REPORT NO.
UCB/SEMM-87/05

STRUCTURAL ENGINEERING
MECHANICS AND MATERIALS

A CLASS OF SIMPLE AND EFFICIENT DEGENERATED SHELL ELEMENTS

BY

LOC VU-QUOC
JESUS A. MORA

JULY 1987

DEPARTMENT OF CIVIL ENGINEERING
UNIVERSITY OF CALIFORNIA
BERKELEY, CALIFORNIA

A Class of Simple and Efficient Degenerated Shell Elements

By

L. Vu-Quoc
Applied Mechanics Division, Stanford University, Stanford, CA 94305.

and

J.A. Mora
Structural Engineering, Mechanics, and Materials,
University of California, Berkeley, CA 94720.

Table of Contents

August 21, 1987

A Class of Simple and Efficient Degenerated Shell Elements

L. Vu-Quoc
Applied Mechanics Division, Stanford University, Stanford, CA 94305.

and

J.A. Mora
Structural Engineering, Mechanics, and Materials,
University of California, Berkeley, CA 94720.

Abstract

We present results obtained for a class of degenerated shell elements formulated in convected (curvilinear) coordinates. Each node has five degrees of freedom, with displacements expressed in the global cartesian system. Rotations of directors are treated in an efficient manner that preserves continuity across inter-element boundaries, and allows treatment of general boundary conditions. A continuous field of local triads can be generated by a method proposed herein. A plane stress linear constitutive relation is developed with respect to a general system of curvilinear coordinates whose transverse coordinate is not necessarily normal to the shell lamina. Element stiffness matrices are obtained in a form directly ready for global assemblage, avoiding completely local-global transformations. Uniform reduced integration is employed to relieve shear and membrane locking. It is shown analytically that spurious zero-energy modes are invariant under change of element geometry. These spurious modes are filtered in a reliable and efficient manner that preserves consistency of the element, and is insensitive to change of material constants and geometric parameters. The element passes patch tests, and is robust under severe element distortions. Several numerical results are presented to assess the performance of the element. Practical aspects of implementing the present formulation are also discussed.

1. Introduction

The first degenerated element for general analysis of shell structures was presented in Ahmad, Irons, & Zienkiewicz [1970]. Further investigations into this type of element by numerous authors followed this early work; a (partial) list of references pertaining to the subject can be found in Hughes & Tezduyar [1981]. It was very soon realized that the fully-integrated stiffness matrix of this element, in particular, over-estimates the stiffness of the shell as its thickness decreases, i.e., the shear-locking problem. Convergence of numerical solution is obtained, in some examples, at a very slow rate. To remedy the shear locking problem, selective/reduced integration was proposed simultaneously by Zienkiewicz, Taylor, & Too [1971], and Pawsey & Clough [1971]. As is in general the case, early pioneering numerical work would be later re-considered in search for a firmer foundation based on mathematical analysis — the finite element method itself is

an example. Selective/reduced integration of a shell stiffness matrix, a "numerical trick" as it appeared to be at first, was subsequently shown to fall within the concept of (implicit) mixed finite element method by Malkus & Hughes [1976]. It was also found that the use of reduced integration mitigates considerably the problem of membrane locking in curved shell elements (Stolarski & Belytschko [1982]).†

Even though good results were achieved with selective/reduced integration, this method by itself is not a panacea to the membrane/shear locking problem: spurious zero-energy modes appear as one under-integrates the stiffness matrix. An ingenious remedy to this problem by filtering the spurious zero-energy modes from the under-integrated stiffness matrix was employed in Kosloff & Frazier [1978]. This methodology was first applied to shell elements by Taylor [1979], and thereafter in the work of Belytschko and co-workers [1984,85]. The latters justified to some extend their approach via the Hu-Washizu variational principle (Belytschko *et al* [1985b]). We mention briefly here a different avenue to solve the locking problem pioneered by MacNeal [1978,82] in using an assumed-strain field together with full integration of the stiffness matrix. A variational foundation of the assumed-strain method was later provided by Simo & Hughes [1986]. Explicit mixed method is yet another approach to this problem, e.g., Pian & Sumihara [1984].

We present in this paper results obtained for a class of simple and efficient degenerated shell elements formulated in convected (curvilinear) coordinates. A director is defined as a vector colinear with the transverse fiber to the shell mid-surface; these directors form a vector field. The director field is not necessarily normal to the shell mid-surface, but is required to be continuous over the shell surface. The shell has five degrees of freedom: three displacement components, expressed in global cartesian coordinate system, and two rotation components to describe the rotation of a director. We

† An argument for the use of curved elements versus flat elements in modeling general shell structures can be found for example in Parisch [1979].

also require that the two rotation fields be continuous across the elements. The two rotation components of a director could be expressed with respect to two arbitrary base vectors, provided that the director and the two base vectors are independent. General rotational boundary conditions can be accounted for by expressing these conditions in the form of linear constraint equations involving rotational degrees of freedom. These constraint equations are then eliminated directly at the element level, before the global assemblage of the stiffness matrix.

The element is formulated exactly with linearized strain tensor in convected coordinates (without neglecting any higher order terms in the convected coordinates). Several types of strain components, with corresponding elastic moduli tensors, could be employed to compute the stiffness matrix with identical results. Plane stress elasticity is assumed at the shell lamina level (a surface defined by keeping constant the transverse convected coordinate of the shell). In general shell structures, often the director field is not normal to a shell lamina due to thickness variation or sharp angle connection. In these cases, we develop elastic moduli tensors with respect to convected coordinates to enforce the plane stress constraints, i.e., zero stress components in the direction normal to a shell lamina. Element stiffness matrices are obtained in a form directly ready for assemblage of the global stiffness, thus avoiding completely local-global transformations at element level. Finally, stress resultants and stress couples are also evaluated with respect to the convected coordinates on the shell.

We adopt uniform reduced-integration of the stiffness matrix to relieve shear and membrane locking in thin shell elements — full integration is used for thick shell. Belytschko and co-workers [1984,85] derived the hourglass modes for rectangular elements, and observed by numerical experiments that these hourglass modes remain the same regardless of the shape of the element. This invariance property of the hourglass modes is herein analytically asserted. An efficient scheme for filtering spurious zero-energy modes is proposed by ways of perturbing the (singular) stiffness matrix. It is

shown that this scheme is the most efficient in its class. The proposed filtering scheme is consistent with linear displacement field in general curved elements, and up to quadratic displacement field in flat elements. Further, the condition that the hourglass modes are always filtered out is explicitly accounted for in the method. The simplicity of the present approach lies in the fact that one does not need to perform several tests to look for appropriate weighting coefficients, i.e., there is no parameter tuning as done in Belytschko Ong & Liu [1984]. It should be noted that while Belytschko and co-workers [1985a] proposed to filter the hourglass modes with respect to the stiffness matrix expressed in a local cartesian coordinate system (the weighting coefficients are computed in these local coordinates), we perform this operation directly on the element stiffness matrix in the global cartesian coordinate system. In addition, the hourglass filtering in Belytschko *et al* [1985a] requires exact integration of certain quantities over the area of a shell element (whereas the stiffness matrix is computed with uniformly reduced integration); in the present work no such integration is needed. As a result, the present filtering scheme is far less expensive. Further, this scheme is insensitive to change of material properties and of element geometric parameters (thickness, area).

Several types of finite element interpolation could be employed in the present formulation: 4-node bilinear, 8-node serendipity, 9-node Lagrangian, ... A particular emphasis in the present work is given to the 9-node Lagrangian interpolation scheme.‡ This shell element passes the patch tests, in particular the pure bending test with quadratic displacement field, and is robust under severe element distortions. The 9-node element is subjected to an extensive course of obstacles as proposed in MacNeal & Harder [1985] and in The Finite Element Standards Forum (see Forsberg & Fong [1985]) for static problems. Numerical results are compared with known analytical results whenever possible, or with numerical results from other workers. As a consequence of

‡ An argument favoring the use of higher-order elements versus lower ones, regarding robustness and computer cost to achieve an error within the range of 1-2%, is given in Babuska [1987].

avoiding local-global transformations in element stiffnesses, of using uniformly reduced integration, and efficient spurious-mode filtering, this class of shell elements is inexpensive, and yet provides accurate results in several numerical examples documented herein.

2. Kinematic assumption

In this section, we describe the underlying basic linear kinematic assumption in the formulation of the shell element, and define how rotational degrees of freedom are chosen to preserve continuity across the elements. A triad of vectors designates a system of three independent vectors, not necessarily orthonormal to each other. Two types of triad are often referred to in this paper: the global (orthogonal) triad and the local triad. We indicate a convenient way to generate a continuous field of local orthonormal triads from the global triad. Finally, treatment of general rotational boundary conditions at the element level is also indicated.

2.1. Basic linear kinematic assumption

Let $\{\mathbf{E}_1, \mathbf{E}_2, \mathbf{E}_3\}$ denote a system of orthonormal base vectors which forms the global (orthogonal) triad. The (global) cartesian coordinates along the global base vectors are denoted respectively by (X^1, X^2, X^3). A material point $X \in \Omega$ with coordinates (X^1, X^2, X^3), where $\Omega \subset \mathbf{R}^3$ is the domain of the shell, is represented by the position vector $\mathbf{X} = X^I\mathbf{E}_I$.† A system of curvilinear coordinates $(\theta^1, \theta^2, \theta^3)$ is inscribed on the domain Ω of the shell, with (θ^1, θ^2) being the coordinates on the shell surface, and θ^3 the transverse coordinate. The domain of θ^3 is chosen to be the closed interval $[-1, 1]$. A shell lamina is thus a surface with $\theta^3 = \textit{constant}$; the shell mid-surface is the lamina located at $\theta^3 = 0$. The tangent vectors to these curvilinear coordinate lines are

$$\mathbf{A}_j(\theta^{(i)}) = A_j^I\mathbf{E}_I := \frac{\partial X(\theta^{(i)})}{\partial\theta^j} = \frac{\partial X^I(\theta^{(i)})}{\partial\theta^j}\,\mathbf{E}_I\,, \quad \text{for } j = 1,2,3\,. \tag{2.1}$$

† Whenever the summation sign Σ is omitted, summation convention is implied over repeated indices. Roman-letter indices take values in {1,2,3}, Greek-letter indices in {1,2}.

On the shell mid-surface, we define a director field $\mathbf{D}(\theta^{\{\alpha\}}) = D^I(\theta^{\{\alpha\}})\mathbf{E}_I$, not necessarily normal to the mid-surface.‡ Let x denote the image of X under a deformation map. Note that x and X have the same curvilinear coordinates $(\theta^1, \theta^2, \theta^3)$; this type of coordinates is referred to as convected coordinates, and is often used in shell theory (Naghdi [1972]). It is assumed that the displacement in the shell, denoted by $\mathbf{u}^*$, takes the following form

$$\mathbf{u}^*(\theta^{\{i\}}) := x(\theta^{\{i\}}) - X(\theta^{\{i\}}) = \mathbf{u}(\theta^{\{\alpha\}}) + \theta^3 \frac{h(\theta^{\{\alpha\}})}{2} [\, \mathbf{d}(\theta^{\{\alpha\}}) - \mathbf{D}(\theta^{\{\alpha\}}) \,] , \tag{2.2}$$

where $\mathbf{u}(\theta^{\{\alpha\}}) := \mathbf{u}^*(\theta^{\{\alpha\}},0)$ is the displacement of the point $(\theta^{\{\alpha\}}) \equiv (\theta^1, \theta^2)$ on the mid-surface (the intersection of the director and the mid-surface), $h(\theta^{\{\alpha\}}) > 0$ the thickness of the shell along the transverse fiber, and $\mathbf{d}(\theta^{\{\alpha\}})$ the image of the director $\mathbf{D}(\theta^{\{\alpha\}})$ under a rotation operation defined shortly. Let $\{\mathbf{e}_1, \mathbf{e}_2, \mathbf{e}_3\}$ denote the spatial base vectors chosen such that $\mathbf{e}_i \delta^i_I \equiv \mathbf{E}_I$ for convenience. We have in component form $\mathbf{u} = u^i \mathbf{e}_i$, and $\mathbf{d} = d^i \mathbf{e}_i$. The above assumed kinematics simply states that displacement of any point X in the shell is the sum of the displacement of the projected point on the mid-surface along the director passing through X, and of the displacement due to rotation of the director.

2.2. Rotation of directors

The rotation of a director $\mathbf{D}$ is obtained through an orthogonal transformation $\mathbf{\Lambda}$ (a linear transformation) as follows

$$\mathbf{d} = \mathbf{\Lambda}\, \mathbf{D} \,. \tag{2.3}$$

In general finite rotations, $\mathbf{\Lambda}$ is a member of the special orthogonal group $SO(3)$. Let $\boldsymbol{\chi} = \chi^i \mathbf{e}_i$ denote the rotation vector, then $\mathbf{\Lambda}$ can be evaluated via the exponentiation $\exp[\overset{\mathrm{v}}{\boldsymbol{\chi}}]$. Here $\overset{\mathrm{v}}{\boldsymbol{\chi}}$ denotes the skew-symmetric tensor, whose axial vector is $\boldsymbol{\chi}$, such that

‡ Consistent with our notation in the previous footnote, $(\theta^{\{i\}})$ is shorthand notation for $(\theta^1, \theta^2, \theta^3)$, and $(\theta^{\{\alpha\}})$ is shorthand notation for (θ^1, θ^2).

$\overset{v}{\boldsymbol{\chi}}\mathbf{D} \equiv \boldsymbol{\chi}\times\mathbf{D}$. For a complete treatment of this operation, we refer to Simo & Vu-Quoc [1986,87] and Vu-Quoc [1986]. In the present work, only infinitesimal rotation of the director is considered; the series in $\exp[\overset{v}{\boldsymbol{\chi}}]$ is truncated to

$$\boldsymbol{\Lambda} = \exp[\overset{v}{\boldsymbol{\chi}}] = \mathbf{1} + \overset{v}{\boldsymbol{\chi}} + O(\overset{v}{\boldsymbol{\chi}}^2)\,, \tag{2.4}$$

with $\mathbf{1}$ denoting the identity tensor. Thus the displacement of a point on the transverse fiber with director $\mathbf{D}$ can be obtained with the aid of

$$\mathbf{d} - \mathbf{D} = \overset{v}{\boldsymbol{\chi}}\mathbf{D} \equiv \boldsymbol{\chi}\times\mathbf{D}\,. \tag{2.5}$$

We have to define the components of the rotation vector $\boldsymbol{\chi}$. First, in this formulation, rotation of the director about itself is not accounted for, and is thus represented by only two parameters. Further, it is required that the rotation vector $\boldsymbol{\chi}$ be normal to the director to eliminate the rotation about the director itself. Thus let $\mathbf{T}_1$ and $\mathbf{T}_2$ be independent unit vectors normal to the director $\mathbf{D}$. The rotation vector $\boldsymbol{\chi}$ can be expressed as $\boldsymbol{\chi} = \chi^\alpha\mathbf{T}_\alpha$, where (χ^1, χ^2) are the two rotation components. It should be noted here that $\mathbf{T}_1$ and $\mathbf{T}_2$ need not be orthogonal to each other.

Choice of local triads. In order to obtain continuous rotation fields across the element boundaries, as well as to facilitate the filtering of spurious modes discussed later, we require that the field of local triads $\{\mathbf{D}, \mathbf{T}_1, \mathbf{T}_2\}$ be continuous; i.e., $\mathbf{D}(\theta^{\{\alpha\}})$, $\mathbf{T}_1(\theta^{\{\alpha\}})$, and $\mathbf{T}_2(\theta^{\{\alpha\}})$ are continuous vector fields on the shell surface.

Proposition 2.1. *Let* $\mathbf{D}$ *be a continuous field of directors on the shell mid-surface, and let* $\boldsymbol{\chi}$ *be the rotation vector such that* $\mathbf{D} = \exp[\overset{v}{\boldsymbol{\chi}}]\mathbf{E}_\mathrm{I}$, *with* $\mathrm{I} \in \{1,2,3\}$. *Let* (I, J, K) *be a cyclic permutation of* (1,2,3). *Then* $\mathbf{T}_1 = \exp[\overset{v}{\boldsymbol{\chi}}]\mathbf{E}_\mathrm{J}$ *and* $\mathbf{T}_2 = \exp[\overset{v}{\boldsymbol{\chi}}]\mathbf{E}_\mathrm{K}$ *are continuous vector fields on the shell mid-surface.*

Proof. The continuity of the vector fields $\mathbf{T}_1$ and $\mathbf{T}_2$ follows at once from that of $\mathbf{D}$. Suppose that $\mathbf{T}_1$ is not continuous at $(\hat{\theta}^{\{\alpha\}})$, then there exists a curve on the shell surface such that as $(\theta^{\{\alpha\}})\rightarrow(\hat{\theta}^{\{\alpha\}})$ from two sides on that curve, $\mathbf{T}_1$ tends to two distinct vectors, say $\mathbf{T}_1$ and $\mathbf{T}_1'$. It follows that there are two distinct rotation vectors $\boldsymbol{\chi}$ and $\boldsymbol{\chi}'$

such that $\mathbf{T}_I = \exp[\overset{\vee}{\boldsymbol{\chi}}]\mathbf{E}_J$ and $\mathbf{T}_I' = \exp[\overset{\vee}{\boldsymbol{\chi}}']\mathbf{E}_J$. One reaches a contradiction since $\mathbf{D} = \exp[\overset{\vee}{\boldsymbol{\chi}}]\mathbf{E}_I \neq \exp[\overset{\vee}{\boldsymbol{\chi}}']\mathbf{E}_I$, i.e., the director field is not continuous. □

It should be noted that the global base vector to be rotated to the director $\mathbf{D}$ can be chosen arbitrarily among the vectors $\{\mathbf{E}_1, \mathbf{E}_2, \mathbf{E}_3\}$. An efficient algorithm for this procedure is given in Appendix **I**. This method thus provides an unequivocally simple way to generate the wanted continuous field of local triads, and is illustrated in Figure 2.2a, where for the sake of simplicity $\mathbf{E}_1$ is chosen to be rotated to the director $\mathbf{D}$.

Remark 2.1. There exist other ways of generating the local triads such as proposed in Hughes & Liu [1981], and in Huang & Hinton [1986]. But these methods tend to be biased toward either one direction or one plane — the Huang & Hinton method is sensitive to perturbation of the director about the axis $\mathbf{E}_2$. Arbitrary conventions are made to remove ambiguities, and to render unique the choice of a local triad. Further, they do not meet our requirement to have a continuous field of local triads on the shell surface (both inside an element or across inter-element boundaries). This remark is illustrated in Figures 2.2b and 2.2c, on the same mesh as in Figure 2.2a, where the generated fields of triads is not continuous within an element. This example has the same topology as that of the hemisphere in Example 6.9, and later helps explain the asymmetry in the results when the above methods of generating local triads are employed. □

Remark 2.2. In engineering calculation, one regularly encounters cases of shell structure with folds and branches, where several shells are welded together along a certain curve. It should be noted that in these situations, we have stepped outside of the realm of shell theory; a detailed stress analysis at these connection points requires the 3-D continuum theory. Shell theory is applied when we are only interested in the global shell response of the structure. The proposed method of generating local triads remains applicable in the above case, for once the director at a node on the connection line is given, the local triad is determined uniquely. Further, if the field of directors is continuous on the whole structure (including the connection line in the branching shell case),

then by the above proposition the field of local triads is also continuous. □

Remark 2.3. The use of normals to element mid-surface instead of a continuous director field to generate local triads will clearly result in discontinuity of the rotation fields, since normals to element mid-surface are not continuous across inter-element boundaries. This method is not applicable in the case of branching shell structure considered in the previous remark. □

Finite element interpolation. Let the domain Ω of the shell be subdivided into (shell) finite elements Ω_e, for $e = 1,2,...$, where each element has N nodal points. Let $P_I(\theta^{\{\alpha\}})$, a polynomial in $(\theta^{\{\alpha\}})$, denote the finite element interpolation function corresponding to node I, and $\theta^1, \theta^2 \in [-1, 1]$ are the natural coordinates on a shell lamina. The position vector $\mathbf{X}$ of a material point in the shell element is interpolated by

$$\begin{aligned} \mathbf{X} &\cong \sum_{I=1}^{N} P_I(\theta^{\{\alpha\}}) \left[\mathbf{X}_I + \theta^3 \frac{h_I}{2} \mathbf{D}_I \right], \\ \text{with } \mathbf{X}_I &:= \mathbf{X}(\theta_I^1, \theta_I^2, 0), \quad \text{and } \mathbf{D}_I := \mathbf{D}(\theta_I^1, \theta_I^2), \end{aligned} \tag{2.6}$$

whereas the displacement field within each element is interpolated by

$$\mathbf{u}^*(\theta^{\{i\}}) \cong \sum_{I=1}^{N} P_I(\theta^{\{\alpha\}}) \, \mathbf{u}^*_I(\theta^3), \quad \text{with } \mathbf{u}^*_I(\theta^3) := \mathbf{u}^*(\theta_I^1, \theta_I^2, \theta^3). \tag{2.7a}$$

Subscripts in capital roman letters such as I designate hereafter quantities pertaining to node I whose coordinates are $(\theta_I^1, \theta_I^2, 0)$. Equation (2.7a) could be expressed in terms of the nodal displacement $\mathbf{u}_I = u_I^i \mathbf{e}_i$ and nodal rotation $\boldsymbol{\chi}_I = \chi_{(I)}^{\alpha} \mathbf{T}_{\alpha(I)}$† as follows

$$\mathbf{u}^*(\theta^{\{i\}}) \cong \sum_{I=1}^{N} P_I(\theta^{\{\alpha\}}) \left[\mathbf{u}_I + \theta^3 \frac{h_I}{2} \boldsymbol{\chi}_I \times \mathbf{D}_I \right]. \tag{2.7b}$$

An element has thus $n := 5 \times N$ degrees of freedom, which is ordered according to $\Delta := \{u_1^{\{i\}}, \chi_1^{\{\alpha\}} \mid \cdots \mid u_N^{\{i\}}, \chi_N^{\{\alpha\}}\}^{\mathrm{T}} \in \mathbf{R}^n$.

† Summation convention does not apply for indices in parentheses.

Remark 2.4. In our computer implementation, the data at node I are (X_I^1, X_I^2, X_I^3), h_I, and the coordinates of a fictitious node which are used to compute the nodal director $\mathbf{D}_I$. It should be noted that the distance between node I and its fictitious node need not be $\frac{h_I}{2}$. Thus the use of fictitious nodes facilitates greatly the input of data since one is not required to trace exactly the upper and lower surfaces of the shell such as in the procedure employed in Hughes & Liu [1981]. □

2.4. Rotation boundary conditions

Often in general analysis of shell structures, one encounters situations involving constraints of rotation degrees of freedom along the shell boundary. We will show how this type of rotation boundary conditions could be exactly satisfied at the element level. Consider a constrained rotation on the boundary as shown in Figure 2.3, together with the local triad $\{\mathbf{D}, \mathbf{T}_1, \mathbf{T}_2\}$. Let $\overline{\mathbf{T}}_1$ be a unit vector associated with the constrained rotational degree of freedom, and $\overline{\mathbf{T}}_2$ an unit vector normal to $\overline{\mathbf{T}}_1$ such that $\{\overline{\mathbf{T}}_1, \overline{\mathbf{T}}_2\}$ and $\{\mathbf{T}_1, \mathbf{T}_2\}$ lie in the same plane. Let β be the angle between $\mathbf{T}_1$ and $\overline{\mathbf{T}}_1$. The rotation vector $\boldsymbol{\chi}$ can then be expressed in the basis $\{\overline{\mathbf{T}}_1, \overline{\mathbf{T}}_2\}$ as

$$\boldsymbol{\chi} = (\chi^1 \cos\beta + \chi^2 \sin\beta)\overline{\mathbf{T}}_1 + (\chi^2 \cos\beta - \chi^1 \sin\beta)\overline{\mathbf{T}}_2 \,. \tag{2.8}$$

Thus prescribing for example the rotation about $\overline{\mathbf{T}}_1$ axis, denoted by $\hat{\chi}^1$, is equivalent to imposing a linear constraint equation, which at node I reads as follows

$$\chi^1_{(I)} \cos\beta_{(I)} + \chi^2_{(I)} \sin\beta_{(I)} = \hat{\chi}^1_I \,.\dagger \tag{2.9}$$

This constraint equation could be eliminated directly at the element level. The rotation degree of freedom whose axis is closest to $\overline{\mathbf{T}}_1$ will be eliminated. Thus, if $|\cos\beta_I| \geq |\sin\beta_I|$, then χ^1_I is to be eliminated — otherwise, we eliminate the rotation component χ^2_I. The space of admissible variations for the rotations, whose elements are

† Summation convention does not apply for indices in parentheses.

denoted by ς^α, is subjected to the corresponding constraint

$$\varsigma^1_{(I)} \cos\beta_{(I)} + \varsigma^2_{(I)} \sin\beta_{(I)} = 0 \ .\dagger \tag{2.10}$$

Hence suppose that we are to eliminate χ^1_1. Defining the "condensation" matrix $\mathbf{L}$, and the force column-matrix $\mathbf{f}$ by

$$\mathbf{L} := \begin{bmatrix} 1 & 0 & 0 & 0 & . & . & . \\ 0 & 1 & 0 & 0 & . & . & . \\ 0 & 0 & 1 & 0 & . & . & . \\ 0 & 0 & 0 & -\tan\beta_1 & . & . & . \\ 0 & 0 & 0 & 1 & . & . & . \\ . & . & . & . & . & . & . \\ . & . & . & . & . & 1 & 0 \\ . & . & . & . & . & 0 & 1 \end{bmatrix} \in \mathbf{R}^{n\times(n-1)}, \quad \mathbf{f} := \begin{Bmatrix} 0 \\ 0 \\ 0 \\ \hat{\chi}^1_1/\cos\beta_1 \\ 0 \\ . \\ . \\ 0 \end{Bmatrix} \in \mathbf{R}^{n\times 1}, \tag{2.11}$$

then the condensed stiffness matrix and applied force are simply

$$\mathbf{K}^{cond} = \mathbf{L}^T \mathbf{K}\, \mathbf{L} \in \mathbf{R}^{(n-1)\times(n-1)}, \text{ and } \mathbf{f}^{cond} = \mathbf{L}^T \mathbf{K}\, \mathbf{f} \in \mathbf{R}^{(n-1)\times 1}, \tag{2.12}$$

where $\mathbf{K} \in \mathbf{R}^{n\times n}$ is the original unconstrained stiffness matrix. The above operation is repeated at all nodes where rotation boundary conditions are to be enforced.

Remark 2.5. Often in practice, either the rotation about the tangent to the shell boundary (e.g., clamped edge), or the rotation about the normal to the shell boundary (e.g., simply supported edge) is constrained. In these cases, $\overline{\mathbf{T}}_1$ could be conveniently chosen to be the tangent vector to the shell boundary. □

Remark 2.6. In a finite element discretization, tangent vectors to the shell boundary at a node common to two adjacent shell elements do not necessarily lie in the plane $\{\mathbf{T}_1, \mathbf{T}_2\}$ (with normal $\mathbf{D}$). In this case, the above treatment of rotation boundary conditions is to be performed with respect to the projection of vectors $\overline{\mathbf{T}}_\alpha$'s on the plane $\{\mathbf{T}_1, \mathbf{T}_2\}$ given by $[\ \mathbf{1} - \mathbf{D}\otimes\mathbf{D}\ ]\overline{\mathbf{T}}_\alpha$, where $\mathbf{1}$ is the identity operator, and $\otimes$ is the tensor product defined such that $[\ \mathbf{D}\otimes\mathbf{D}\ ]\overline{\mathbf{T}}_\alpha := (\mathbf{D}\cdot\overline{\mathbf{T}}_\alpha)\mathbf{D}$. □

3. Strain and stress tensors

In this section, we recall expressions of strain tensor in convected coordinates, and develop the strain-displacement relations which will be used extensively later. Expressions of stress resultants and stress couples are also summarized.

3.1. Strain tensors in convected coordinates

Let the tangent vectors to the (convected) coordinate lines in the deformed configuration be defined as

$$\mathbf{a}_k(\theta^{\{i\}}) := \frac{\partial x(\theta^{\{i\}})}{\partial \theta^k} = \frac{\partial x^j(\theta^{\{i\}})}{\partial \theta^k}\,\mathbf{e}_j \ , \quad \text{for } k=1,2,3 \ . \tag{3.1}$$

In the undeformed configuration, these tangent vectors are denoted by $\{\mathbf{A}_1, \mathbf{A}_2, \mathbf{A}_3\}$, and defined according to (2.1). Further, let the cotangent vectors conjugate to these tangent vectors be denoted respectively by $\{\mathbf{a}^1, \mathbf{a}^2, \mathbf{a}^3\}$ and $\{\mathbf{A}^1, \mathbf{A}^2, \mathbf{A}^3\}$. The corresponding metric tensors are then defined by

$$\begin{aligned} \mathbf{g} &= g_{ij}\mathbf{a}^i \otimes \mathbf{a}^j = (\mathbf{a}_i \bullet \mathbf{a}_j)\mathbf{a}^i \otimes \mathbf{a}^j \ , \\ \mathbf{g}^{\#} &= g^{ij}\mathbf{a}_i \otimes \mathbf{a}_j = (\mathbf{a}^i \bullet \mathbf{a}^j)\mathbf{a}_i \otimes \mathbf{a}_j \ , \end{aligned} \tag{3.2a}$$

$$\begin{aligned} \mathbf{G} &= G_{ij}\mathbf{A}^i \otimes \mathbf{A}^j = (\mathbf{A}_i \bullet \mathbf{A}_j)\mathbf{A}^i \otimes \mathbf{A}^j \ , \\ \mathbf{G}^{\#} &= G^{ij}\mathbf{A}_i \otimes \mathbf{A}_j = (\mathbf{A}^i \bullet \mathbf{A}^j)\mathbf{A}_i \otimes \mathbf{A}_j \ , \end{aligned} \tag{3.2b}$$

where the matrices $[g^{ij}]$ and $[G^{ij}]$ are the inverses of the matrices $[g_{ij}]$ and $[G_{ij}]$, respectively. The deformation gradient takes a simple form in convected coordinates:

$$\mathbf{F} = \delta^i_j \mathbf{a}_i \otimes \mathbf{A}^j = \mathbf{a}_i \otimes \mathbf{A}^i \ , \tag{3.3a}$$

where δ^i_j is the Kronecker delta. It follows that the transpose of $\mathbf{F}$ can be expressed by (e.g., Marsden & Hughes [1983])

$$\mathbf{F}^{\mathrm{T}} = G^{ip}\delta^q_p g_{qj}\mathbf{A}_i \otimes \mathbf{a}^j = G^{ik}g_{kj}\mathbf{A}_i \otimes \mathbf{a}^j \ . \tag{3.3b}$$

Using (3.3a) and (3.3b) to compute the material (mixed) strain tensor $\boldsymbol{\Gamma} = \Gamma^i_j \mathbf{A}_i \otimes \mathbf{A}^j$, we obtain

$$\boldsymbol{\Gamma} = \frac{1}{2}\left[\,\mathbf{F}^{\mathrm{T}}\mathbf{F} - \mathbf{1}\,\right] = \frac{1}{2}\left[\,G^{ik}g_{kj} - \delta^i_j\,\right]\mathbf{A}_i \otimes \mathbf{A}^j \,. \tag{3.4a}$$

Define $\boldsymbol{\Gamma}^{\#} := \Gamma^{ij}\mathbf{A}_i \otimes \mathbf{A}_j$ by raising the indices of $\boldsymbol{\Gamma}$, and $\boldsymbol{\Gamma}^{@} := \Gamma_{ij}\mathbf{A}^i \otimes \mathbf{A}^j$ by lowering the indices of $\boldsymbol{\Gamma}$, we have

$$\boldsymbol{\Gamma}^{\#} = \Gamma^i_k G^{kj}\mathbf{A}^i \otimes \mathbf{A}^j = \frac{1}{2}\left[\,G^{ip}g_{pq}G^{qj} - G^{ij}\,\right]\mathbf{A}_i \otimes \mathbf{A}_j \,, \tag{3.4b}$$

$$\boldsymbol{\Gamma}^{@} = G_{ik}\Gamma^k_j\mathbf{A}^i \otimes \mathbf{A}^j = \frac{1}{2}\left[\,g_{ij} - G_{ij}\,\right]\mathbf{A}^i \otimes \mathbf{A}^j \,. \tag{3.4c}$$

It should be noted that while $\boldsymbol{\Gamma}$ is not a symmetric tensor, $\boldsymbol{\Gamma}^{\#}$ and $\boldsymbol{\Gamma}^{@}$ are. The components of $\boldsymbol{\Gamma}^{@}$ were used in shell theory in Naghdi [1972] (see also Green & Zerna [1968]).

3.2. Strain-displacement relations

From (2.1), (2.2), and (3.1), one could easily see that

$$\mathbf{a}_i = \frac{\partial(X + \mathbf{u}^*)}{\partial\theta^i} = \mathbf{A}_i + \frac{\partial\mathbf{u}^*}{\partial\theta^i} \,, \tag{3.5}$$

$$\text{and} \quad g_{ij} = \mathbf{a}_i \bullet \mathbf{a}_j = G_{ij} + \mathbf{A}_i \bullet \frac{\partial\mathbf{u}^*}{\partial\theta^j} + \frac{\partial\mathbf{u}^*}{\partial\theta^i} \bullet \mathbf{A}_j + \frac{\partial\mathbf{u}^*}{\partial\theta^i} \bullet \frac{\partial\mathbf{u}^*}{\partial\theta^j} \,. \tag{3.6}$$

It follows that $\boldsymbol{\Gamma}$, $\boldsymbol{\Gamma}^{\#}$, and $\boldsymbol{\Gamma}^{@}$ take the expressions

$$\boldsymbol{\Gamma} = \frac{1}{2}G^{ik}\left[\mathbf{A}_k \bullet \frac{\partial\mathbf{u}^*}{\partial\theta^j} + \frac{\partial\mathbf{u}^*}{\partial\theta^k} \bullet \mathbf{A}_j + \frac{\partial\mathbf{u}^*}{\partial\theta^k} \bullet \frac{\partial\mathbf{u}^*}{\partial\theta^j}\right]\mathbf{A}_i \otimes \mathbf{A}^j \,, \tag{3.7a}$$

$$\boldsymbol{\Gamma}^{\#} = \frac{1}{2}G^{ip}G^{qj}\left[\mathbf{A}_p \bullet \frac{\partial\mathbf{u}^*}{\partial\theta^q} + \frac{\partial\mathbf{u}^*}{\partial\theta^p} \bullet \mathbf{A}_q + \frac{\partial\mathbf{u}^*}{\partial\theta^p} \bullet \frac{\partial\mathbf{u}^*}{\partial\theta^q}\right]\mathbf{A}_i \otimes \mathbf{A}_j \,, \tag{3.7b}$$

$$\boldsymbol{\Gamma}^{@} = \frac{1}{2}\left[\mathbf{A}_i \bullet \frac{\partial\mathbf{u}^*}{\partial\theta^j} + \frac{\partial\mathbf{u}^*}{\partial\theta^i} \bullet \mathbf{A}_j + \frac{\partial\mathbf{u}^*}{\partial\theta^i} \bullet \frac{\partial\mathbf{u}^*}{\partial\theta^j}\right]\mathbf{A}^i \otimes \mathbf{A}^j \,. \tag{3.7c}$$

Finite element interpolation. It suffices to develop the strain-displacement matrix for the components of $\boldsymbol{\Gamma}^{@}$ since the components of $\boldsymbol{\Gamma}$ and of $\boldsymbol{\Gamma}^{\#}$ follow according to (3.4). Further, since in the present work we are only concerned with linearized strain, the higher order term in displacement $\mathbf{u}^*$ in (3.7) (the last term) is neglected. First, by employing (2.6), the base vectors $\{\mathbf{A}_i = A_i^I\mathbf{E}_I\}$ are such that

$$\mathbf{A}_\alpha = \sum_{I=1}^{N} P_{I,\alpha} \left[\mathbf{X}_I + \theta^3 \frac{h_I}{2} \mathbf{D}_I \right], \quad \mathbf{A}_3 = \sum_{I=1}^{N} P_I \frac{h_I}{2} \mathbf{D}_I, \tag{3.8}$$

with $P_{I,i} := \partial P_I / \partial \theta^i$. Due to the symmetry of $\boldsymbol{\Gamma}^{\#}$ and $\boldsymbol{\Gamma}^{@}$, one often orders the six independent components of these strains in the form of a column matrix:

$$\{\Gamma_{ij}\} := \{\Gamma_{11}, \Gamma_{22}, 2\Gamma_{23}, 2\Gamma_{31}, 2\Gamma_{12}, \Gamma_{33}\}^T \in \mathbf{R}^{6\times 1}. \tag{3.9}$$

Unlike the usual practice of ordering strain components, the above ordering is chosen because in this formulation Γ_{33} plays no role, as will be seen in subsequent sections. Substituting (2.7) into (3.7c), we obtain the linearized components of the strain $\boldsymbol{\Gamma}^{@}$:

$$\Gamma_{\alpha\beta} = \frac{1}{2} \sum_{I=1}^{N} \left(P_{I,\alpha} \mathbf{A}_\beta + P_{I,\beta} \mathbf{A}_\alpha \right) \bullet \mathbf{u}^*_I, \tag{3.10a}$$

$$\Gamma_{\alpha 3} = \Gamma_{3\alpha} = \frac{1}{2} \sum_{I=1}^{N} \left[P_{I,\alpha} \mathbf{A}_3 \bullet \mathbf{u}^*_I + P_I \frac{h_I}{2} \mathbf{A}_\alpha \bullet (\boldsymbol{\chi}_I \times \mathbf{D}_I) \right], \tag{3.10b}$$

$$\Gamma_{33} = \mathbf{A}_3 \bullet \sum_{I=1}^{N} P_I \frac{h_I}{2} \boldsymbol{\chi}_I \times \mathbf{D}_I. \tag{3.10c}$$

With this, we introduce the matrix $\mathbf{B} \in \mathbf{R}^{6\times n}$ relating the strains $\{\Gamma_{ij}\}$ to the nodal degrees of freedom $\{\mathbf{u}_I^{\{i\}}, \boldsymbol{\chi}_I^{\{\alpha\}}\}$,

$$\{\Gamma_{ij}\} =: \mathbf{B}\,\Delta =: \sum_{I=1}^{N} \mathbf{B}_I \begin{Bmatrix} u_I^{\{i\}} \\ \chi_I^{\{\alpha\}} \end{Bmatrix} =: \sum_{i=1}^{3} \mathbf{B}^i_{dis} \begin{Bmatrix} u_1^i \\ \cdot \\ \cdot \\ u_N^i \end{Bmatrix} + \sum_{\alpha=1}^{2} \mathbf{B}^\alpha_{rot} \begin{Bmatrix} \chi_1^\alpha \\ \cdot \\ \cdot \\ \chi_N^\alpha \end{Bmatrix}, \tag{3.11}$$

where $\mathbf{B}_I$ is the partition of $\mathbf{B}$ relating the degrees of freedom at node I to the strains, $\mathbf{B}^i_{dis}$ the partition of $\mathbf{B}$ relating all the displacement degrees of freedom of the element to the strains, and $\mathbf{B}^\alpha_{rot}$ is similar to $\mathbf{B}^i_{dis}$ but for the rotation degrees of freedom of the element. From (3.10), $\mathbf{B}_I$ can be shown to take the following form

$$\mathbf{B}_I = \left[\Xi^0_I \;\middle|\; \frac{h_{(I)}}{2} \left(\theta^3 \Xi^0_{(I)} + \Xi^1_{(I)} \right) \left[-\{T^i_{2(I)}\} \,|\, \{T^i_{1(I)}\} \right] \right] \in \mathbf{R}^{6\times 5}, \tag{3.12a}$$

where $\{T^i_{\alpha I}\} := \{T^1_{\alpha I}, T^2_{\alpha I}, T^3_{\alpha I}\}^T$ denotes the column matrix of components of

$\mathbf{T}_{\alpha \mathrm{I}} = T^{\mathrm{J}}_{\alpha \mathrm{I}} \mathbf{E}_{\mathrm{J}}$, and

$$\Xi^0_{\mathrm{I}} := \begin{bmatrix} P_{\mathrm{I},1}A^1_1 & P_{\mathrm{I},1}A^2_1 & P_{\mathrm{I},1}A^3_1 \\ P_{\mathrm{I},2}A^1_2 & P_{\mathrm{I},2}A^2_2 & P_{\mathrm{I},2}A^3_2 \\ P_{\mathrm{I},2}A^1_3 & P_{\mathrm{I},2}A^2_3 & P_{\mathrm{I},2}A^3_3 \\ P_{\mathrm{I},1}A^1_3 & P_{\mathrm{I},1}A^2_3 & P_{\mathrm{I},1}A^3_3 \\ (P_{\mathrm{I},1}A^1_2 + P_{\mathrm{I},2}A^1_1) & (P_{\mathrm{I},1}A^2_2 + P_{\mathrm{I},2}A^2_1) & (P_{\mathrm{I},1}A^3_2 + P_{\mathrm{I},2}A^3_1) \\ 0 & 0 & 0 \end{bmatrix} \in \mathbf{R}^{6\times 3}, \quad (3.12b)$$

$$\Xi^1_{\mathrm{I}} := P_{\mathrm{I}} \begin{bmatrix} 0 & 0 & 0 \\ 0 & 0 & 0 \\ A^1_2 & A^2_2 & A^3_2 \\ A^1_1 & A^2_1 & A^3_1 \\ 0 & 0 & 0 \\ A^1_3 & A^2_3 & A^3_3 \end{bmatrix} \in \mathbf{R}^{6\times 3}. \quad (3.12c)$$

In the above, we have made use of the relation $\mathbf{T}_\alpha \times \mathbf{D} = e_{\beta\alpha}\mathbf{T}_\beta$, with $e_{\alpha\beta}$ being the alternating symbol defined such that $e_{11} := e_{22} := 0$, and $e_{12} := -e_{21} := 1$. While the matrices in (3.12) are useful for computer implementation, the following definitions will prove useful when we deal with the spurious zero-energy modes. Again, from (3.10) we obtain

$$\mathbf{B}^i_{dis} = \begin{bmatrix} A^i_1 \left\{ P_{1,1}, \cdots, P_{N,1} \right\} \\ A^i_2 \left\{ P_{1,2}, \cdots, P_{N,2} \right\} \\ A^i_3 \left\{ P_{1,2}, \cdots, P_{N,2} \right\} \\ A^i_3 \left\{ P_{1,1}, \cdots, P_{N,1} \right\} \\ \left(A^i_1 P_{1,2} + A^i_2 P_{1,1} \right), \cdots, \left(A^i_1 P_{N,2} + A^i_2 P_{N,1} \right) \\ 0, \cdots, 0 \end{bmatrix} \in \mathbb{R}^{6\times N}, \quad (3.13a)$$

$$\mathbf{B}^\alpha_{rot} = \frac{1}{2} e_{\alpha\beta} \begin{bmatrix} \theta^3 \mathbf{A}_1 \bullet \left\{ h_1 P_{1,1}\mathbf{T}_{\beta 1}, \cdots, h_N P_{N,1}\mathbf{T}_{\beta N} \right\} \\ \theta^3 \mathbf{A}_2 \bullet \left\{ h_1 P_{1,2}\mathbf{T}_{\beta 1}, \cdots, h_N P_{N,2}\mathbf{T}_{\beta N} \right\} \\ h_1(P_{1,2}\theta^3\mathbf{A}_3 + P_1\mathbf{A}_2)\bullet\mathbf{T}_{\beta 1}, \cdots, h_N(P_{N,2}\theta^3\mathbf{A}_3 + P_N\mathbf{A}_2)\bullet\mathbf{T}_{\beta N} \\ h_1(P_{1,1}\theta^3\mathbf{A}_3 + P_1\mathbf{A}_1)\bullet\mathbf{T}_{\beta 1}, \cdots, h_N(P_{N,1}\theta^3\mathbf{A}_3 + P_N\mathbf{A}_1)\bullet\mathbf{T}_{\beta N} \\ h_1\theta^3(P_{1,1}\mathbf{A}_2 + P_{1,2}\mathbf{A}_1)\bullet\mathbf{T}_{\beta 1}, \cdots, h_N\theta^3(P_{N,1}\mathbf{A}_2 + P_{N,2}\mathbf{A}_1)\bullet\mathbf{T}_{\beta N} \\ \mathbf{A}_3 \bullet \left\{ h_1 P_1\mathbf{T}_{\beta 1}, \cdots, h_N P_N\mathbf{T}_{\beta N} \right\} \end{bmatrix} \in \mathbb{R}^{6\times N}.$$

(3.13b)

3.3. Conjugate stress tensors. Stress resultants and stress couples

The stress tensors conjugate to the strains $\boldsymbol{\Gamma}$, $\boldsymbol{\Gamma}^{\#}$, and $\boldsymbol{\Gamma}^{@}$ are denoted respectively by $\mathbf{S} = S^i_j \mathbf{A}_i \otimes \mathbf{A}^j$, $\mathbf{S}^{@} = S_{ij}\mathbf{A}^i \otimes \mathbf{A}^j$, and $\mathbf{S}^{\#} = S^{ij}\mathbf{A}_i \otimes \mathbf{A}_j$. The internal energy in the shell can then be written with respect to these strains as follows

$$W := \frac{1}{2}\int_{\Omega} S^j_i \, \Gamma^i_j d\Omega = \frac{1}{2}\int_{\Omega} S_{ij}\Gamma^{ij} d\Omega = \frac{1}{2}\int_{\Omega} S^{ij}\Gamma_{ij} d\Omega \, . \tag{3.14}$$

The stress resultants and stress couples are computed on a surface $\theta^\alpha = \textit{constant}$, where a "directed" infinitesimal area on that surface is given by $\mathbf{A}^\alpha \sqrt{G}\, e_{\alpha\beta} d\theta^\beta d\theta^3$, with $G := \det[G_{ij}]$. Therefore, with the small deformation assumption, the contact force acting on a portion of the surface $\theta^\alpha = \textit{constant}$ is given by

$$\int\int \mathbf{S}\mathbf{A}^\alpha \sqrt{G}\, e_{\alpha\beta} d\theta^\beta d\theta^3 = \int\int S^\alpha_i \mathbf{A}^i \sqrt{G}\, e_{\alpha\beta} d\theta^\beta d\theta^3 = \int\int S^{\alpha i}\mathbf{A}_i \sqrt{G}\, e_{\alpha\beta} d\theta^\beta d\theta^3 \, . \tag{3.15}$$

Recall that the physical length on the coordinate line θ^α corresponding to an increment $d\theta^\alpha$ is $\|\mathbf{A}_{(\alpha)}\| d\theta^{(\alpha)} \equiv \sqrt{G_{(\alpha\alpha)}}\, d\theta^{(\alpha)}$; note that here $e_{\alpha\beta}\theta^\beta = \textit{constant}$ and $\theta^3 = 0$. Hence, on the surface $\theta^\alpha = \hat{\theta}^\alpha$, we can evaluate the stress resultants per unit length of coordinate line at the point $(\hat{\theta}^{\{\alpha\}}, 0) \equiv (\hat{\theta}^1, \hat{\theta}^2, 0)$ to be

$$\mathbf{N}^\alpha := N^{\alpha i}\mathbf{A}_i(\hat{\theta}^{\{\alpha\}},0) = \frac{1}{|\, e_{\alpha\beta}\|\mathbf{A}_\beta(\hat{\theta}^{\{\alpha\}},0)\| \,|} \int_{-1}^{1} S^{\alpha i}\mathbf{A}_i \sqrt{G}\, d\theta^3 \, . \tag{3.16}$$

Similarly, the stress couples per unit length of coordinate line is obtained according to

$$\mathbf{M}^\alpha := M^{\alpha\beta}\mathbf{A}_\beta(\hat{\theta}^{\{\alpha\}},0) = \frac{h(\hat{\theta}^{\{\alpha\}})\mathbf{D}(\hat{\theta}^{\{\alpha\}})}{2\,|\, e_{\alpha\beta}\|\mathbf{A}_\beta(\hat{\theta}^{\{\alpha\}},0)\| \,|} \times \int_{-1}^{1} \theta^3 S^{\alpha i}\mathbf{A}_i \sqrt{G}\, d\theta^3 \, , \tag{3.17}$$

where within an element, $\mathbf{D} = \mathbf{A}_3/\|\mathbf{A}_3\|$ and $\mathbf{A}_3$ is as given in $(3.8)_2$. It should be noted here that $M^\alpha_3 = \mathbf{M}^\alpha \bullet \mathbf{A}_3 = 0$, i.e., there is no stress couple about the normal to the shell mid-surface.

Remark 3.1. The above integral could be computed in the global cartesian coordinate system with base vectors $\{\mathbf{E}_I\}$, then if necessary re-expressed the resultant vector in components with respect to the tangent vectors $\{\mathbf{A}_i\}$ at point $(\hat{\theta}^{\{\alpha\}},0)$. Hence,

$$\begin{aligned}
\mathbf{N}^\alpha &= \frac{1}{\mid e_{\alpha\beta}\|\mathbf{A}_\beta\| \mid}\left(\int_{-1}^{1} S^{\alpha j} A_j^{\mathrm{I}} \sqrt{G}\, d\theta^3\right)\mathbf{E}_{\mathrm{I}} = \frac{1}{\mid e_{\alpha\beta}\|\mathbf{A}_\beta\| \mid}\left(\int_{-1}^{1} S^{\alpha j} A_j^{\mathrm{I}} \sqrt{G}\, d\theta^3\right) A_{\mathrm{I}}^i\, \mathbf{A}_i\,, \\
\mathbf{M}^\alpha &= \frac{h e_{\mathrm{IJK}} D^{\mathrm{J}}}{2 \mid e_{\alpha\beta}\|\mathbf{A}_\beta\| \mid}\left(\int_{-1}^{1} \theta^3 S^{\alpha j} A_j^{\mathrm{K}} \sqrt{G}\, d\theta^3\right)\mathbf{E}_{\mathrm{I}} = \frac{h e_{\mathrm{IJK}} D^{\mathrm{J}}}{2 \mid e_{\alpha\beta}\|\mathbf{A}_\beta\| \mid}\left(\int_{-1}^{1} \theta^3 S^{\alpha j} A_j^{\mathrm{K}} \sqrt{G}\, d\theta^3\right) A_{\mathrm{I}}^i\, \mathbf{A}_i\,,
\end{aligned} \tag{3.18a}$$

where e_{IJK} is the alternating symbol which takes value 1 if (I,J,K) is an even permutation of (1,2,3), and -1 if (I,J,K) is an odd permutation of (1,2,3); it is zero otherwise. In (3.18a), we have omitted, for clarity, the coordinates at which different quantities are to be evaluated. These quantities should be read as follows

$$\begin{aligned}
&\mathbf{A}_i = \mathbf{A}_i(\hat{\theta}^{\{\alpha\}},0)\,, \quad \|\mathbf{A}_\beta\| = \|\mathbf{A}_\beta(\hat{\theta}^{\{\alpha\}},0)\|\,, \quad \sqrt{G} = \sqrt{G(\hat{\theta}^{\{\alpha\}},\theta^3)}\,, \\
&A_j^{\mathrm{I}} = \frac{\partial X^{\mathrm{I}}(\hat{\theta}^{\{\alpha\}},\theta^3)}{\partial \theta^j} \quad \text{where} \quad \mathbf{A}_j = A_j^{\mathrm{I}}\mathbf{E}_{\mathrm{I}}\,, \ \text{(same for } A_j^{\mathrm{K}})\,, \\
&A_{\mathrm{I}}^i = \frac{\partial \theta^i(\hat{X}^{\{\mathrm{J}\}})}{\partial X^{\mathrm{I}}} \quad \text{where} \quad \mathbf{A}^i = A_{\mathrm{I}}^i \mathbf{E}_{\mathrm{I}}\,, \ \text{and } \hat{X}^{\mathrm{J}} = X^{\mathrm{J}}(\hat{\theta}^{\{\alpha\}},0)\,, \\
&S^{\alpha j} = S^{\alpha j}(\hat{\theta}^{\{\beta\}},\theta^3)\,, \quad h = h(\hat{\theta}^{\{\alpha\}})\,, \quad D^{\mathrm{I}} = D^{\mathrm{I}}(\hat{\theta}^{\{\alpha\}})\,. \quad \square
\end{aligned} \tag{3.18b}$$

4. Constitutive laws. Plane stress elasticity

In this section, we give the details relating the strain measures $\boldsymbol{\Gamma}$, $\boldsymbol{\Gamma}^{\#}$, and $\boldsymbol{\Gamma}^{@}$ to their conjugate stresses $\mathbf{S}$, $\mathbf{S}^{@}$, and $\mathbf{S}^{\#}$ with a particular attention to the treatment of plane stress constraints imposed on a shell lamina. It should be noted here that plane stress response is enforced directly in convected coordinates without the use of a local triad or the assumption that the director is normal to the shell lamina.

4.1. Unconstrained elastic moduli tensors

We will use indices in capital roman letters to denote tensors in the global cartesian coordinate system:

$$\begin{aligned}
\boldsymbol{\Gamma} &= \Gamma_{\mathrm{IJ}}\mathbf{E}_{\mathrm{I}} \otimes \mathbf{E}_{\mathrm{J}}\,, \ \text{with } \Gamma_{\mathrm{IJ}} = \Gamma^{\mathrm{IJ}} = \Gamma_{\mathrm{J}}^{\mathrm{I}}\,, \\
\mathbf{S} &= S_{\mathrm{IJ}}\mathbf{E}_{\mathrm{I}} \otimes \mathbf{E}_{\mathrm{J}}\,, \ \text{with } S_{\mathrm{IJ}} = S^{\mathrm{IJ}} = S_{\mathrm{J}}^{\mathrm{I}}\,.
\end{aligned} \tag{4.1}$$

A linear relation between strain tensors and stress tensors is postulated through the use of the fourth order tensor $\mathbf{C} = C_{\mathrm{IJKL}}\mathbf{E}_{\mathrm{I}} \otimes \mathbf{E}_{\mathrm{J}} \otimes \mathbf{E}_{\mathrm{K}} \otimes \mathbf{E}_{\mathrm{L}}$ designating the (unconstrained) elastic moduli tensor,

$$\begin{aligned} S_{\mathrm{IJ}} &= C_{\mathrm{IJKL}}\Gamma_{\mathrm{KL}} \ , \quad S^{i}_{j} = C^{ik}_{jl}\,\Gamma^{l}_{k} \ , \\ S_{ij} &= C_{ijkl}\Gamma^{kl} \ , \quad S^{ij} = C^{ijkl}\Gamma_{kl} \ , \end{aligned} \tag{4.2}$$

where $C_{\mathrm{IJKL}} \equiv C^{\mathrm{IJKL}}$ and

$$C^{ijkl} = C^{\mathrm{IJKL}}\frac{\partial\theta^{i}}{\partial X^{\mathrm{I}}}\frac{\partial\theta^{j}}{\partial X^{\mathrm{J}}}\frac{\partial\theta^{k}}{\partial X^{\mathrm{K}}}\frac{\partial\theta^{l}}{\partial X^{\mathrm{L}}} \ . \tag{4.3}$$

In cartesian coordinates, the unconstrained elastic moduli tensor $\mathbf{C}$ takes the following form (e.g., Green & Zerna [1968])

$$\begin{aligned} C^{\mathrm{IJKL}} &= \lambda\delta^{\mathrm{IJ}}\delta^{\mathrm{KL}} + \mu(\delta^{\mathrm{IK}}\delta^{\mathrm{JL}} + \delta^{\mathrm{IL}}\delta^{\mathrm{JK}}) \ , \\ \lambda := \frac{E\nu}{(1+\nu)(1-2\nu)} \ , &\quad \mu := \frac{E}{2(1+\nu)} \ , \end{aligned} \tag{4.4}$$

where E denotes the Young's modulus, ν the Poisson's ratio, and λ and μ are the Lamé's constants. It follows from (4.3) and (4.4) that

$$C^{ijkl} = \lambda G^{ij}G^{kl} + \mu(G^{ik}G^{jl} + G^{il}G^{jk}) \ . \tag{4.5}$$

The expressions of C^{ik}_{jl} and of C_{ijkl} are obtained by lowering the indices of C^{ijkl}:

$$\begin{aligned} C^{ik}_{jl} &= C^{ipkq}G_{jp}G_{lq} = \lambda\delta^{i}_{j}\delta^{k}_{l} + \mu(G^{ik}G_{jl} + \delta^{i}_{l}\delta^{k}_{j}) \ , \\ C_{ijkl} &= C^{pqrs}G_{ip}G_{jq}G_{kr}G_{ls} = \lambda G_{ij}G_{kl} + \mu(G_{ik}G_{jl} + G_{il}G_{jk}) \ . \end{aligned} \tag{4.6}$$

Remark 4.1. The internal energy W can be expressed fully in terms of strain measures using different types of components by

$$W := \frac{1}{2}\int_{\Omega}\Gamma^{i}_{j}C^{jl}_{ik}\Gamma^{k}_{l}\mathrm{d}\Omega = \frac{1}{2}\int_{\Omega}\Gamma^{ij}C_{ijkl}\Gamma^{kl}\mathrm{d}\Omega = \frac{1}{2}\int_{\Omega}\Gamma_{ij}C^{ijkl}\Gamma_{kl}\mathrm{d}\Omega \ . \tag{4.7}$$

It should be noted here that one could employ any of the above three forms of the internal energy in the finite element discretization with identical results. From the computer implementation point of view, the last two forms are more convenient simply because of the symmetry of the strain tensors $\boldsymbol{\Gamma}^{\#}$ and $\boldsymbol{\Gamma}^{@}$. □

Remark 4.2. The symmetric property of the elastic moduli tensors should be noted:

$$\begin{aligned} C^{ik}_{jl} &= C^{ki}_{lj} , \\ C_{ijkl} = C_{jikl} &= C_{ijlk} = C_{klij} , \\ C^{ijkl} = C^{jikl} &= C^{ijlk} = C^{klij} . \end{aligned} \tag{4.8}$$

The above symmetry reduces the number of independent components in the elastic tensors: 45 for $\mathbf{C} = C^{ik}_{jl}\mathbf{A}^j \otimes \mathbf{A}_i \otimes \mathbf{A}_k \otimes \mathbf{A}^l$, 21 for both $\mathbf{C}^{@} = C_{ijkl}\mathbf{A}^i \otimes \mathbf{A}^j \otimes \mathbf{A}^k \otimes \mathbf{A}^l$ and $\mathbf{C}^{\#} = C^{ijkl}\mathbf{A}_i \otimes \mathbf{A}_j \otimes \mathbf{A}_k \otimes \mathbf{A}_l$. □

4.2. Plane stress constraints

In shell theory, it is commonly assumed that a shell lamina is in a state of plane stress, i.e., the stress component along the normal to a shell lamina, of the contact force acting on that lamina, is zero. The unit normal to a shell lamina is given by the covector $\mathbf{A}^3/\|\mathbf{A}^3\|$, and the contact force acting on the shell lamina with directed area $\mathbf{A}^3$ is $\mathbf{S}\mathbf{A}^3$. Hence

$$(\mathbf{S}\mathbf{A}^3 \bullet \mathbf{A}^3) = 0 \implies S^3_i G^{i3} = S_{ij} G^{3i} G^{3j} = S^{33} = 0 . \tag{4.9}$$

The three equations in (4.9) are the plane stress constraint equations for the three forms of internal energy in (4.7) (or in (3.14)), respectively. These (linear) constraint equations are eliminated in the expressions of the internal energy W prior to the finite element discretization. It is more convenient to arrange the components of stress tensors and strain tensors in column-matrix form, as done in (3.9),

$$\begin{aligned} \{S^i_j\} &= \{S^1_1, S^2_1, S^3_1, S^1_2, S^2_2, S^3_2, S^1_3, S^2_3, S^3_3\}^{\mathrm{T}} \in \mathbf{R}^{9\times 1} , \\ \{S_{ij}\} &= \{S_{11}, S_{22}, S_{23}, S_{31}, S_{12}, S_{33}\}^{\mathrm{T}} \in \mathbf{R}^{6\times 1} . \end{aligned} \tag{4.10}$$

The stress components in $\{S^{ij}\}$ are ordered in the same manner as in $(4.10)_2$. The strain components in $\{\Gamma^i_j\}$ are ordered as in $(4.10)_1$; the strain components in $\{\Gamma^{ij}\}$ are as in (3.9). With the above ordering of components, the stress-strain relation in (4.2) can be written as

$$\{S_j^i\} = [C_{jl}^{ik}]\{\Gamma_k^l\} \ , \quad \{S_{ij}\} = [C_{ijkl}]\{\Gamma^{kl}\} \ , \quad \{S^{ij}\} = [C^{ijkl}]\{\Gamma_{kl}\} \ , \tag{4.11a}$$

where $[C_{jl}^{ik}] \in \mathbf{R}^{9\times 9}$, $[C_{ijkl}] \in \mathbf{R}^{6\times 6}$, and $[C^{ijkl}] \in \mathbf{R}^{6\times 6}$ are symmetric matrices containing the components of the tensors $\mathbf{C}$, $\mathbf{C}^{@}$, and $\mathbf{C}^{\#}$, respectively. As an example, the arrangement of the coefficients C^{ijkl} in the matrix $[C^{ijkl}]$ according to the ordering (3.9) and $(4.10)_2$ is explicitly given below,

$$[C^{ijkl}] = \begin{bmatrix} C^{1111} & C^{1122} & C^{1123} & C^{1131} & C^{1112} & C^{1133} \\ & C^{2222} & C^{2223} & C^{2231} & C^{2212} & C^{2233} \\ & & C^{2323} & C^{2331} & C^{2312} & C^{2333} \\ & & & C^{3131} & C^{3112} & C^{3133} \\ & SYM. & & & C^{1212} & C^{1233} \\ & & & & & C^{3333} \end{bmatrix} . \tag{4.11b}$$

The elimination of the plane stress constraint in the internal energy proceeds as follows.

Proposition 4.1. *Let* $\{y^i\} = [A^{ij}]\{x_j\}$, *where* $\{y^i\} \in \mathbf{R}^{m\times 1}$, $\{x_j\} \in \mathbf{R}^{m\times 1}$, *and* $[A^{ij}] \in \mathbf{R}^{m\times m}$ *is a symmetric matrix. Consider the linear constraint equation* $y^m = \sum_{i=1}^{m-1} \alpha_i y^i$, *and the inner product* $W := \sum_{i=1}^{m} y^i x_i$. *Eliminating* y^m *and* x_m *in* W, *one obtains*

$$W = \sum_{i,j=1}^{m} x_i A^{ij} x_j = \sum_{i,j=1}^{m-1} x_i \bar{A}^{ij} x_j \ , \tag{4.12a}$$

$$\bar{A}^{ij} := A^{ij} + \alpha_k A^{km}\beta^i\beta^j + \frac{A^{im}A^{jm} - \alpha_k(A^{ik} + A^{kj})}{\alpha_p A^{pm} - A^{mm}} \ ,\dagger \tag{4.12b}$$

$$\beta^i := -\frac{\alpha_k A^{ki} - A^{im}}{\alpha_p A^{pm} - A^{mm}} \ ,\dagger \tag{4.12c}$$

where the matrix $[\bar{A}^{ij}] \in \mathbf{R}^{(m-1)\times(m-1)}$ *is symmetric.*

Proof. Substituting the constraint equation $y^m = \sum_{i=1}^{m} \alpha_i y^i$ into the expression of the inner product $W = \sum_{i=1}^{m} y^i x_i$, we obtain

† Summation convention is implied on the repeated indices k and p, which take values in $\{1,\ldots,(m-1)\}$.

$$W = \sum_{i=1}^{m} y^i \left(x_i + \alpha_i x_m \right) . \tag{4.13}$$

Again, using the above constraint equation, x_m could be written as a linear combination of $\{x_1, \ldots, x_{m-1}\}$ as follows

$$\sum_{j=1}^{m} A^{mj} x_j = \sum_{i=1}^{m-1} \alpha_i \sum_{j=1}^{m} A^{ij} x_j \implies x_m = -\sum_{i=1}^{m-1} \frac{\sum_{k=1}^{m-1} \alpha_k A^{ki} - A^{mi}}{\sum_{p=1}^{m-1} \alpha_p A^{pm} - A^{mm}} x_i . \tag{4.14}$$

Thus, $x_m = \sum_{i=1}^{m-1} \beta^i x_i$ where β^i is as defined in (4.12c). Next, the components y^i's are expressed in terms of $\{x_1, \ldots, x_{m-1}\}$,

$$y^i = \sum_{j=1}^{m-1} \left(A^{ij} + A^{im} \beta^j \right) x_j . \tag{4.15}$$

It follows from (4.14) and (4.15) that the inner product W takes the form

$$W = \sum_{i,j=1}^{m-1} x_i \left[A^{ij} + (\alpha_k A^{km}) \beta^i \beta^j + \left(\beta^i \alpha_k A^{kj} + A^{im} \beta^j \right) \right] x_j \ .\dagger \tag{4.16}$$

The first two terms in (4.16) are symmetric with respect to interchanging the indices i and j. Substituting (4.12c) into the third term in (4.16), we obtain

$$\begin{aligned} \beta^i \alpha_k A^{kj} + A^{im} \beta^j &= -\frac{\alpha_k A^{ik} - A^{im}}{\alpha_p A^{pm} - A^{mm}} \alpha_q A^{qj} - A^{im} \frac{\alpha_k A^{kj} - A^{jm}}{\alpha_p A^{pm} - A^{mm}} \\ &= -\frac{\alpha_k \left(A^{ik} + A^{kj} \right) + A^{im} A^{jm}}{\alpha_p A^{pm} - A^{mm}} \ ,\ddagger \end{aligned} \tag{4.17}$$

which is clearly also symmetric with respect to interchanging the indices i and j. □

Let (S_3^3, Γ_3^3), (S_{33}, Γ^{33}), and (S^{33}, Γ_{33}) be the chosen pairs of stress and strain components to be eliminated. Using (4.9) and (4.11), the plane stress elastic moduli tensors $[\overline{C}^{ik}_{jl}] \in \mathbf{R}^{8\times 8}$, $[\overline{C}_{ijkl}] \in \mathbf{R}^{5\times 5}$, and $[\overline{C}^{ijkl}] \in \mathbf{R}^{5\times 5}$ can be computed with the aid of

† Summation convention is implied on the repeated index k, which takes values in $\{1,\ldots,(m-1)\}$.

‡ Summation convention is implied on the repeated indices k, p, and q; these indices take values in $\{1,\ldots,(m-1)\}$.

Proposition 4.1.

Remark 4.3. In setting up the strain-displacement matrix $\mathbf{B}$, one does not need to compute the coefficients corresponding to the strain Γ^3_3, Γ^{33}, or Γ_{33}, depending on the type of formulation chosen. The expression of the internal energy (4.7) with plane stress assumption is now given by

$$W := \frac{1}{2}\int_\Omega \Gamma^i_j \,\overline{C}^{jl}_{ik}\,\Gamma^k_l \,\mathrm{d}\Omega = \frac{1}{2}\int_\Omega \Gamma^{ij}\,\overline{C}_{ijkl}\,\Gamma^{kl}\,\mathrm{d}\Omega = \frac{1}{2}\int_\Omega \Gamma_{ij}\,\overline{C}^{ijkl}\,\Gamma_{kl}\,\mathrm{d}\Omega\ , \tag{4.18a}$$

with $(i,j) \neq (3,3)$, and $(k,l) \neq (3,3)$. This explains the ordering of strain and stress components in (3.9) and (4.10). Let $\overline{\mathbf{B}}_\mathrm{I}$ denote the submatrix of $\mathbf{B}_\mathrm{I}$ without the strain component Γ_{33} — recall that $\mathbf{B}_\mathrm{I}$ is defined in particular in (3.12a) for the formulation using $\boldsymbol{\Gamma}^{@}$. The stiffness matrix coupling the degrees of freedom at node I to those at node J is then

$$\mathbf{K}_{\mathrm{IJ}} = \int_\Omega \overline{\mathbf{B}}_\mathrm{I}^\mathrm{T}\,[\overline{C}^{ijkl}]\,\overline{\mathbf{B}}_\mathrm{J}\,\mathrm{d}\Omega\ . \tag{4.18b}$$

A similar expression is used for the formulation employing the strain $\boldsymbol{\Gamma}$ or $\boldsymbol{\Gamma}^{\#}$. □

Remark 4.4. A special case of Proposition 4.1 should be noted: When $\alpha_i = 0, \forall\ \ i \in \{1,...,(m-1)\}$, i.e., $y^m \equiv 0$, then the expression of $\overline{A}^{ij}$ in (4.12b) takes a simple form

$$\overline{A}^{ij} = A^{ij} - \frac{A^{im}A^{jm}}{A^{mm}}\ . \tag{4.19a}$$

Such is the case of a formulation employing strain components $\{\Gamma_{ij}\}$ and stress components $\{S^{ij}\}$. Moreover, when the director field is normal to the shell lamina, i.e., $G^{3\alpha} = G^{\alpha 3} = 0$, equation (4.19a) applies in all three types of formulation, since the plane stress constraint in (4.9) are then reduced to

$$S^3_3 = S_{33} = S^{33} = 0\ . \quad \square \tag{4.19b}$$

Remark 4.5. Jang & Pinsky [1987] employed an approximation to the strain components $\{\Gamma_{ij}\}$ where high order terms in θ^3 were neglected.† These approximated strains

† A partial description of this approach is also presented in Pinsky & Jang [1987].

are evaluated at special points on a shell lamina; the strains within the element are then obtained by some interpolation scheme. This is the assumed-strain approach where the stiffness matrix is computed with full integration. Plane stress constraint is enforced employing (4.19a) with $S^{33} = 0$. Further, directors are assumed to be normal to the shell lamina (see Remark 2.3). □

5. Reduced integration. Filtering of spurious zero-energy modes

In this section, we discuss the numerical computation of the stiffness matrix in (4.18b). Uniformly reduced integration of the stiffness matrix is adopted to relieve shear and membrane locking. Several properties of the stiffness matrix under reduced integration are studied, especially the ensuing spurious zero-energy modes of shell elements with 4-node bilinear and 9-node Lagrangian interpolation. We propose an efficient method for filtering these spurious zero-energy modes which is insensitive to change of material properties and geometric parameters of the element.

5.1. Zero-energy modes for displacements and rotations

The expressions of spurious zero-energy (hourglass) modes have been derived algebraically for the 4-node Reissner/Mindlin plate element by Belytschko & Tsay [1983], and for the rectangular (flat) 9-node plate element by Belytschko, Ong & Liu [1984]. It was observed in the latter reference that in a large number of numerical examples the same hourglass modes appear regardless of the shape taken by the element. Using the 9-node shell element developed by Hughes & Liu [1981] with uniformly reduced (2×2) integration, Belytschko and co-workers [1985a] have verified via numerical computation that the same hourglass modes as those in the 9-node plate element occur independently of the geometry of the shell element.

The equations obtained in the present approach have a structure that gives a great deal of insight into the problem of spurious zero-energy modes. In particular, we will

give a proof that substantiates the results of numerical experiments stated in the previous paragraph. We consider only the 4-node bilinear and the 9-node Lagrangian shell element in this section. For subsequent developments, we recall here the expressions of finite element interpolation functions (e.g., Zienkiewicz [1978]). For the 4-node bilinear element:

$$\begin{aligned} \{\ (\theta_{\rm I}^1,\ \theta_{\rm I}^2)\ \} &:= \{\ (-1,\ -1),\ (1,\ -1),\ (1,\ 1),\ (-1,\ 1)\ \}\ , \\ P_{\rm I}(\theta^{\{\alpha\}}) &:= \frac{1}{4}(1\ +\ \theta_{(\rm I)}^1\theta^1)(1\ +\ \theta_{(\rm I)}^2\theta^2)\ ,\quad \text{for I}\ =\ 1,2,3,4\ . \end{aligned} \tag{5.1}$$

For the 9-node Lagrangian element:

$$\begin{aligned} \{\ (\theta_{\rm I}^1,\ \theta_{\rm I}^2)\ \} &:= \{\ (-1,\ -1),\ (1,\ -1),\ (1,\ 1),\ (-1,\ 1),\ (0,\ -1),\ (1,\ 0),\ (0,\ 1),\ (-1,\ 0),\ (0,\ 0)\ \}\ , \\ P_{\rm I}(\theta^{\{\alpha\}}) &:= \frac{\theta^1(\theta^1-\theta_{\rm I}^1)}{2}\frac{\theta^2(\theta^2-\theta_{\rm I}^2)}{2}\ ,\quad \text{for I}\ =\ 1,2,3,4\ , \\ P_{\rm I}(\theta^{\{\alpha\}}) &:= \Big(1-(\theta^1)^2\Big)\frac{\theta^2(\theta^2-\theta_{\rm I}^2)}{2}\ ,\quad \text{for I}\ =\ 5,7\ , \\ P_{\rm I}(\theta^{\{\alpha\}}) &:= \frac{\theta^1(\theta^1-\theta_{\rm I}^1)}{2}\Big(1-(\theta^2)^2\Big)\ ,\quad \text{for I}\ =\ 6,8\ , \\ P_9(\theta^{\{\alpha\}}) &:= \Big(1-(\theta^1)^2\Big)\Big(1-(\theta^2)^2\Big)\ . \end{aligned} \tag{5.2}$$

Define the matrices $\mathbf{r}\in\mathbf{R}^N$ and $\mathbf{z}\in\mathbf{R}^N$ as follows

$$\begin{aligned} \mathbf{r} &:= \{\ r_{\rm I}\ \} = \{\ +1,\ +1,\ +1,\ +1\ \}^{\rm T}\ ,\ \text{for}\ N\ =\ 4\ , \\ \mathbf{z} &:= \{\ z_{\rm I}\ \} = \{-1,\ +1,\ -1,\ +1\ \}^{\rm T}\ ,\ \text{for}\ N\ =\ 4\ , \\ \mathbf{r} &:= \{\ r_{\rm I}\ \} = \{\ +1,\ +1,\ +1,\ +1,\ +1,\ +1,\ +1,\ +1,\ +1\ \}^{\rm T}\ ,\ \text{for}\ N\ =\ 9\ , \\ \mathbf{z} &:= \{\ z_{\rm I}\ \} = \{\ -1,\ -1,\ -1,\ -1,\ +1,\ +1,\ +1,\ +1,\ 0\ \}^{\rm T}\ ,\ \text{for}\ N\ =\ 9\ . \end{aligned} \tag{5.3}$$

Thus, for example, $\{u_{\rm I}^{(i)}\} := \{u_1^i\ ,\ \ldots\ ,\ u_N^i\}^{\rm T} = \mathbf{r}$ is the rigid body mode along the direction $\mathbf{e}_i$, and $\{u_{\rm I}^{(i)}\} = \mathbf{z}$ is the spurious zero-energy (hourglass) mode of displacement in the direction $\mathbf{e}_i$. Let $\chi_{\rm I}^\alpha = 0$ and $u_{\rm I}^i = r_{\rm I}$, for $\alpha = 1,2$ and I = 1,...,N. It can be easily seen from (3.13) that all strain components are zero since

$$\{\ P_{1,1}\ ,\ \ldots\ ,\ P_{N,1}\ \}\ \mathbf{r} = 0\ ,\quad \{\ P_{1,2}\ ,\ \ldots\ ,\ P_{N,2}\ \}\ \mathbf{r} = 0\ , \tag{5.4}$$

and so is the energy, $W = 0$. The computation of W by uniformly reduced integration, which result is denoted by $\widetilde{W}$, introduces additional (spurious) zero-energy modes.

Proposition 5.1. *Let* (i,j,k) *be a cyclic permutation of* (1,2,3). *Consider the case with zero rotation* $\boldsymbol{\chi}_I = 0$, $\forall$ I. *Then regardless of the shape of the shell element, the displacement* $\mathbf{u} = \sum_{I=1}^{N} P_I \mathbf{u}_I$ *where* $\{ u_I^{(i)} \} = \mathbf{z}$, *and* $\{u_I^{(j)}\} = \{u_I^{(k)}\} = 0$, *produces zero strains at the (uniformly) reduced-integration points,* $\forall \ \theta^3 \in [-1, 1]$, *and* $\widetilde{W} = 0$.

Proof. Using (5.1) and (5.2), it can be easily verified that for the 4-node ($N = 4$) bilinear interpolation with one-point integration at $(\theta^{\{\alpha\}}) = (0, 0)$, and for the 9-node ($N = 9$) Lagrangian interpolation with 2×2 integration points at $(\theta^{\{\alpha\}}) = (\pm \frac{1}{\sqrt{3}}, \pm \frac{1}{\sqrt{3}})$, we have

$$\{ P_{1,1} , \ldots , P_{N,1} \} \ \mathbf{z} = 0 , \quad \{ P_{1,2} , \ldots , P_{N,2} \} \ \mathbf{z} = 0 . \tag{5.5}$$

Hence, from (3.13a), it can be easily seen that $\mathbf{B}_{dis}^{(i)}\{u_I^{(i)}\} = 0$, regardless of the components of the tangent vectors $\mathbf{A}_i = A_i^I \mathbf{E}_I$. Hence, it follows that the strains at the reduced-integration points are zero independently of the shape of the element. Note that the fifth row in the matrix $\mathbf{B}_{dis}^{(i)}$ is a linear combination of the other rows. □

Proposition 5.2. *Consider now the case with zero displacement,* $\mathbf{u}_I = 0$, $\forall$ I. *Assume that the director field* $\mathbf{D}$ *and the thickness* h *are constant over the shell surface, i.e.,* $\mathbf{D}(\theta^{\{\alpha\}}) = \hat{\mathbf{D}}$, *and* $h(\theta^{\{\alpha\}}) = \hat{h}$, $\forall$ $(\theta^{\{\alpha\}})$, *for some* $\hat{\mathbf{D}}$ *and* $\hat{h}$. *Then regardless of the shape of the shell element, the nodal rotations such that* $\{ \chi_I^{\{\alpha\}} \} = \mathbf{z}$ *for the 4-node element, and* $\{ \chi_I^{\{\alpha\}} \} = \mathbf{r} - 3\mathbf{z}$ *for the 9-node element, with* $e_{\alpha\beta}\chi_I^{\beta} = 0$, $\forall$ I, *produces zero strains at the reduced-integration points,* $\forall \ \theta^3 \in [-1, 1]$, *and* $\widetilde{W} = 0$.

Proof. Let $(\hat{\mathbf{D}}, \hat{\mathbf{T}}_1, \hat{\mathbf{T}}_2)$ be the orthonormal triad computed as stated in Proposition 2.1. Then $\mathbf{T}_{\beta I} = \hat{\mathbf{T}}_\beta$, $\forall$ I. The expression of $\mathbf{B}_{rot}^{\alpha}$ in (3.13b) can be rewritten as follows

$$\mathbf{B}_{rot}^{\alpha} = \frac{1}{2} e_{\alpha\beta} \begin{bmatrix} \theta^3 \hat{h}(\mathbf{A}_1 \bullet \hat{\mathbf{T}}_\beta) \left\{ P_{1,1} , \cdots , P_{N,1} \right\} \\ \theta^3 \hat{h}(\mathbf{A}_2 \bullet \hat{\mathbf{T}}_\beta) \left\{ P_{1,2} , \cdots , P_{N,2} \right\} \\ \hat{h}\hat{\mathbf{T}}_\beta \bullet \left\{ (P_{1,2}\theta^3\mathbf{A}_3 + P_1\mathbf{A}_2) , \cdots , (P_{N,2}\theta^3\mathbf{A}_3 + P_N\mathbf{A}_2) \right\} \\ \hat{h}\hat{\mathbf{T}}_\beta \bullet \left\{ (P_{1,1}\theta^3\mathbf{A}_3 + P_1\mathbf{A}_1) , \cdots , (P_{N,1}\theta^3\mathbf{A}_3 + P_N\mathbf{A}_1) \right\} \\ \hat{h}\theta^3\hat{\mathbf{T}}_\beta \bullet \left\{ (P_{1,1}\mathbf{A}_2 + P_{1,2}\mathbf{A}_1) , \cdots , (P_{N,1}\mathbf{A}_2 + P_{N,2}\mathbf{A}_1) \right\} \\ \hat{h}(\mathbf{A}_3 \bullet \hat{\mathbf{T}}_\beta) \left\{ P_1 , \cdots , P_N \right\} \end{bmatrix} \in \mathbb{R}^{8\times N} . \tag{5.6}$$

From (5.1) and (5.2), it can be verified that at the reduced-integration points

$$\begin{aligned} \{ P_1, \ldots, P_N \}\, \mathbf{z} &= 0, \quad \text{for } N = 4, \\ \{ P_1, \ldots, P_N \}\, (\mathbf{r} - 3\mathbf{z}) &= 0, \quad \text{for } N = 9. \end{aligned} \tag{5.7}$$

Thus, using (5.7) together with (5.4) and (5.5) in the expression of $\mathbf{B}^{\alpha}_{rot}$ in (5.6), we obtain $\mathbf{B}^{\alpha}_{rot}\mathbf{z} = 0$, for $N = 4$, and $\mathbf{B}^{\alpha}_{rot}(\mathbf{r} - 3\mathbf{z}) = 0$, for $N = 9$, independently of the tangent vectors $\mathbf{A}_i$'s, and for all $\theta^3 \in [-1, 1]$. Hence, the spurious zero-energy mode $\mathbf{z}$ for the 4-node element, and $(\mathbf{r} - 3\mathbf{z})$ for the 9-node element are invariant with respect to the shape taken by the shell element. □

Remark 5.1. Note that in Proposition 5.2 even though the director field $\mathbf{D}$ is assumed to be constant, the shell mid-surface is not assumed to be flat; in fact, is is shown that the results hold for any shape taken by the shell mid-surface. □

Remark 5.2. We consider in Proposition 5.2 a very special case where both the director field and the thickness are constant. In the general case where the director field and the thickness over the shell are arbitrary, the rotations $\mathbf{z}$ for the 4-node element and $(\mathbf{r} - 3\mathbf{z})$ for the 9-node element do not necessarily produce zero strains at the reduced-integration points, and therefore are not in general the spurious zero-energy modes for the rotation. □

Proposition 5.3. *Let* $\mathbf{z}_\beta := \{z_{\beta i}\} \in \mathbf{R}^N$ *belong to the (column) null-space of the matrix* $\mathbf{P}_\beta$, *i.e.,* $\mathbf{P}_{(\beta)}\mathbf{z}_{(\beta)} = 0$, *defined by*

$$\mathbf{P}_\beta := \begin{bmatrix} h_1 P_{1,1}\{T^i_{\beta 1}\} & | \cdots | & h_N P_{N,1}\{T^i_{\beta N}\} \\ h_1 P_{1,2}\{T^i_{\beta 1}\} & | \cdots | & h_N P_{N,2}\{T^i_{\beta N}\} \\ h_1 P_1\{T^i_{\beta 1}\} & | \cdots | & h_N P_N\{T^i_{\beta N}\} \end{bmatrix} \in \mathbf{R}^{9\times N}, \tag{5.8}$$

where $\{T^i_{(\beta 1)}\} := \{T^1_{\beta 1}, T^2_{\beta 1}, T^3_{\beta 1}\}^{\mathrm{T}}$. *Then* $\mathbf{z}_\beta$ *belongs to the null space of* $\mathbf{B}^{\beta}_{rot}$, *i.e.,* $\mathbf{B}^{(\beta)}_{rot}\mathbf{z}_{(\beta)} = 0$, *regardless of the shape of the shell element, and for all* $\theta^3 \in [-1, 1]$.

Proof. The proof can be easily obtained by rewriting (3.13b) as follows

$$\mathbf{B}^{\beta}_{rot} = \frac{1}{2} e_{\alpha\beta} \begin{bmatrix} \theta^3\mathbf{A}_1 & 0 & 0 \\ 0 & \theta^3\mathbf{A}_2 & 0 \\ 0 & \theta^3\mathbf{A}_3 & \mathbf{A}_2 \\ \theta^3\mathbf{A}_3 & 0 & \mathbf{A}_1 \\ \theta^3\mathbf{A}_2 & \theta^3\mathbf{A}_1 & 0 \\ 0 & 0 & \mathbf{A}_3 \end{bmatrix} \bullet \begin{bmatrix} h_1 P_{1,1}\mathbf{T}_{\beta 1}\,,\ \ldots\,,\ h_N P_{N,1}\mathbf{T}_{\beta N} \\ h_1 P_{1,2}\mathbf{T}_{\beta 1}\,,\ \ldots\,,\ h_N P_{N,2}\mathbf{T}_{\beta N} \\ h_1 P_1 \mathbf{T}_{\beta 1}\,,\ \ldots\,,\ h_N P_N \mathbf{T}_{\beta N} \end{bmatrix}. \tag{5.9}$$

□

Further, it is clear that

Corollary 5.1. *If Proposition 5.3 holds with the same* $\mathbf{z}_\beta$ *at all of the reduced-integration points, then* $\mathbf{z}_\beta$ *is the spurious zero-energy mode for the rotation degree of freedom* $e_{\alpha\beta}\chi^\alpha$*, regardless of the shape taken by the shell element.* □

Corresponding to each component T^i_β, define the matrix

$$\mathbf{P}^i_\beta := \begin{bmatrix} h_1 P_{1,1} T^i_{\beta 1}\,,\ \ldots\,,\ h_N P_{N,1} T^i_{\beta N} \\ h_1 P_{1,2} T^i_{\beta 1}\,,\ \ldots\,,\ h_N P_{N,2} T^i_{\beta N} \\ h_1 P_1 T^i_{\beta 1}\,,\ \ldots\,,\ h_N P_N T^i_{\beta N} \end{bmatrix} \in \mathbf{R}^{3\times N}\,. \tag{5.10}$$

Corollary 5.2. *Consider the case of a 4-node element where* $N = 4$*. Let* $i \in \{1,2,3\}$ *such that the matrix* $\mathbf{P}^i_\beta \in \mathbf{R}^{3\times 4}$ *has full row rank. If* $\mathbf{P}_\beta \in \mathbf{R}^{9\times 4}$ *in (5.8) evaluated at the reduced-integration point* $(\theta^{\{\alpha\}}) = (0, 0)$ *has a row rank equal to 3, then regardless of the shape of the element the spurious zero-energy mode for the rotation field* $e_{\alpha\beta}\chi^\alpha$ *is given by*

$$\mathbf{z}_\beta = \{\, z_{\beta \mathrm{I}} \,\} := \left\{ \frac{z_{\mathrm{I}}}{\lambda_{\mathrm{I}}} \right\}, \quad \lambda_{\mathrm{I}} := \begin{cases} h_{(\mathrm{I})} T^i_{\beta(\mathrm{I})}\,, & \text{if } h_{(\mathrm{I})} T^i_{\beta(\mathrm{I})} \neq 0\,, \\ 0\,, & \text{otherwise}\,, \end{cases} \tag{5.11}$$

where $\mathbf{z} = \{\, z_{\mathrm{I}} \,\}$ *is as defined in* $(5.3)_2$.

Proof. From (5.10) and (5.11), we have

$$\mathbf{P}^i_{(\beta)}\mathbf{z}_{(\beta)} = \begin{bmatrix} P_{1,1}\,,\ \ldots\,,\ P_{4,1} \\ P_{1,2}\,,\ \ldots\,,\ P_{4,2} \\ P_1\,,\ \ldots\,,\ P_4 \end{bmatrix} \mathbf{z} = 0\,, \tag{5.12}$$

by virtue of (5.5) and $(5.7)_1$. Since $\mathbf{P}_\beta$ has a row rank of 3, and $\mathbf{P}^i_\beta$ has full row rank, it

follows that $\mathbf{P}_\beta \mathbf{z} = 0$. □

Remark 5.3. For the 9-node element, it is not clear how to obtain an algebraic expression for the spurious zero-energy mode(s) of the rotation field in the general case. Define the matrix

$$\overline{\mathbf{P}}_\beta := \begin{bmatrix} \mathbf{P}_\beta(\frac{-1}{\sqrt{3}}, \frac{-1}{\sqrt{3}}) \\ \mathbf{P}_\beta(\frac{1}{\sqrt{3}}, \frac{-1}{\sqrt{3}}) \\ \mathbf{P}_\beta(\frac{1}{\sqrt{3}}, \frac{1}{\sqrt{3}}) \\ \mathbf{P}_\beta(\frac{-1}{\sqrt{3}}, \frac{1}{\sqrt{3}}) \end{bmatrix} \in \mathbb{R}^{36\times 9}, \tag{5.13a}$$

which includes all matrices $\mathbf{P}_\beta$ evaluated at the reduced-integration points, and whose maximal rank is equal to 9. If there is a vector $\mathbf{v} \in \mathbb{R}^9$ which is independent of all the row vectors of $\overline{\mathbf{P}}_\beta$, then one can find a vector in the (column) null space of $\overline{\mathbf{P}}_\beta$ as a linear combination of $\mathbf{v}$ and the rows of $\overline{\mathbf{P}}_\beta$ (by using for example the Gram-Schmidt orthogonalization process). Corresponding to each component T^i_β, define the matrix

$$\overline{\mathbf{P}}^i_\beta := \begin{bmatrix} \mathbf{P}^i_\beta(\frac{-1}{\sqrt{3}}, \frac{-1}{\sqrt{3}}) \\ \mathbf{P}^i_\beta(\frac{1}{\sqrt{3}}, \frac{-1}{\sqrt{3}}) \\ \mathbf{P}^i_\beta(\frac{1}{\sqrt{3}}, \frac{1}{\sqrt{3}}) \\ \mathbf{P}^i_\beta(\frac{-1}{\sqrt{3}}, \frac{1}{\sqrt{3}}) \end{bmatrix} \in \mathbb{R}^{12\times 9}, \tag{5.13b}$$

where $\mathbf{P}^i_\beta$ is as defined in (5.10). It is easy to verify that a vector in the null space of $\overline{\mathbf{P}}^i_\beta$ is given by

$$\mathbf{z}^i_\beta = \{ z^i_{\beta I} \} := \left\{ \frac{r_I - 3z_I}{\lambda_I} \right\} \in \mathbb{R}^9, \tag{5.13c}$$

where $\mathbf{r} = \{ r_I \}$ and $\mathbf{z} = \{ z_I \}$ for the 9-node have been defined in $(5.3)_{3,4}$, and λ_I is as defined in $(5.11)_2$. Thus, $(\mathbf{z}^1_\beta, \mathbf{z}^2_\beta, \mathbf{z}^3_\beta)$ could be a good starting point as candidates for the vector $\mathbf{v}$ mentioned above. It should be noted that in the case of constant director field and constant thickness, $\mathbf{z}^i_\beta$ reduces exactly to $(\mathbf{r} - 3\mathbf{z})$, with some multiplicative factor. □

Finally, the geometry of the shell element is related to the hourglass mode $\mathbf{z}$ as follows

Proposition 5.4. *Given a geometry* $\{\hat{\mathbf{X}}_\mathrm{I}\}$, *and a director field* $\{\hat{\mathbf{D}}_\mathrm{I}\}$ *for* $\mathrm{I} \in \{1,...,N\}$. *Consider a family of shell elements whose geometry differs by the hourglass mode* $\mathbf{z}$

$$\left\{ \{\mathbf{X}_{\mathrm{I}e}\},\ \mathrm{I} = 1,...,N,\ e = 1,2,...\ |\ \mathbf{X}_{\mathrm{I}e} = \hat{\mathbf{X}}_\mathrm{I} + z_\mathrm{I}\mathbf{c}_e\ ,\ \text{and}\ \mathbf{D}_{\mathrm{I}e} \equiv \hat{\mathbf{D}}_\mathrm{I} \right\}, \tag{5.14}$$

for all arbitrary $\mathbf{c}_e = c_e^\mathrm{I}\mathbf{E}_\mathrm{I}$, *with* $c_e^\mathrm{I} \in \mathbf{R}$. *The family of elements (5.14) forms an equivalent class whose members have the same under-integrated stiffness matrix as that of the representative element with geometry* $\{\hat{\mathbf{X}}_\mathrm{I}\}$ *and director field* $\{\hat{\mathbf{D}}_\mathrm{I}\}$.

Proof. From (3.8), we obtain

$$\mathbf{A}_{\alpha e} = \sum_{\mathrm{I}=1}^{N} P_{\mathrm{I},\alpha}\left[\ \hat{\mathbf{X}}_\mathrm{I} + z_\mathrm{I}\mathbf{c}_e + \theta^3\frac{h_\mathrm{I}}{2}\hat{\mathbf{D}}_\mathrm{I}\ \right],\quad \mathbf{A}_{3e} = \sum_{\mathrm{I}=1}^{N} P_\mathrm{I}\frac{h_\mathrm{I}}{2}\,\hat{\mathbf{D}}_\mathrm{I} \equiv \hat{\mathbf{A}}_3\ . \tag{5.15}$$

By invoking the equalities in (5.5) at the reduced-integration points, we have $\mathbf{A}_{\alpha e} \equiv \hat{\mathbf{A}}_\alpha$. Thus, the metric tensor of all elements in the family is that of the representative element: $[G_{ij}] \equiv [\hat{G}_{ij}]$. Further, since the field of triad $\{\hat{\mathbf{D}},\ \hat{\mathbf{T}}_1,\ \hat{\mathbf{T}}_2\}$ is the same for all elements in (5.14), the conclusion follows from (3.13), (4.5), and (4.6). □

5.2. Filtering of spurious zero-energy modes

The general filtering scheme. The method employed here to filter the spurious zero-energy modes from an under-integrated stiffness matrix is by means of a series of rank-one perturbations on the stiffness matrix. The stiffness matrix can be written as an assemblage of sub-matrices (recall the notation used in (4.18b))

$$\mathbf{K} = \int_{\Omega_e} \overline{\mathbf{B}}^\mathrm{T}\,[\overline{C}^{ijkl}]\,\overline{\mathbf{B}}\mathrm{d}\Omega$$

$$= \int_{\Omega_e} \underset{\substack{i\,\in\,\{1,2,3\}\\ \alpha\,\in\,\{1,2\}}}{A} \left[\ \left(\overline{\mathbf{B}}^i_{dis}\right)^\mathrm{T}[\overline{C}^{pqrs}]\overline{\mathbf{B}}^i_{dis} \oplus \left(\overline{\mathbf{B}}^\alpha_{rot}\right)^\mathrm{T}[\overline{C}^{pqrs}]\overline{\mathbf{B}}^\alpha_{rot} \oplus \left(\overline{\mathbf{B}}^i_{dis}\right)^\mathrm{T}[\overline{C}^{pqrs}]\overline{\mathbf{B}}^\alpha_{rot} \oplus \left(\overline{\mathbf{B}}^\alpha_{rot}\right)^\mathrm{T}[\overline{C}^{pqrs}]\overline{\mathbf{B}}^i_{dis}\ \right]\mathrm{d}\Omega\ , \tag{5.16}$$

where the symbols A and $\oplus$ are used to designate the assembling process. Let

$\bar{\mathbf{b}}^i_{dis} \in \mathbf{R}^9$ and $\bar{\mathbf{b}}^\alpha_{rot} \in \mathbf{R}^9$. By rank-one perturbations of the under-integrated stiffness $\widetilde{\mathbf{K}}$, we mean

$$\mathbf{K}^* = \widetilde{\mathbf{K}} + \delta\mathbf{K}\,, \quad \delta\mathbf{K} := \underset{\substack{i \in \{1,2,3\} \\ \alpha \in \{1,2\}}}{A} \left[\bar{\mathbf{b}}^i_{dis} \left(\bar{\mathbf{b}}^i_{dis}\right)^{\mathrm{T}} \oplus \bar{\mathbf{b}}^\alpha_{rot} \left(\bar{\mathbf{b}}^\alpha_{rot}\right)^{\mathrm{T}} \right], \tag{5.17}$$

where $\|\delta\mathbf{K}\| << \|\mathbf{K}\|$ (Belytschko *et al* [1984,85]).† The choice of $\delta\mathbf{K} = \epsilon\mathbf{K}$, with ϵ being a very small number and $\mathbf{K}$ the fully-integrated stiffness, is a simple, but expensive, filtering scheme.

The vectors $\bar{\mathbf{b}}^i_{dis}$ and $\bar{\mathbf{b}}^\alpha_{rot}$ are chosen such that they are not orthogonal to the spurious zero-energy modes — hence these modes are filtered from the under-integrated stiffness $\widetilde{\mathbf{K}}$ — and that they maintain as much as possible the consistency of the element. To maintain consistency of the element, $\bar{\mathbf{b}}^i_{dis}$ must be orthogonal to the linear displacement field, and $\mathbf{b}^\alpha_{rot}$ must be orthogonal to the constant rotation field, since these displacement and rotation produces a state of constant strains which appears as the size of an element tends to zero. It has been shown that the 9-node Lagrangian element is able to reproduce quadratic displacement field (Wachspress [1981]), particularly when its geometry is restricted to the isoparametric mapping of a 4-node element. In this case, the 9-node element is flat and takes the form of a quadrilateral with mid-side nodes exactly in the middle of each side; the interior node inside the element must be exactly on the intersection of two lines passing through the mid-side nodes. This type of 9-node elements passes the patch test of pure bending where the displacement field is quadratic (Taylor *et al* [1986], Huang & Hinton [1986]). Hence, for the 9-node shell element to perform well in this situation, we further require that $\bar{\mathbf{b}}^i_{dis}$ to be orthogonal to the quadratic displacement field when the element is flat.

The construction of $\bar{\mathbf{b}}^i_{dis}$ and $\bar{\mathbf{b}}^\alpha_{rot}$. Let $\{\mathbf{b}_1, \ldots, \mathbf{b}_m\}$ be m vectors in $\mathbf{R}^N$. Further let $\bar{\mathbf{b}}^i_{dis} = \bar{\mathbf{b}}^\alpha_{rot} = \bar{\mathbf{b}} = \{\bar{b}_I\} \in \mathbf{R}^N$, and define a general form of $\bar{\mathbf{b}}$ to be

† The rank of $\delta\mathbf{K}$ here is of course 5.

$$\bar{\mathbf{b}} := \alpha_o \mathbf{z} + \sum_{i=1}^{m} \alpha_i \mathbf{b}_i \ , \tag{5.18}$$

where $\{\alpha_o, \ldots, \alpha_m\}$ are coefficients to be determined. Let $\{\mathbf{w}_1, \ldots, \mathbf{w}_m\}$ be vectors in $\mathbf{R}^N$. Given a coefficient $c \in \mathbf{R}\backslash\{0\}$, the general problem we want to solve is to

$$\textit{Find } \{\alpha_o, \ldots, \alpha_m\} \textit{ such that } \bar{\mathbf{b}} \bullet \mathbf{z} = c \neq 0 \ , \textit{ and } \bar{\mathbf{b}} \bullet \mathbf{w}_i = 0 \ , \forall \ i \in \{1,\ldots,m\} \ , \tag{5.19}$$

which amounts to solving the system

$$\mathbf{H} \begin{Bmatrix} \alpha_o \\ . \\ . \\ \alpha_m \end{Bmatrix} = \begin{Bmatrix} c \\ 0 \\ . \\ 0 \end{Bmatrix}, \text{ with } \mathbf{H} := \begin{bmatrix} (\mathbf{z}\bullet\mathbf{z}) & (\mathbf{z}\bullet\mathbf{b}_1) & . & (\mathbf{z}\bullet\mathbf{b}_m) \\ (\mathbf{w}_1\bullet\mathbf{z}) & (\mathbf{w}_1\bullet\mathbf{b}_1) & . & (\mathbf{w}_1\bullet\mathbf{b}_m) \\ . & . & . & . \\ (\mathbf{w}_m\bullet\mathbf{z}) & (\mathbf{w}_m\bullet\mathbf{b}_1) & . & (\mathbf{w}_m\bullet\mathbf{b}_m) \end{bmatrix} \in \mathbf{R}^{(m+1)\times(m+1)} . \tag{5.20}$$

The vectors $\mathbf{w}_i$'s are associated with the constant, linear, and quadratic displacement field as will be explained in detail later. Basically, the components of $\mathbf{w}_i$'s are polynomials in the cartesian coordinates of the nodal points.

Remark 5.4. The structure of $\bar{\mathbf{b}}$ here differs from the generalized gradient "γ" employed by Belytschko and co-workers [1984,85], where it is assumed that $\alpha_o = 1$. These authors only aimed at solving partially problem (5.19) by requiring that $\bar{\mathbf{b}} \bullet \mathbf{w}_i = 0$, $\forall$ i. However, this procedure does not in general ensure that $\bar{\mathbf{b}} \bullet \mathbf{z} \neq 0$. In fact, it is easy to construct example where the second condition in (5.19) is satisfied, but not the first one. □

Remark 5.5. In Belytschko *et al* [1985b], the vectors $\{\mathbf{b}_1, \ldots, \mathbf{b}_m\}$ were obtained from differentiating the shape functions, and are not all linearly independent. A special solution was devised without having to solve a system of linear equations. But this filtering scheme is only consistent with respect to linear displacement field when the element is flat; it is in general inconsistent. □

Note that the system (5.20) is non-symmetric. The problem is solvable if $\det\mathbf{H} \neq 0$. Further, the vectors $\{\mathbf{w}_1, \ldots, \mathbf{w}_m\}$ are not assumed to be independent. The following is clear:

Proposition 5.5. *Assume that* $\{\mathbf{z}, \mathbf{b}_1, \ldots, \mathbf{b}_m\}$ *are linearly independent vectors. Then the system (5.20) is solvable only if* $\{\mathbf{z}, \mathbf{w}_1, \ldots, \mathbf{w}_m\}$ *are linearly independent.* □

However, it is more efficient to solve completely problem (5.19) as follows

Proposition 5.6. *Choose* $\mathbf{b}_i = \mathbf{w}_i, \forall\ i \in \{1,...,m\}$*:*

$$\bar{\mathbf{b}} = \alpha_o \mathbf{z} + \sum_{i=1}^{m} \alpha_i \mathbf{w}_i \ . \tag{5.21}$$

If $\{\mathbf{z}, \mathbf{w}_1, \ldots, \mathbf{w}_m\}$ *are linearly independent, then (5.19) is solvable. Suppose there exists* $\{\beta_o, \ldots, \beta_m\}$ *not all equal to zero such that* $\beta_o \mathbf{z} + \sum_{i=1}^{m} \beta_i \mathbf{w}_i = 0$*. If* $\beta_o \neq 0$*, then (5.19) is not solvable. If* $\beta_o = 0$*, (5.19) is completely solvable.*

Proof. By choosing $\mathbf{b}_i \equiv \mathbf{w}_i$, $\mathbf{H}$ becomes symmetric. If $\{\mathbf{z}, \mathbf{w}_1, \ldots, \mathbf{w}_m\}$ are linearly independent, then by Proposition 5.5 problem (5.19) is solvable. We only need to consider the case of linear dependence between the $\mathbf{w}_i$'s, i.e., $\beta_o \mathbf{z} + \sum_{i=1}^{m} \beta_i \mathbf{w}_i = 0$ and $\beta_o = 0$. Eliminate the redundant vectors $\mathbf{w}_i$'s and reorder such that the remaining vectors $\{\mathbf{z}, \mathbf{w}_1, \ldots, \mathbf{w}_p\}$, with $p < m$, are linearly independent. Next solve for $\{\alpha_o, \ldots, \alpha_p\}$ such that

$$\mathbf{H} \begin{Bmatrix} \alpha_o \\ . \\ . \\ \alpha_p \end{Bmatrix} = \begin{Bmatrix} c \\ 0 \\ . \\ 0 \end{Bmatrix}, \text{ with } \mathbf{H} := \begin{bmatrix} (\mathbf{z}\bullet\mathbf{z}) & (\mathbf{z}\bullet\mathbf{w}_1) & . & (\mathbf{z}\bullet\mathbf{w}_p) \\ (\mathbf{w}_1\bullet\mathbf{z}) & (\mathbf{w}_1\bullet\mathbf{w}_1) & . & (\mathbf{w}_1\bullet\mathbf{w}_p) \\ . & . & . & . \\ (\mathbf{w}_p\bullet\mathbf{z}) & (\mathbf{w}_p\bullet\mathbf{w}_1) & . & (\mathbf{w}_p\bullet\mathbf{w}_p) \end{bmatrix} \in \mathbf{R}^{(p+1)\times(p+1)}, \tag{5.22}$$

and $\bar{\mathbf{b}} = \alpha_o \mathbf{z} + \sum_{i=1}^{p} \alpha_i \mathbf{w}_i$. The vectors $\mathbf{w}_j$'s, for $j = (p+1),...,m$, are linear combinations of $\{\mathbf{w}_1, \ldots, \mathbf{w}_p\}$, i.e., $\mathbf{w}_j = \sum_{i=1}^{p} \bar{\beta}_{ij} \mathbf{w}_i$. Since $\bar{\mathbf{b}}\bullet\mathbf{w}_i = 0$, for $i = 1,...,m$, we have $\bar{\mathbf{b}}\bullet\mathbf{w}_j = 0$, for $j = (p+1),...,m$; and since $\bar{\mathbf{b}}\bullet\mathbf{z} = c$, problem (5.19) is completely solved. □

Remark 5.7. The matrix $\mathbf{H}$ in Proposition 5.6 is not only symmetric, but can also be rendered better conditioned if the vectors $\{\mathbf{z}, \mathbf{w}_1, \ldots, \mathbf{w}_m\}$ are normalized using the

Euclidean norm $\|\cdot\|_2$, defined by

$$\|\mathbf{z}\|_2 = \left[\sum_{I=1}^{N} (z_I)^2 \right]^{\frac{1}{2}} . \tag{5.23}$$

In this case, all diagonal terms are equal to 1, and off-diagonal terms are less than 1 in absolute value. Hence, the problem of solving the linear system (5.22) is in general better conditioned than solving (5.20) using various possible choices of the vectors $\{\mathbf{b}_1, \ldots, \mathbf{b}_m\}$. In addition, the choice $\mathbf{b}_i \equiv \mathbf{w}_i$, $\forall\ i$, provides a natural extension of the base vectors $\mathbf{b}_i$'s when the number of vectors $\mathbf{w}_i$'s increases, as will be seen shortly. □

Remark 5.8. When $\beta_o \neq 0$, then problem (5.19) is unsolvable for any set of independent vectors $\{\mathbf{z}, \mathbf{b}_1, \ldots, \mathbf{b}_m\}$. In this sense, choosing $\mathbf{b}_i \equiv \mathbf{w}_i$, for all $i \in \{1,...,m\}$, represents the best possible choice for the vectors $\{\mathbf{b}_1, \ldots, \mathbf{b}_m\}$. In the case $\beta_o \neq 0$, we let $\bar{\mathbf{b}} = \mathbf{z}$, and thus will not satisfy the requirement that $\bar{\mathbf{b}} \cdot \mathbf{w}_i = 0$, $\forall\ i$. However, this does not mean the filtering procedure does not retain consistency of the element, since by changing the geometry of the element (such as refining the mesh) we will alter the vectors $\mathbf{w}_i$'s, and hence the unsolvability of the problem. The practical implementation aspects of the solution procedure in the proof of Proposition 5.6 are relegated to Appendix II. □

Using the proof of Proposition 5.6, it is simple to obtain the following

Corollary 5.3. *Let* $\{\hat{\mathbf{w}}_1, \ldots, \hat{\mathbf{w}}_m\}$ *where* $\hat{\mathbf{w}}_i$*'s are linear combinations of* $\{\mathbf{w}_1, \ldots, \mathbf{w}_m\}$ *such that the subspace spanned by the vectors* $\hat{\mathbf{w}}_i$*'s is the same as the one spanned by the vectors* $\mathbf{w}_i$*'s. Then problem (5.19) can be solved by using* $\hat{\mathbf{w}}_i$*'s in (5.22) instead of* $\mathbf{w}_i$*'s.* □

The set-up of vectors $\mathbf{w}_i$'s. We want to maintain consistency of the element up to linear displacement field in both the 4-node and the 9-node elements. Hence, the followings are considered

$$\begin{aligned} \mathbf{w}_1 &= \mathbf{r} = \{\ 1\ ,\ \ldots\ ,\ 1\ \}^{\mathrm{T}} \in \mathbf{R}^N\ , \\ \mathbf{w}_{i+1} &= \{\ X_I^{(i)}\ \} = \{\ X_1^i\ ,\ \ldots\ ,\ X_N^i\ \}^{\mathrm{T}} \in \mathbf{R}^N\ ,\ \text{for } i = 1,2,3\ . \end{aligned} \tag{5.24}$$

Except in the case of a flat 9-node element, we want to maintain consistency of the element up to quadratic displacement field as discussed earlier. The additional vectors $\mathbf{w}_i$'s to be considered are presented in matrix form as follows

$$\begin{bmatrix} (X_1^1)^2 & (X_1^2)^2 & (X_1^3)^2 & (X_1^1X_1^2) & (X_1^2X_1^3) & (X_1^3X_1^1) \\ \cdot & \cdot & \cdot & \cdot & \cdot & \cdot \\ \cdot & \cdot & \cdot & \cdot & \cdot & \cdot \\ \cdot & \cdot & \cdot & \cdot & \cdot & \cdot \\ (X_9^1)^2 & (X_9^2)^2 & (X_9^3)^2 & (X_9^1X_9^2) & (X_9^2X_9^3) & (X_9^3X_9^1) \end{bmatrix} \in \mathbf{R}^{9\times 6} . \tag{5.25}$$

There are thus 10 vectors in total, but at most 6 of them are independent. Define an orthonormal triad $\{\hat{\mathbf{T}}_1, \hat{\mathbf{T}}_2, \hat{\mathbf{T}}_3\}$ such that $\{\hat{\mathbf{T}}_1, \hat{\mathbf{T}}_2\}$ are tangent to the shell mid-surface at node 9 (the interior node). Invoking Proposition 5.6 and Corollary 5.3, we define the new set of coordinates

$$\hat{\mathbf{X}}_I = \mathbf{X}_I - \mathbf{X}_9 = \hat{X}_I^J \hat{\mathbf{T}}_J , \text{ with } \hat{X}_I^J := (\mathbf{X}_I \bullet \hat{\mathbf{T}}_J) - X_9^J , \tag{5.26}$$

and use these in (5.24) and (5.25). Note that $(\hat{X}_{(I)}^J)$ are the coordinates of node I with respect to a system of cartesian coordinates with origin at node 9 and with base vectors $\{\hat{\mathbf{T}}_1, \hat{\mathbf{T}}_2, \hat{\mathbf{T}}_3\}$. When the element is flat, $\hat{X}_I^3 \equiv 0$, $\forall$ I. In this case, the $\mathbf{w}_i$'s in (5.24) and (5.25) are replaced by their linear combinations defined in (5.26)

$$\begin{bmatrix} 1 & \hat{X}_1^1 & \hat{X}_1^2 & (\hat{X}_1^1)^2 & (\hat{X}_1^1\hat{X}_1^2) & (\hat{X}_1^2)^2 \\ \cdot & \cdot & \cdot & \cdot & \cdot & \cdot \\ \cdot & \cdot & \cdot & \cdot & \cdot & \cdot \\ \cdot & \cdot & \cdot & \cdot & \cdot & \cdot \\ 1 & \hat{X}_9^1 & \hat{X}_9^2 & (\hat{X}_9^1)^2 & (\hat{X}_9^1\hat{X}_9^2) & (\hat{X}_9^2)^2 \end{bmatrix} \in \mathbf{R}^{9\times 6} . \tag{5.27}$$

Remark 5.9. It is numerically more accurate to make use of the transformation (5.26) and the normalization in Remark 5.7 in all cases. In so doing, we still solve exactly problem (5.19), by Proposition 5.6 and Corollary 5.3, and at the same time avoid numerical ill-conditioning when the coordinates of nodal points have large amplitudes. Further, the transformation (5.26) provides a way to check the flatness of the element.

□

The practical filtering scheme. As explained in (5.17), the filtering of spurious zero-energy modes is done by introducing small perturbations into the stiffness matrix. In order to have a measure of the perturbation, we normalize $\bar{\mathbf{b}}$ using the norm

$$\|\bar{\mathbf{b}}\|_\infty = \max_{I=1,\ldots,N} |\bar{b}_I| \,. \tag{5.28}$$

The magnitude of the perturbation is a fraction of the maximal absolute value of the diagonal coefficients. We propose the following practical filtering scheme

$$\bar{\mathbf{b}}^i_{dis} = \bar{\mathbf{b}}^\alpha_{rot} = \frac{\bar{\mathbf{b}}}{\|\bar{\mathbf{b}}\|_\infty} \,, \tag{5.29a}$$

$$\delta\mathbf{K} = \max_{i=1,\ldots,n} |\widetilde{K}_{(ii)}| \underset{\substack{j\in\{1,2,3\}\\ \alpha\in\{1,2\}}}{A} \left[\epsilon_{dis} \bar{\mathbf{b}}^j_{dis} \left(\bar{\mathbf{b}}^j_{dis}\right)^{\mathrm{T}} \oplus \epsilon_{\mathrm{rot}} \bar{\mathbf{b}}^\alpha_{rot} \left(\bar{\mathbf{b}}^\alpha_{rot}\right)^{\mathrm{T}} \right], \tag{5.29b}$$

where ϵ_{dis} and ϵ_{rot} are perturbation constants (of order 10^{-6}). Clearly, similar to $\widetilde{\mathbf{K}}$, the matrix $\delta\mathbf{K}$, and therefore $\mathbf{K}^*$, are also proportional to the Young's modulus E. It follows that the computed displacement $\boldsymbol{\Delta}$ is exactly proportional to the Young's modulus. In this manner, the filtering scheme is insensitive under change of material properties. In addition, the proposed filtering scheme is shown to be insensitive under change of geometric parameters of the shell element in numerical examples presented shortly.

Remark 5.10. The computation of the perturbation matrix $\delta\mathbf{K}$ in (5.29) is done once for each element. This is contrast to the filtering scheme proposed in Belytschko *et al* [1985a], where at each reduced-integration point a perturbation matrix is added to the stiffness matrix expressed in a local cartesian coordinate system. The perturbed stiffness is then transformed to the global coordinate system. In addition to this operation, 3 coefficients are to be evaluated exactly by full (3×3) integration — while the stiffness is computed by reduced (2×2) integration. □

6. Numerical Examples

In this section, several numerical examples are presented to assess the performance of the shell element formulation and the filtering of spurious zero-energy modes. The shell element with 9-node Lagrangian interpolation has been implemented in the research version of FEAP, a "Finite Element Analysis Program," written by Taylor (a simplified version of this program is presented in Chapter 24 of Zienkiewicz [1978]), and run under the Berkeley Unix 4.3 BSD operating system. This element is subjected to an extensive course of obstacles suggested by several authors (e.g., MacNeal & Harder [1985] and in Forsberg & Fong [1985]).

The following convention is used to report the results obtained from the filtering of spurious zero-energy modes:

- $kf = 0$: No filtering of spurious modes.
- $kf = 1$: Filtering scheme consistent with linear displacement field.
- $kf = 2$: Filtering scheme consistent with quadratic displacement field.
- $kf = 3$: Inconsistent filtering ($\bar{\mathbf{b}} = \mathbf{z}$).

In all examples, we arbitrarily set the constant c in (5.19) to $c = 1$, and the perturbation constants in (5.29b) to $\epsilon_{dis} = \epsilon_{rot} = 10^{-6}$. Also, integration through the thickness is performed throughout with 3 points of integration.

Example 6.1. Patch tests. Consider the square patch of length 10 consisted of shell 9-node elements as shown in Figure 6.1 with material properties $E = 2.1 \times 10^6$ and $\nu = 0.3$ (Huang & Hinton [1986]). The present 9-node element, either in full integration or in reduced integration with filtering of spurious modes, passes both the membrane and pure bending tests — a large range of thickness, $0.0001 \leq h \leq 1$, has been tested. This test is also part of the MacNeal-Harder standard set of problems [1985].

A square plate with length L under pure bending test, with moment per unit length M, yields a transverse displacement which is a polynomial with quadratic terms in the coordinates:

$$u^3(X^{\{\alpha\}}) = \frac{6M}{Eh^3}\left[(X^1)^2 - \nu(X^2)^2 + \frac{\nu L^2}{4}\right]. \tag{6.1}$$

Thus in order to pass this test, the filtering scheme must be consistent up to quadratic displacement field.

Remark 6.1. We have implemented the assumed-strain method and used full integration as suggested in Jang & Pinsky [1987], where an approximation to the strain components Γ_{ij} is used.† This element, in our implementation, could only passes the membrane test, but not the bending test. The same can be said when we try to apply the same assumed-strain scheme to the exact expression of Γ_{ij} without neglecting any terms. However, if we transform the strains Γ_{ij} to the (global) cartesian coordinate system — a costly process — prior to carrying out the assumed-strain scheme, then this element passes the bending test. It should be noted that both Huang & Hinton [1986] and Park & Stanley [1986] applied their assumed-strain scheme to the strain components in local cartesian coordinate systems. It was mentioned in Huang & Hinton [1986] that their element passed the bending patch test. □

Consider now the square plate of length 4, thickness $h = 0.01$, with a specially distorted mesh as shown in Figure 6.1b.† The material properties are $E = 1000$ and $\nu = 0.3$. In connection with Propositions 5.5 and 5.6, the purpose of this test is to consider the case where the matrix of coordinates in (5.27) is not full rank. Such case is presented in the (extremely) narrow element along a diagonal of the plate as shown in Figure 6.1b; its nodal coordinates are tabulated in Table 6.1a below. The plate is subjected to a bending moment per unit length of $M = 3 \times 10^{-5}$ at its tip (with 3 nodes) in the same manner as in the bending patch test. The transverse displacements of the 3 nodes at the tip, normalized with the exact solution, is summarized in Table 6.1b, and a perspective view of the deformed shape is given in Figure 6.1c. It can be observed that the present filtering

† Terms quadratic in θ^3 were neglected by these authors.

† This mesh admits 2 corner nodes with an angle of 180° along two sides of the plate — the jacobian at these 2 nodes is singular.

Table 6.1a. *Coordinates of special element.*

Node	X^1	X^2
1	−2	−2
2	−0.99	−1.01
3	2	2
4	0.99	1.01
5	−1.485	−1.515
6	1	1
7	1.485	1.515
8	−1	−1
9	0	0

Table 6.1b. *Specially distorted mesh. Normalized transverse displacements at tip.*

Coordinates	Exact	Normal. Disp.		
		$kf = 2$	$kf = 3$	Full Int.
(−2, 2)	1.44	1.007	0.923	0.007
(0, 2)	1.548	0.924	0.725	0.087
(+2, 2)	1.44	0.828	0.582	0.258

scheme ($kf = 2$) provides a better result than the inconsistent filtering ($kf = 3$). •

Example 6.2. Thick circular plate. This example is used to test the performance of the element in thick shell structures where shear deformation is important. The circular plate, with clamped boundary condition, has radius $R = 5$, thickness $h = 2$, and material properties $E = 1.09 \times 10^6$, $\nu = 0.3$. A quarter of the plate is modeled with 3 elements as depicted in Figure 6.2a. Figure 6.2b shows both the computed transverse displacement using full integration. The exact solution of this problem can be found in Lukasiewicz [1979,p.114]. •

Example 6.3. Thin rectangular plate. This example is part of the MacNeal-Harder tests, and is used to assess the performance of plate elements against shear locking. The plate has length 10, width 2, and thickness $h = 10^{-4}$, with material properties $E = 1.7472 \times 10^7$, $\nu = 0.3$. Two boundary conditions (simply supported and clamped) and two load cases (uniform pressure at 10^{-4} and point force at 4×10^{-4}) are considered.

Only a quarter of the plate is modeled with uniform meshes of 1, 4, 16, and 64 elements. The computed transverse displacement at the center of the plate is summarized in Table 6.3a.

Table 6.3a. *Thin rectangular plate. Transverse displacement at center.*

Boundary Condition	No. of Elements	Uniform Load		Point Force	
Simply supported		Exact = 12.97		Exact = 16.96	
		$kf = 0$	$kf = 2$	$kf = 0$	$kf = 2$
	4	1.2986e+01	1.2790e+01	1.7263e+01	1.5655e+01
	16	—	1.3006e+01	—	1.6139e+01
	64	—	1.2972e+01	—	1.6673e+01
Clamped		Exact = 2.56		Exact = 7.23	
		$kf = 0$	$kf = 2$	$kf = 0$	$kf = 2$
	1	—	—	6.8766e+00	6.4477e+00
	4	2.8729e+00	2.3342e+00	7.2550e+00	3.5259e+00
	16	—	2.6047e+00	—	5.0105e+00
	64	—	2.6041e+00	—	6.7509e+00

Remark 6.2. Only in one instance, the present filtering scheme ($kf = 2$) with $\epsilon_{dis} = \epsilon_{rot} = 10^{-6}$ yields a clear slower rate of convergence than reduced integration without filtering of spurious modes ($kf = 0$): the case of clamped boundary condition with point force.† However, these results could be sharply improved if the perturbation constant on the rotation (ϵ_{rot}) is chosen to be smaller than the perturbation constant for the displacement (ϵ_{dis}). Using for example $\epsilon_{dis} = 10^{-6}$ and $\epsilon_{rot} = 10^{-8}$, the tranverse displacement at center of the clamped plate under point force is reported in Table 6.3b. The reason is because the stiffness associated with rotations is very small compared with the membrane stiffness. Clearly, for this case, a mesh with finer discretization around the point force and coarser discretization near the clamped boundary would give a better result. The purpose of using uniform discretization here, however, is to compare with

† The results for the square plate (with aspect ratio 1) agree very well with the exact solution in all situations, including the case with clamped boundary conditions and point force. This is why we chose to present only results for the rectangular plate.

Table 6.3b. *Thin rectangular plate. Transverse displacement at center. Perturbation constants:* $\epsilon_{dis} = 10^{-6}$, $\epsilon_{rot} = 10^{-8}$.

Boundary Condition	No. of Elements	Point Force	
		Exact = 7.23	
		$kf = 0$	$kf = 2$
Clamped	1	6.8766e+00	6.4563e+00
	4	7.2550e+00	5.4280e+00
	16	—	6.7753e+00
	64	—	7.1369e+00

published results by MacNeal and Harder. □ •

Example 6.4. Square plate with corner point-supports. This example was used by Belytschko, Ong & Liu [1984] to look for an appropriate value of r_w associated with the transverse displacement, a multiplicative factor in their proposed perturbation matrix $\delta\mathbf{K}$. The plate has length $L = 10$, thickness $h = 0.01$, and material properties $E = 10^7$ and $\nu = 0.3$. Depending on the magnitude of the value of r_w, they obtained different results compared to the exact solution: oscillations in the transverse displacement for small value of r_w (0.01), and acceptable results for $r_w \geq 0.1$. The oscillation obtained when using $r_w = 0.01$ is probably due to the fact that their filtering scheme does not completely eliminate the hourglass mode for such a small value of r_w. In the cases with $r_w \geq 0.1$, one observes as expected a stiffening effect as the value of r_w increases. These authors recommended the optimal value $r_w = 0.1$ for general use, as it produced results closest to the exact solution in this example.

A quarter of the plate is modeled. Figure 6.4a shows the computed transverse displacement along a centerline as obtained in the present approach for a mesh of 2×2 elements and for a mesh of 8×8 elements. In this example, the filtering of spurious zero-energy modes is crucial as can be seen from the results in Table 6.4. The convergence of the transverse displacement at the center of the plate obtained different types of filtering is reported in in Figure 6.4b. The displacements in Table 6.4 are normalized with

Table 6.4. *Square plate with corner point-supports. Transverse displacement along center line.*

X^1 Coord.	No filtering, $kf = 0$	Filtering, $kf = 2$
0.00	$-5.0504e-01$	$-2.5961e+00$
1.25	$-8.7265e+09$	$-2.5335e+00$
2.50	$-5.1206e-01$	$-2.3457e+00$
3.75	$-8.7265e+09$	$-2.0912e+00$
5.00	$-5.5357e-01$	$-1.8284e+00$

respect to the referential value of -2.788811 obtained from an 8×8 mesh (i.e., mesh size 0.625). The theoretical formula for the transverse displacement can be found in Timoshenko & Woinowsky-Krieger [1959]. It should be noted that due to the simplicity of formula (5.28) the above results are obtained without the need of parameter tuning. •

Example 6.5. Simply supported rhombic plate under uniform loading. This example, whose geometry is depicted in Figure 6.5a, is often used to test the performance of plate elements. The difficulty in this example lies in the singularity of the moments — the stress tends to infinity — at the obtuse vertices. This type of singularity is predicted in both the Kirchhoff plate theory as well as in the Reissner/Mindlin plate theory as noted in Morley [1963,p.89]. The length of each side of the plate is 100, the obtuse vertices have an angle of 150°, the acute vertices have an angle of 30°, and the plate has a thickness of 0.1. The material properties are $E = 10^7$, $\nu = 0.3$.

Two types of finite element mesh are used to discretize the (whole) rhombic plate: (A) uniform discretization — all elements have identical stiffness matrix, and (B) uniform discretization with one exception: We move the 3 nodes closest to an obtuse vertex to the "quarter-points" from that vertex as shown in Figure 6.5b. The mesh of type B is inspired from the treatment of singularity points in fracture mechanics by exploiting the properties of isoparametric coordinate mapping, as proposed by Henshell & Shaw [1975] and by Barsoum [1976]. Recall that the Morley solution as plotted in Figures 6.5c and 6.5d involves certain approximation, and is used here as a reference.

In this example, the internal forces are presented with respect to the global cartesian coordinate system. Thus prior to computing the stress resultants and stress couples, the stress tensor is transformed to the global cartesian coordinate system by

$$S^{IJ} = S^{ij} \frac{\partial X^I}{\partial \theta^i} \frac{\partial X^J}{\partial \theta^j} . \tag{6.2}$$

The variation along the short diagonal of the computed stress couples $\mathbf{M}^\alpha = M^{\alpha\beta}\mathbf{E}_\beta$ ($M^{33} = 0$) acting of the surface with normal $\mathbf{E}_\alpha$ are shown in Figure 6.5c for the component M^{12}, and in Figure 6.5d for the stress couple M^{21}.† The sign of the computed moments near the obtuse vertex is as predicted by the theory.‡ We note in passing that the results of mesh A in Figure 21 of Belytschko, Ong & Liu [1984] — which is a finer mesh than mesh B in the same reference — predict a reversal of the sign of M^{21} as compared with the exact solution.

It can be observed from Figure 6.5c that the computed moment M^{12} agrees well with the Morley solution for both mesh type A and mesh type B; there is no significant change in the computed values compared with those obtained from the 256-element mesh of type A. The values of M^{12} from a mesh of only 16 elements are good enough — this is for both type A and type B, even though type B yields slightly better results near the center of the plate.

On the other hand, a sharp improvement on the computed values for moment M^{21} is obtained with a mesh of type B compared with a mesh of type A. It can be seen from Figure 6.5d that the results obtained with a 16-element mesh (Figure 6.5a) of type B are clearly better than those from a 256-element mesh of type A. The values of M^{21} for a 64-element mesh of type B agree well with Morley solution. Recall that a 16-element mesh has only 4 elements per diagonal, and a 64-element mesh has only 8 elements per

† The difference in notation for the moment components should be noted: m_{11} and m_{22} are used in Morley [1963] for M^{12} and M^{21}, respectively. Further, the sign convention for the moments is also different.

‡ It appears, according to Hughes & Tezduyar [1981] who studied the same problem, that there are plate elements which do not predict correctly the sign of the moments at the obtuse corner; these authors cited Sander [1971] and Rossow [1977].

diagonal.

At the acute vertex, there is no singularity in the moments. The computed values of M^{12} and M^{21} along the long diagonal are respectively shown in Figure 6.5e and in Figure 6.5f.

The convergence of the displacement (meshes type A) at the center of the rhombic plate, normalized with respect to the Morley solution of 0.4455, is given in Figure 6.5g: The best rate of convergence is obtained with reduced integration and consistent filtering. It should be noted that this example does not have any global spurious zero-energy mode due to the simply supported boundary conditions. The enforcement of the simply supported boundary conditions, where the rotation in the direction normal to the boundary of the rhombic plate is constrained, provides an example of the treatment of rotation boundary condition discussed in Section 2.4. •

Example 6.6. Twisted beam. MacNeal & Harder [1985] proposed this example to test the effect of warp on the response of shell elements — the gaussian curvature of the shell in this example is negative. The beam has length 12, width 1.1, thickness $h = 0.32$, and is twisted 90^o from root to tip (see Figure 6.6). The material properties are $E = 29 \times 10^6$, $\nu = 0.22$. Results from a mesh of 6 shell (9-node) elements are tabulated in Table 6.6, where the referential values displacement are as given in MacNeal & Harder [1985].

Table 6.6. *Twisted beam. Displacement in direction of applied force.*

Integration Type	Applied Force	
	In-plane Shear (refer. $= 5.424e-03$)	Out-of-plane Shear (refer. $= 1.754e-03$)
$kf = 0$	$5.4177e-03$	$1.8061e-03$
$kf = 1$	$5.4110e-03$	$1.8056e-03$
$kf = 3$	$5.4110e-03$	$1.8056e-03$
Full 3×3	$5.2797e-03$	$1.7876e-03$

In this particular example, due to the shape of the elements in the mesh of Figure 6.6,

identical results are obtained with $kf = 1$ and with $kf = 3$. Further, full integration here yields good results since the shell is relatively thick. •

Example 6.7. Pinched cylinder. A cylinder of thickness $h = 3$, radius $R = 300$, half-length $L = 300$, and made of material with $E = 3 \times 10^6$ and $\nu = 0.3$, is employed to test the performance of the element in a shell structure with a single curvature. Two types of boundary conditions at the extremities of the cylinder are considered: (i) completely unrestrained, and (ii) supported by rigid diaphragms† such that the only unrestrained degrees of freedom are the displacement along the axis of the cylinder and the rotation about the tangent to the shell boundary. The under-integrated stiffness of the cylinder with free ends possesses spurious zero-energy modes, and hence the free boundary condition provides a more meaningful test of performance for the filtering scheme of these spurious modes. Also since theoretical results exist for the free-end pinched cylinder, we will vary the geometric parameters of the cylinder to test the performance of the present filtering scheme under change of geometry of the shell structure. The cylinder with end diaphragms on the other hand presents complex state of bending and membrane actions, and thus is often used to evaluate the performance of shell elements.

Only 1/8th of the cylinder is modeled as shown in Figure 6.7a. The convergence of the normalized displacement under the point force for both boundary conditions is shown in Figure 6.7b and in Figure 6.7c; the mesh sizes correspond to a uniform discretization with 1, 4, 16, and 64 elements. One can see that, for both boundary conditions, the best rate of convergence is obtained with reduced integration and consistent filtering of spurious modes. For the cylinder with free ends, a good approximation of the displacement under the point force F is given by (Lukasiewicz [1979,p.405])

$$\frac{0.0745FR^3}{2DL}, \quad \text{with} \quad D := \frac{Eh^3}{12(1-\nu^2)}. \tag{6.3}$$

† This boundary condition is also called the "freely supported" boundary condition by some authors.

Note that the above formula is based on some approximating assumptions† that are only valid for short and thin cylinder. Formula (6.3) yields the value of displacement of -4.5197×10^{-4}. This formula will later serve as a guideline to verify the computed results with different values of radius R and thickness h. For the case of rigid diaphragms, the displacement is normalized with the exact value of -1.82489×10^{-5} computed by Lindberg, Olson & Cowper [1969] based on Flugge's equations.

For an infinitely long cylinder, the displacement under the point force is given by

$$0.737\ \frac{FR}{Eh^2}\left(\frac{R}{h}\right)^{\frac{1}{2}}, \tag{6.4}$$

which also does not include shear deformation and local effects of point loading (Lukasiewicz [1979,p.371]).

The computed values of the displacement under the point force with several geometry of the cylinder with free ends are summarized in Table 6.7a, where the results are presented as follows. We start with the basic geometry with parameters $h = 3$, $R = 300$, and $L = 300$. We vary one of these parameters, and keep the other two fixed as given in the basic geometry; only the parameter which differs from its basic counterpart is shown in Table 6.7a. It could be seen from Table 6.7a that the order of magnitude of the displacement corresponds well with formula (6.3), except for the case with $L = 3000$ where one should use formula (6.4) to obtain a value of $-8.189e-05$. The result in Table 6.7a testifies to a robust performance of the proposed filtering of spurious modes under change of geometry.

Back to the pinched cylinder with diaphragms and basic geometric parameters, the radial displacement along the lines BC and DC are respectively shown in Figures 6.7d and 6.7e. The computed stress resultants and stress couples in the pinched cylinder with diaphragms agree well with the exact solution (which was derived for a theory without

† These assumptions are: (i) the generator remains straight, (ii) partial satisfaction of boundary conditions at the free edge, (iii) no shear deformation. Formula (6.3) was found to be in good agreement with experiments.

Table 6.7a. *Pinched cylinder with free ends. Displacement under point force for different geometric parameters.*

Basic parameters: $h = 3$, $R = 300$, $L = 300$		
No. elem.	$h = 0.3$	$h = 30$
1	$-4.0782e-01$	$-4.8458e-07$
4	$-4.4976e-01$	$-5.2917e-07$
16	$-4.5276e-01$	$-5.3778e-07$
No. elem.	$R = 30$	$R = 3000$
1	$-1.8005e-05$	$-4.0809e-01$
4	$-9.3667e-06$	$-4.5566e-01$
16	$-5.3312e-06$	$-4.6088e-01$
No. elem.	$L = 30$	$L = 3000$
1	$-4.3440e-03$	$-8.9260e-05$
4	$-4.8033e-03$	$-9.1821e-05$
16	$-4.8520e-03$	$-8.5949e-05$

shear deformation) as presented in Lindberg, Olson, & Cowper [1969]. Let all force components be referred to the local triads $\{\mathbf{T}_1, \mathbf{T}_2, \mathbf{T}_3\}$ as shown in Figure 6.7a: $\mathbf{N}^\alpha = N^{\alpha 1}\mathbf{T}_1$, and $\mathbf{M}^\alpha = M^{\alpha\beta}\mathbf{T}_\beta$. Figure 6.7f and Figure 6.7g show the variation of the membrane force N^{11} along the lines BC and DC, respectively. Figure 6.7h and Figure 6.7i show the variation of the membrane force N^{22} along the lines BC and DC, respectively. Finally, Figure 6.7j and Figure 6.7k show the variation of the bending moment M^{21} along the lines BC and DC, respectively.

Remark 6.3. The internal forces at these lines are computed as follows. The stress tensors at a nodal point I, with coordinates $(\theta_1^1, \theta_1^2, \theta^3)$,

$$\mathbf{S}(\theta_1^{\{\alpha\}}, \theta^3) = S^{ij}(\theta_1^{\{\alpha\}}, \theta^3)\mathbf{A}_i(\theta_1^{\{\alpha\}}, \theta^3) \otimes \mathbf{A}_j(\theta_1^{\{\alpha\}}, \theta^3)\,, \tag{6.4a}$$

are obtained by a linear extrapolation such that

$$S^{ij}(\theta_1^{\{\alpha\}}, \theta^3) = \sum_{G=1}^{4} P_G(\theta_1^{\{\alpha\}}) S^{ij}(\theta_G^{\{\alpha\}}, \theta^3)\,, \tag{6.4b}$$

where $(\theta_G^{\{\alpha\}})$ denotes the coordinates of the integration points, and $\mathbf{A}_i(\theta_1^{\{\alpha\}}, \theta^3)$ is as given in (3.8). The stress resultants and stress couples at the nodal point I are computed after equation (3.18). These values are then averaged at nodes which are common to two

adjacent elements — the difference of these values at a common nodal point is very small. □

We also used the cylinder with free ends to test the robustness of both the element and the filtering scheme ($kf = 1$) under the type of mesh distorsion shown in Figure 6.7l. We employ here a mesh with 4 elements, which when undistorted already gives good results. The triad at the node in the middle of the mesh is rotated about the director, and the degree of distortion is represented by the angle of this rotation with respect to the undistorted mesh — Figure 6.7l corresponds to an angle of 30°. In fact, the distortion of the mesh in Figure 6.7l is more severe than in the type of distorted mesh considered by Park & Stanley [1986]; further, a smaller number of elements is used here. The displacement under the point force for various degrees of distortion is tabulated in Table 6.7b. Also shown in Table 6.7b are the values normalized with respect to the displacement of the undistorted mesh; the results are plotted in Figure 6.7m. •

Table 6.7b. *Pinched cylinder with free ends. Displacement for a 4-element distorted mesh.*

Angle (deg.)	Displacement	Norm. Disp.
−30	−3.8176e−04	0.838
−20	−4.4811e−04	0.983
−10	−4.6259e−04	1.015
0	−4.5577e−04	1.000
10	−4.4440e−04	0.975
20	−4.2543e−04	0.933
30	−3.7593e−04	0.898

Example 6.8. Scordelis-Lo roof [1961]. This is the second membrane locking test to the 9-node element, other than the above example of a pinched cylinder. The geometric parameters of the roof and material properties are as in MacNeal & Harder [1985]: length 50, radius 25, thickness 0.25, $E = 4.32\times 10^8$, $\nu = 0$. We use the same value of 0.3024 as in the latter reference to normalize the vertical displacement at mid-span of the free edge. A quarter of the roof is modeled. The results are tabulated in Table 6.8 and presented in Figure 6.8. •

Table 6.8. *Scordelis-Lo roof. Normalized vertical displacement at mid-span of free edge.*

Referential Displacement = 0.3024				
No. of elements	2×2 Integration + Filtering			3×3 Integration
	$kf = 0$	$kf = 1$	$kf = 3$	
1	1.2336	1.2472	1.2035	0.0940
4	1.0339	1.0339	1.0312	0.2650
16	1.0028	1.0027	1.0025	0.8132
64	0.9985	0.9985	0.9984	0.9807

Example 6.9. Hemispherical shell under point loads. The hemispherical shell in Figure 6.9a (shown with a mesh with 48 elements over a 1/4 of the shell) has a uniform thickness of $h = 0.04$, radius $R = 10$, and material properties $E = 6.825 \times 10^7$, $\nu = 0.3$. All degrees of freedom at the pole are constrained, while those along the equator are free. This example was proposed by MacNeal & Harder [1985] as a test of shell element with double curvature (the Gaussian curvature is here positive), and is used in particular to verify the ability of shell elements to model rigid body motion (Belytschko *et al* [1985b]). The convergence of the displacement under the applied force is reported in Table 6.9a.

Table 6.9a. *Hemispherical shell. Displacement under point force.*

No. of elements	2×2 Integration + Filtering			3×3 Integration
	$kf = 0$	$kf = 1$	$kf = 3$	
3	$-1.0626e-01$	$-1.0269e-01$	$-9.1300e-02$	$-8.9825e-05$
12	$-9.1357e-02$	$-9.0991e-02$	$-8.8650e-02$	$-1.1582e-03$
48	$-9.1123e-02$	$-9.0806e-02$	$-8.9583e-02$	$-1.0573e-02$

The theoretical lower bound to this problem was reported to be 0.0924 as obtained by Morley & Morris [1978]; the results of our numerical computation show that the displacement converges to a value below 0.0924 for both cases where filtering is not used ($kf = 0$) and where it is used ($kf = 1$), as can be seen from Table 6.9a. However, since we do not have access to this reference, we could not comment on the results. We speculate that this theoretical lower bound was computed using a theory without shear

deformation. It should be noted here that due to the boundary conditions, there is no global spurious zero-energy mode. Figure 6.9b shows the convergence of the (normalized) displacement under the applied force. The element sizes correspond to the meshes with 3, 12, and 48 elements, respectively.

The displacements under the two applied forces must be exactly equal in absolute value. Using the mesh with 3 elements together with reduced integration and filtering of spurious zero-energy modes, the results in Table 6.9b are obtained for the different types of local triads discussed in Section **2.2**.

Table 6.9b. *Hemispherical shell. Displacements under point forces as obtained with several types of local triad.*

Local Triads	Disp. 1	Disp. 2
Hughes & Liu	$-1.0170e-01$	$1.0213e-01$
Huang & Hinton	$-1.0245e-01$	$1.0236e-01$
Present	$-1.026857e-01$	$1.026857e-01$

The asymmetry in the displacements when using the local triads proposed by Hughes & Liu [1981] and by Huang & Hinton [1986] is due to the discontinuity of these local triads as discussed earlier in Remark 2.1.

Remark 6.3. In Belytschko *et al* [1985b], these authors reported a "confusing result" concerning the convergence rate of the inconsistent filtering scheme ($\bar{\mathbf{b}} = \mathbf{z}$). They observed — from the results obtained for the hemispherical sphere — that the rate of convergence of the inconsistent filtering ($kf = 3$) is higher than that of the consistent one ($kf = 1$). It is important to note that generalization of the last statement is not warranted, for we have presented examples where the contrary is true. From Figure 6.9b and Figure 6.4b (for the square plate with corner point-supports), one can observe that the displacement with $kf = 3$ is closer to the converged solution than the displacement with $kf = 2$ in a certain range of mesh size. However, the difference in the rates of convergence here is marginal; it is by contrast significant in the case of the pinched cylinder with free ends as shown in Figure 6.7b, where the rate of convergence of the

inconsistent filtering is much slower than that of the consistent one (see also the specially distorted patch test, Table 6.1b, and the rhombic plate, Figure 6.5g). □ •

7. Closure

We have presented a class of simple and efficient degenerated shell elements. The formulation is based on the use of convected coordinates as in shell theory. For thin shell structures, we employ uniformly reduced integration to relieve shear and membrane locking. A reliable and efficient method of filtering spurious zero-energy modes, which appear as a consequence of reduced integration, is proposed. The present formulation has been implemented with a 9-node Lagrangian interpolation. The two features mentioned above — uniform reduced integration and filtering of spurious modes — considerably decrease the cost of computing the stiffness matrix. Further, no local-global transformation of the stiffness is necessary. The present 9-node shell element passes the required higher-order patch tests, and is subjected to an extensive course of obstacles recommended by several authors. Accurate results are obtained in all of these test problems.

Acknowledgements

The encouragement from Profs. J.C. Simo and R.L. Taylor, and their discussions, are here gratefully acknowledged. The first author also thanks the support of his colleagues: Prof. M.A. Austin, Dr. J.E. Higgins, and Dr. T.L. Wuu.

References

Ahmad, S., Irons, B.M., and Zienkiewicz, O.C. [1970], "Analysis of thick and thin shell structures by curved finite elements," *Int. J. Num. Meth. Engng.*, Vol. 2 , pp. 419-451.

Babuska, I. [1987], "Are high degree elements preferrable? Some aspects of the h and h-p version of the finite element method," Proc. of the Int. Conf. on *Numerical Methods in Engineering: Theory and Applications* (NUMETA 87), Swansea, July.

Barsoum, R.S. [1976], "On the use of isoparametric finite elements in linear fracture mechanics," *Int. J. Num. Meth. Engng.*, Vol. 10, pp. 25-38.

Belytschko, T., Liu, W.K., Ong, J.S.J., and Lam, D. [1985a], "Implementation and application of a 9-node Lagrange shell element with spurious mode control," *Computers & Structures*, Vol. 20, pp. 121-128.

Belytschko, T., Ong, J.S.J., and Liu, W.K. [1984], "A consistent control of spurious singular modes in the 9-node Lagrange element for the Laplace and Mindlin plate equations," *Comp. Meth. Appl. Mech. Engng.*, Vol. 44, pp. 269-295.

Belytschko, T., Stolarski, H., Liu, W.K., Carpenter, N., and Ong, J. [1985b], "Stress projection for membrane and shear locking in shell finite elements," *Comp. Meth. Appl. Mech. Engng.*, Vol. 51, pp. 221-258.

Belytschko, T., and Tsay, C.S. [1983], "A stabilization procedure for the quadrilateral plate with one-point quadrature," *Int. J. Num. Meth. Engng.*, Vol. 19, pp. 405-420.

Forsberg, K.J., and Fong, H.H. [1985] (Chairmen), *Finite Element Standard Forum, Book 1*, AIAA/ASME/ASCE/AHS 26th Structures, Structural Dynamics, and Materials Conference, Orlando, Florida.

Green, A.E., and Zerna, W. [1968], *Theoretical Elasticity* , Second Edition, Clarendon Press, Oxford.

Golub, G.H., and Van Loan, C.F. [1983], *Matrix Computations* , The John Hopkins University Press, Baltimore.

Henshell, R.D., and Shaw, K.G. [1975], "Crack tip elements are unnecessary," *Int. J. Num. Meth. Engng.*, Vol. 9, pp. 495-509.

Hughes, T.J.R., and Liu, W.K. [1981], "Nonlinear Finite Element Analysis of Shells: Part I. Three-Dimensional Shells," *Comp. Meth. in Appl. Mech. and Engng.*, Vol. 26, pp. 331-362.

Hughes, T.J.R., and Tezduyar, T.E. [1981], "Finite elements based upon Mindlin plate theory with particular reference to the four-node bilinear isoparametric element," *J. Appl. Mech.*, Vol. 48, pp. 587-596.

Huang, H.C., and Hinton, E. [1986], "New nine node degenerated shell element with enhanced membrane and shear interpolation," *Int. J. Num. Meth. Engng.*, Vol. 22, pp. 73-92.

Jang, J., and Pinsky, P.M. [1987], "An assumed covariant strain based 9-node shell element," preprint, to appear in *Int. J. Num. Meth. Engng.*.

Kosloff, D., and Frazier, G. [1978], "Treatment of hourglass patterns in low order finite element codes," *Num. and Anal. Meth. in Geomech.*, Vol. 2, pp 52-72.

Lindberg, G.M., Olson, M.D., and Cowper, G.R. [1969], "New development in the finite element analysis of shells," *Quat. Bul. Div. Mech. Engng and Nat. Aero. Estab.*, National Research Council of Canada, Division of Mechanical Engineering, Vol. 4, pp. 1-38.

Lukasiewicz, S. [1979], *Local Loads in Plates and Shells*, Sijthoff & Noordhoff, The Netherlands.

MacNeal, R.H. [1978], "A simple quadrilateral shell element," *Computers & Structures*, Vol. 8, pp. 175-183.

MacNeal, R.H. [1982], "Derivation of element stiffness matrices by assumed strain distributions," *Nuclear Engng. & Design*, Vol. 70, pp. 3-12.

MacNeal, R.H., and Harder, R.L. [1985], "A proposed standard set of problems to test finite element accuracy," *J. of Finite Elements in Analysis and Design*, Vol. 1, pp. 3-20.

Marsden, J.E., and Hughes, T.J.R. [1983], *Mathematical Foundations of Elasticity*, Prentice-Hall, New Jersey.

Morley, L.S.D. [1963], *Skew Plates and Structures*, Int. Series of Monographs in Aeronautics and Astronautics, The MacMillan Company, New York.

Morley, L.S.D., and Morris, A.J. [1978], *Conflict between Finite Elements and Shell Theory*, Royal Aircraft Establishment Report, London.

Naghdi, P.M. [1972], "The theory of plates and shells," in *Handbuch der Physik*, Vol. vi a-2, pp. 425-640., Springer-Verlag, Berlin.

Parisch, H. [1979], "A critical survey of the 9-node degenerated shell element with special emphasis on thin shell applications and reduced integration," *Comp. Meth. Appl. Mech. Engng.*, Vol. 20, pp 323-350.

Park, K.C., and Stanley, G.M. [1986], "A curved C^o shell element based on assumed natural coordinate strains," *J. Appl. Mech.*, Vol. 53, pp. 278-290.

Pawsey, S.F., and Clough, R.W. [1971], "Improved numerical integration for thick slab finite elements," *Int. J. Num. Meth. Engng.*, Vol. 3, pp. 575-586.

Pian, T.H.H., and Sumihara, K. [1984], "Hybrid semiloof elements for plates and shells based upon a modified Hu-Washizu principle," *Computers & Structures*, Vol. 19, No. 1-2, pp. 163-173.

Pinsky, P.M., and Jang, J. [1987], "A C^o elastoplastic shell element based on assumed covariant strain interpolation," Proc. of the Int. Conf. on *Numerical Methods in Engineering: Theory and Applications* (NUMETA 87), Swansea, July.

Rossow, M. [1977], "Efficient C^o finite element solution of simply supported plates of polygonal shape," *J. Appl. Mech.*, Vol. 44, pp.347-349.

Sander, G. [1971], "Application of the dual analysis principle," *Proceedings of the IUTAM Symposium*, Liege, Belgium, pp. 167-207.

Simo, J.C., and Hughes, T.J.R. [1986], "On the variational foundations of assumed strain methods," *J. Appl. Mech.*, Vol. 53, pp. 51-54.

Simo, J.C., and Vu-Quoc, L. [1986], "Three-dimensional finite-strain rod model. Part II: Computational aspects," *Comp. Meth. Appl. Mech. Engng.*, Vol. 58, pp. 79-116.

Simo, J.C., and Vu-Quoc, L. [1987], "On the dynamics of finite strain rods undergoing large motions — The three dimensional case," to appear in *Comp. Meth. Appl. Mech. Engng.*.

Scordelis, A.C., and Lo, K.S. [1961], "Computer analysis of cylindrical shell," *J. Amer. Concr. Inst.*, Vol. 61, pp. 539-561.

Stolarski, H., and Belytschko, T. [1982], "Membrane locking and reduced integration for curved elements," *J. Appl. Mech.*, Vol. 49, pp. 172-176.

Taylor, R.L. [1979], "Finite element for general shell analysis," *5th Int. Seminar on Comp. Aspects of the FEM*, Berlin.

Taylor, R.L., Simo, J.C., Zienkiewicz, O.C., and Chan, A.C.H. [1986], "The patch test — A condition for assessing FEM convergence," *Int. J. Num. Meth. Engng.*, Vol. 22, pp. 39-62.

Timoshenko, S.P., and Woinowsky-Krieger, S. [1959], *Theory of Plates and Shells*, second edition, MacGraw-Hill, New York.

Vu-Quoc, L. [1986], *Dynamics of Flexible Structures Performing Large Overall Motions: A Geometrically-Nonlinear Approach*, Ph.D. Dissertation, Electronics Research Laboratory, Memo No. UCB/ERL M86/36, University of California, Berkeley.

Wachspress, E.L. [1981], "High-order curved finite elements," *Int. J. Num. Meth. Engng.*, Vol. 17, pp. 735-745.

Zienkiewicz, O.C., Taylor, R.L., and Too, J.M. [1971], "Reduced integration techniques in general analysis of plates and shells," *Int. J. Num. Meth. Engng.*, Vol. 3, pp. 275-290.

Zienkiewicz, O.C. [1978], *The Finite Element Method*, third edition, McGraw-Hill, London.

Appendix I. Computation of local triads.

To simplify the discussion, we choose, as an example, the global base vector $\mathbf{E}_3$ to rotate to the director $\mathbf{D} = D^I\mathbf{E}_I$. It should be recalled that any other choice would be perfectly valid, and the naming of the local base vectors $\mathbf{T}_1$ and $\mathbf{T}_2$ is simply a permutation.

- Compute rotation angle θ and rotation axis $\mathbf{h} = h^I\mathbf{E}_I$:

$$\theta = \cos^{-1}(D^3) , \quad \mathbf{h} = \frac{\mathbf{E}_3 \times \mathbf{D}}{\|\mathbf{E}_3 \times \mathbf{D}\|} . \tag{I.1}$$

- Compute the associated quaternion parameters:

$$q_o = \cos\frac{\theta}{2} , \quad q_I = h^I \sin\frac{\theta}{2} , \quad \text{for I= 1,2,3} . \tag{I.2}$$

- Compute $\mathbf{T}_1$ and $\mathbf{T}_2$ as the rotated vectors $\mathbf{E}_1$ and $\mathbf{E}_2$:

$$\mathbf{T}_1 = (q_o^2 + q_1^2 - \tfrac{1}{2})\mathbf{E}_1 + (q_2q_1 + q_3q_o)\mathbf{E}_2 + (q_3q_1 - q_2q_o)\mathbf{E}_3 , \tag{I.3}$$

$$\mathbf{T}_2 = (q_1q_2 - q_3q_o)\mathbf{E}_1 + (q_o^2 + q_2^2 - \tfrac{1}{2})\mathbf{E}_2 + (q_3q_2 + q_1q_o)\mathbf{E}_3 . \tag{I.4}$$

Remark. Note that the orthogonal matrix associated with the rotation vector $(\theta\mathbf{h})$ is

$$\exp[\theta\overset{\vee}{\mathbf{h}}] = 2\begin{bmatrix} q_o^2 + q_1^2 - \frac{1}{2} & q_1q_2 - q_3q_o & q_1q_3 + q_2q_o \\ q_2q_1 + q_3q_o & q_o^2 + q_2^2 - \frac{1}{2} & q_2q_3 - q_1q_o \\ q_3q_1 - q_2q_o & q_3q_2 + q_1q_o & q_o^2 + q_3^2 - \frac{1}{2} \end{bmatrix} , \tag{I.5}$$

where the components of $\mathbf{T}_1$ and $\mathbf{T}_2$ are contained the first two columns, and the components of $\mathbf{D}$ in the third column. We refer to Simo & Vu-Quoc [1986,87] and Vu-Quoc [1986] for further details concerning the use of quaternion parameters in the study of large motions of rods. □

Appendix II. Computation of $\bar{\mathbf{b}}$.

In this appendix, we discuss some practical aspects in implementing the computation of the vector $\bar{\mathbf{b}}$ defined in (5.18), in particular, the procedure in the proof of Proposition 5.6. As mentioned in Remark 5.7, all vectors $\{\mathbf{z}, \mathbf{w}_1, \ldots, \mathbf{w}_m\}$ are normalized using the norm $\|\cdot\|_2$, which leads to the matrix $\mathbf{H} = [H_{ij}]$ in (5.22) with $H_{(ii)} = 1$ and $|H_{ij}| < 1$. It is more convenient to reorder the unknowns to have

$$\mathbf{H}\begin{Bmatrix} \alpha_1 \\ \cdot \\ \alpha_m \\ \alpha_o \end{Bmatrix} = \begin{Bmatrix} 0 \\ \cdot \\ 0 \\ c \end{Bmatrix}, \text{ with } \mathbf{H} = \begin{bmatrix} (\mathbf{w}_1 \bullet \mathbf{w}_1) & \cdot & (\mathbf{w}_1 \bullet \mathbf{w}_m) & (\mathbf{w}_1 \bullet \mathbf{z}) \\ \cdot & \cdot & \cdot & \cdot \\ (\mathbf{w}_m \bullet \mathbf{w}_1) & \cdot & (\mathbf{w}_m \bullet \mathbf{w}_m) & (\mathbf{w}_m \bullet \mathbf{z}) \\ (\mathbf{z} \bullet \mathbf{w}_1) & \cdot & (\mathbf{z} \bullet \mathbf{w}_m) & (\mathbf{z} \bullet \mathbf{z}) \end{bmatrix} \in \mathbf{R}^{(m+1)\times(m+1)}. \quad \text{(II.1)}$$

We then proceed to **LU**-decompose the matrix **H** with a partial pivoting (e.g., Golub & Van Loan [1983]): Suppose that we have eliminated equations 1 to $(i-1)$, and that equation i is to be eliminated next. We begin a search in column i for the coefficient with maximal absolute value under (and including) the diagonal term $H_{(ii)}$. An interchange of the rows will follow such that the diagonal term has the maximal absolute value in the column. If the maximal coefficient is zero (or smaller than certain tolerance), this means that row i is linearly dependent on the previous rows. In this case, skip the elimination of equation i. The procedure is continued until we complete the **LU**-decomposition of **H**.

If $U_{m+1,m+1} \neq 0$, then problem (5.19) is solvable. All vectors $\mathbf{w}_i$'s corresponding to zero diagonal terms in **U**, i.e., $U_{(ii)} = 0$ (or $|U_{(ii)}| < \textit{Tolerance}$), are dropped from (5.21), since they are linearly dependent on the remaining vectors $\mathbf{w}_i$'s (see Proposition 5.6). This is done by simply deleting the rows and columns in the matrix **LU** which correspond to the eliminated vectors $\mathbf{w}_i$'s. In this manner, we thus avoid to do the decomposition again.

If $U_{m+1,m+1} = 0$, problem (5.19) is unsolvable for the current geometry. In this case, we use the filtering scheme that does not maintain consistency of the element, and

set $\overline{\mathbf{b}} = \mathbf{z}$. □

Figure Captions

Figure 2.2a. Proposed method of generating continous field of local triads.

Figure 2.2b. Field of local triads after Hughes & Liu [1981].

Figure 2.2c. Field of local triads after Huang & Hinton [1986].

Figure 2.3. Constrained rotation on the shell boundary.

Figure 6.1a. Patch tests. Square plate (length 10).

Figure 6.1b. Patch tests. Square plate (length 4) with specially distorted mesh.

Figure 6.1c. Patch tests. Square plate (length 4) with specially distorted mesh. Pure bending. Perspective view of undeformed and deformed configurations.

Figure 6.2a. Thick circular plate. 3-element mesh.

Figure 6.2b. Thick circular plate. Transverse displacement ($\times 10^6$) along radius. ○: 3 elements. Solid line: exact.

Figure 6.4a. Square plate with corner supports. Transverse displacement along center line. ○: 16 elements. □ : 64 elements.

Figure 6.4b. Square plate with corner supports. Displacement at center. (The numbers on the curves are the values of kf with which results are computed. F: Full integration.)

Figure 6.5a. Rhombic plate. Geometry.

Figure 6.5b. Rhombic plate. Treatment of singularity: Nodes at quarter points from an obtuse vertex.

Figure 6.5c. Rhombic plate. Variation of moment M^{12} along the short diagonal. ○: 16 elements. △: 64 elements. Solid line: Morley solution.

Figure 6.5d. Rhombic plate. Variation of moment M^{21} along the short diagonal. ○: 16 elements, type A. ●: 16 elements, type B. △: 64 elements, type A. ▲: 64 elements, type B. Solid line: Morley solution. Dotted line: 256 elements, type A.

Figure 6.5e. Rhombic plate. Variation of moment M^{12} along the long diagonal. ○: 16 elements. △: 64 elements.

Figure 6.5f. Rhombic plate. Variation of moment M^{21} along the long diagonal. ○: 16 elements. △: 64 elements.

Figure 6.5g. Rhombic plate. Convergence of tranverse displacement at center. (The numbers on the curves are the values of kf with which results are computed. F: Full integration.)

Figure 6.6. Twisted beam. Perspective view (shown with out-of-plane shear force).

Figure 6.7a. 1/8th of the pinched cylinder. Perspective view.

Figure 6.7b. Pinched cylinder with free ends. Convergence of displacement under point force. (The numbers on the curves are the values of kf with which results are computed. F: Full integration.)

Figure 6.7c. Pinched cylinder with diaphragms. Convergence of displacement under point force. (The numbers on the curves are the values of kf with which results are computed. F: Full integration.)

Figure 6.7d. Pinched cylinder with diaphragms. Radial displacement ($\times 10^6$) along BC. ○: 16-element mesh. △: 64-element mesh. Solid line: Flugge's equations.

Figure 6.7e. Pinched cylinder with diaphragms. Radial displacement ($\times 10^6$) along DC. ○: 16-element mesh. △: 64-element mesh. Solid line: Flugge's equations.

Figure 6.7f. Pinched cylinder with diaphragms. Membrane force N^{11} ($\times 100$) along line BC. ○: 16-element mesh. △: 64-element mesh. Solid line: Flugge's equations.

Figure 6.7g. Pinched cylinder with diaphragms. Membrane force N^{11} ($\times 100$) along line DC. ○: 16-element mesh. △: 64-element mesh. Solid line: Flugge's equations.

Figure 6.7h. Pinched cylinder with diaphragms. Membrane force N^{22} ($\times 100$) along line BC. ○: 16-element mesh. △: 64-element mesh. Solid line: Flugge's equations.

Figure 6.7i. Pinched cylinder with diaphragms. Membrane force N^{22} ($\times 100$) along line DC. ○: 16-element mesh. △: 64-element mesh. Solid line: Flugge's equations.

Figure 6.7j. Pinched cylinder with diaphragms. Moment M^{21} ($\times 10$) along line BC. ○: 16-element mesh. △: 64-element mesh. Solid line: Flugge's equations.

Figure 6.7k. Pinched cylinder with diaphragms. Moment M^{21} ($\times 10$) along line DC. ○: 16-element mesh. △: 64-element mesh. Solid line: Flugge's equations.

Figure 6.7l. Pinched cylinder with free ends. 4-element mesh shown with 30^o angle of distortion. Lines connecting mid-side nodes to interior nodes are plotted to show distortion of mesh.

Figure 6.7m. Pinched cylinder with free ends. Distorted 4-element mesh. Displacement normalized with the one from undistorted mesh.

Figure 6.8. Scordelis-Lo roof. Convergence of vertical displacement at mid-span of free edge. (The numbers on the curves are the values of kf with which results are computed. F: Full integration.)

Figure 6.9a. Hemispherical shell. Perspective view (48-element mesh).

Figure 6.9b. Hemispherical shell. Convergence of displacement under point force. (The numbers on the curves are the values of kf with which results are computed. F: Full integration.)

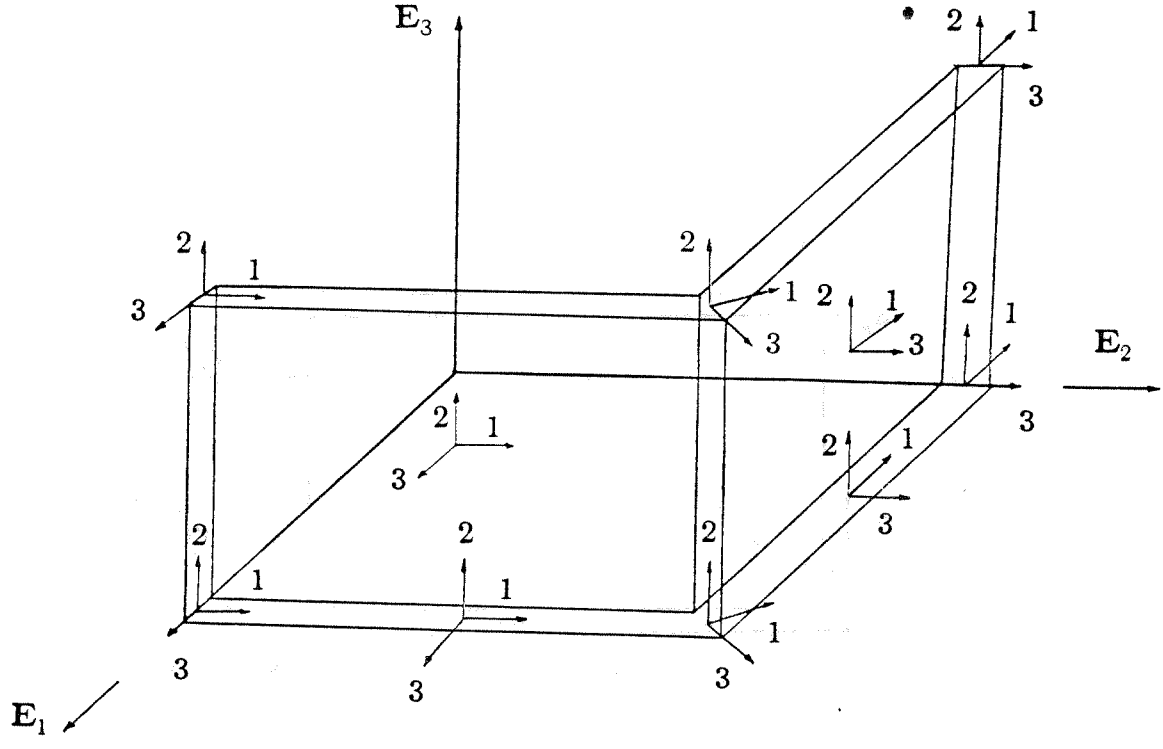

Figure 2.2a. Proposed method of generating continous field of local triads.

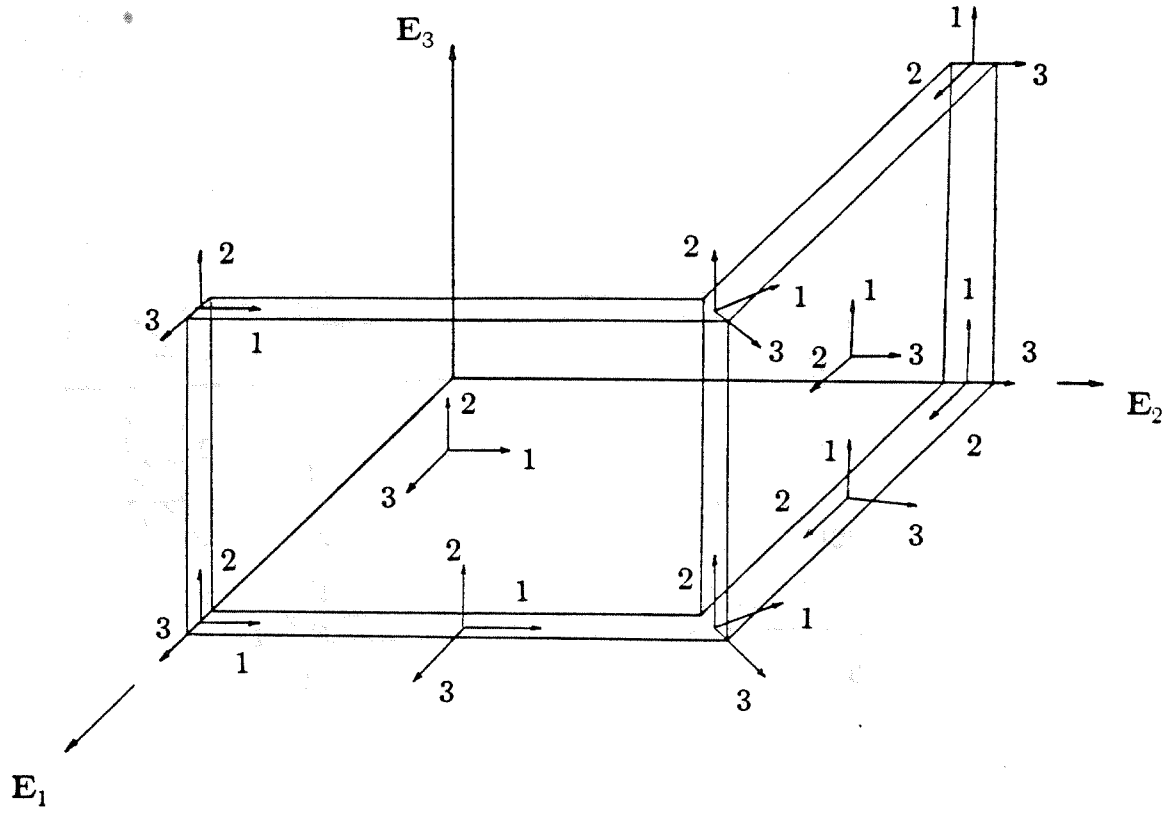

Figure 2.2b. Field of local triads after Hughes & Liu [1981].

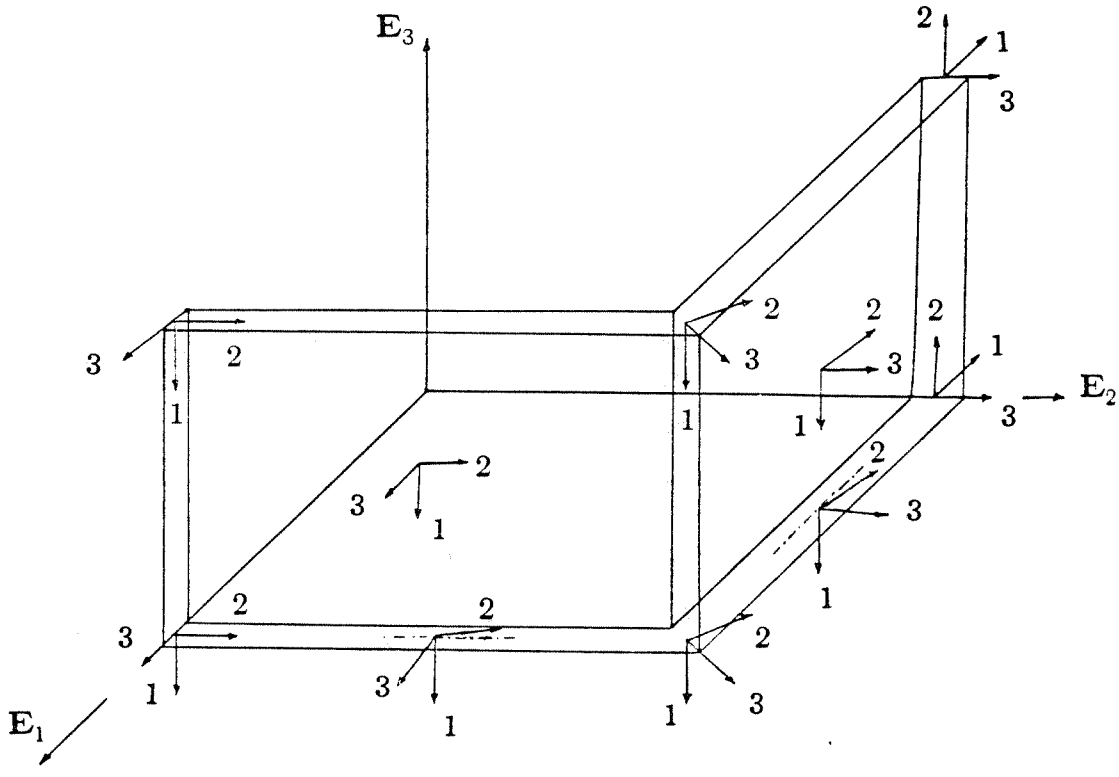

Figure 2.2c. Field of local triads after Huang & Hinton [1986].

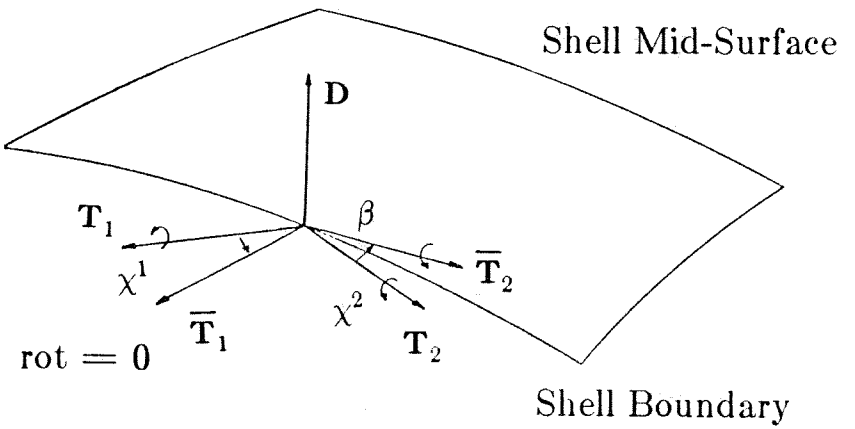

Figure 2.3. Constrained rotation on the shell boundary.

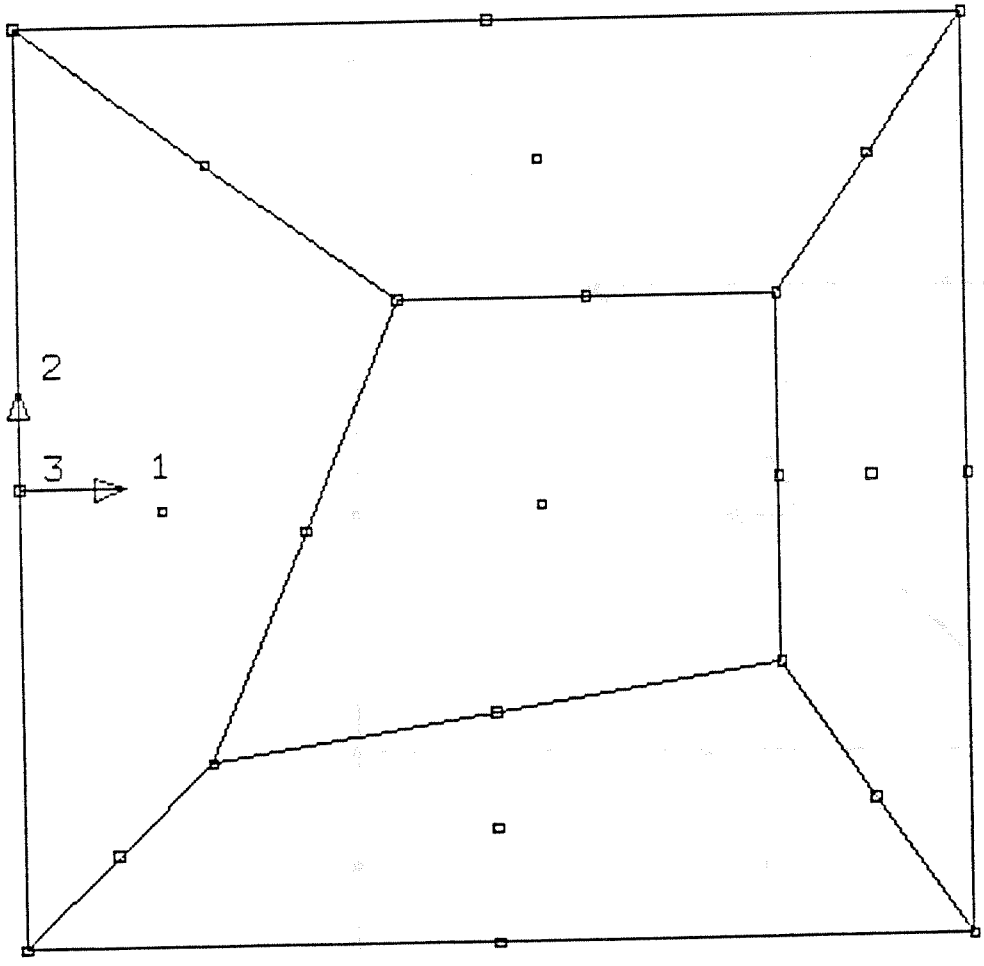

FEAP

Figure 6.1a. Patch tests. Square plate (length 10).

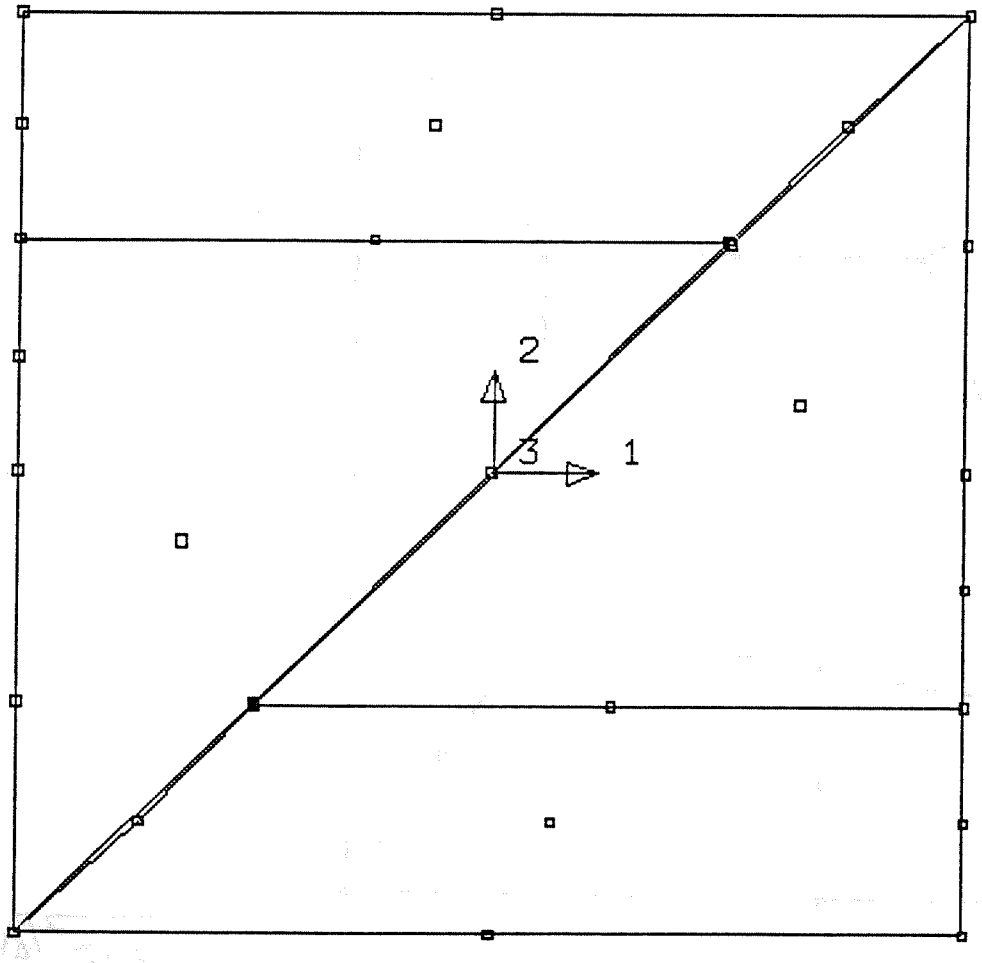

FEAP

Figure 6.1b. Patch tests. Square plate (length 4) with specially distorted mesh.

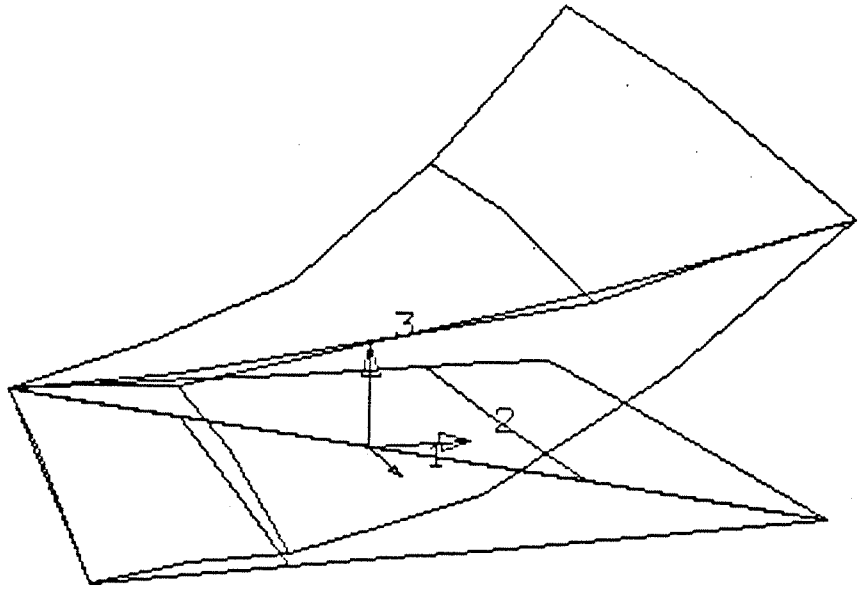

Figure 6.1c. Patch tests. Square plate (length 4) with specially distorted mesh. Pure bending. Perspective view of undeformed and deformed configurations.

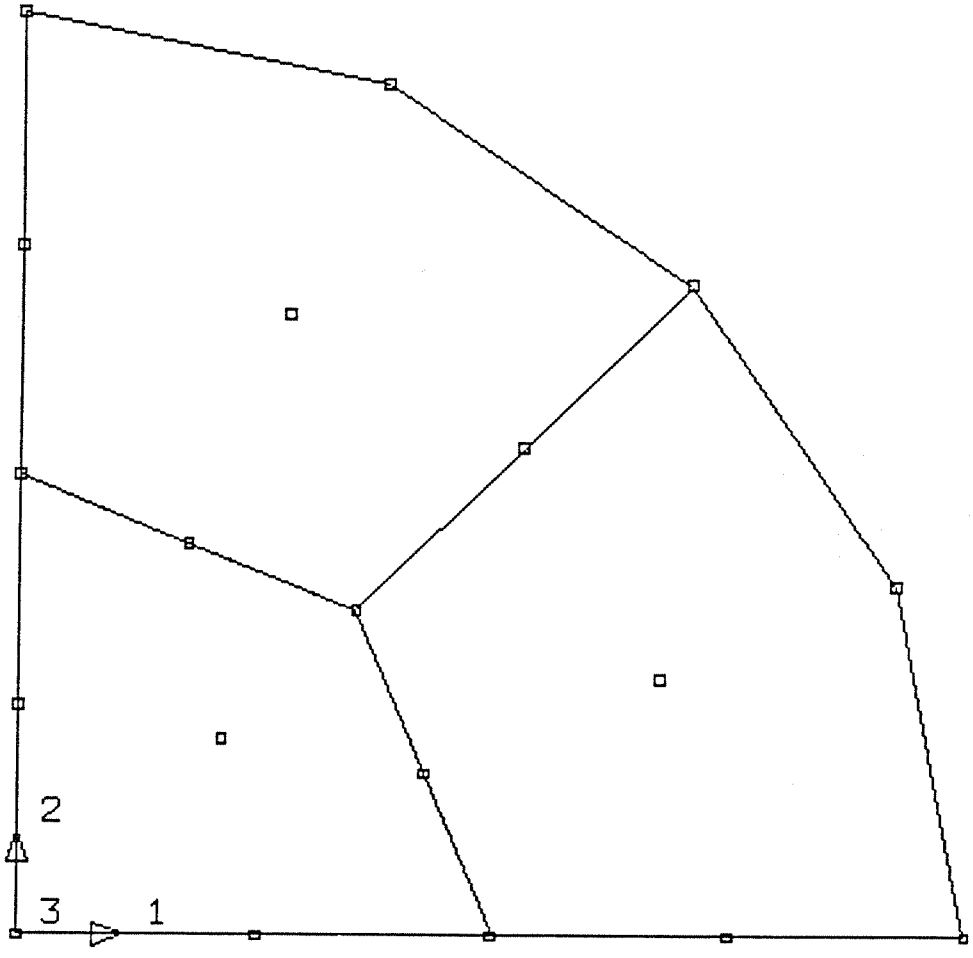

FEAP

Figure 6.2a. Thick circular plate. 3-element mesh.

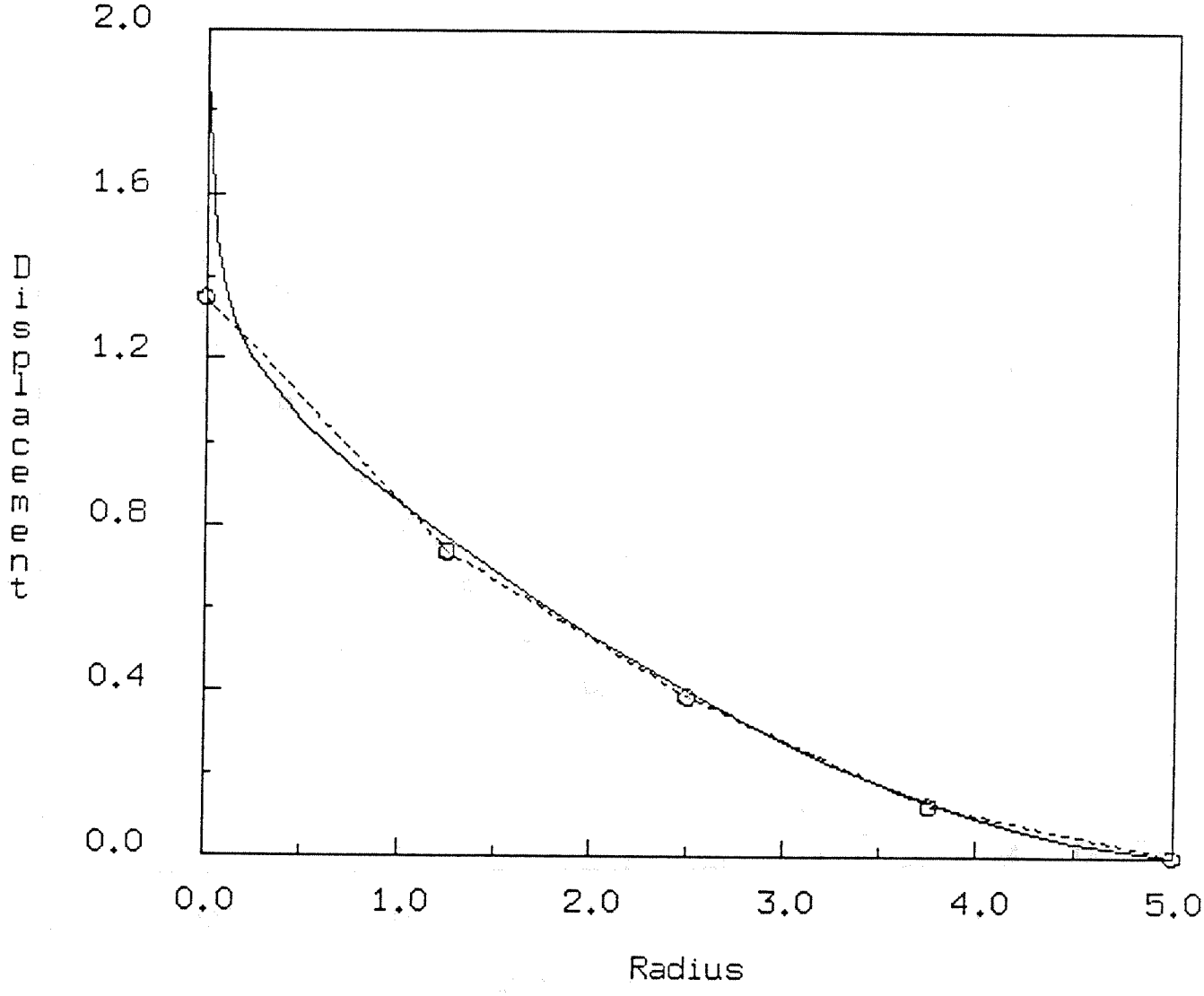

Figure 6.2b. Thick circular plate. Transverse displacement along radius. ○: 3 elements. Solid line: exact.

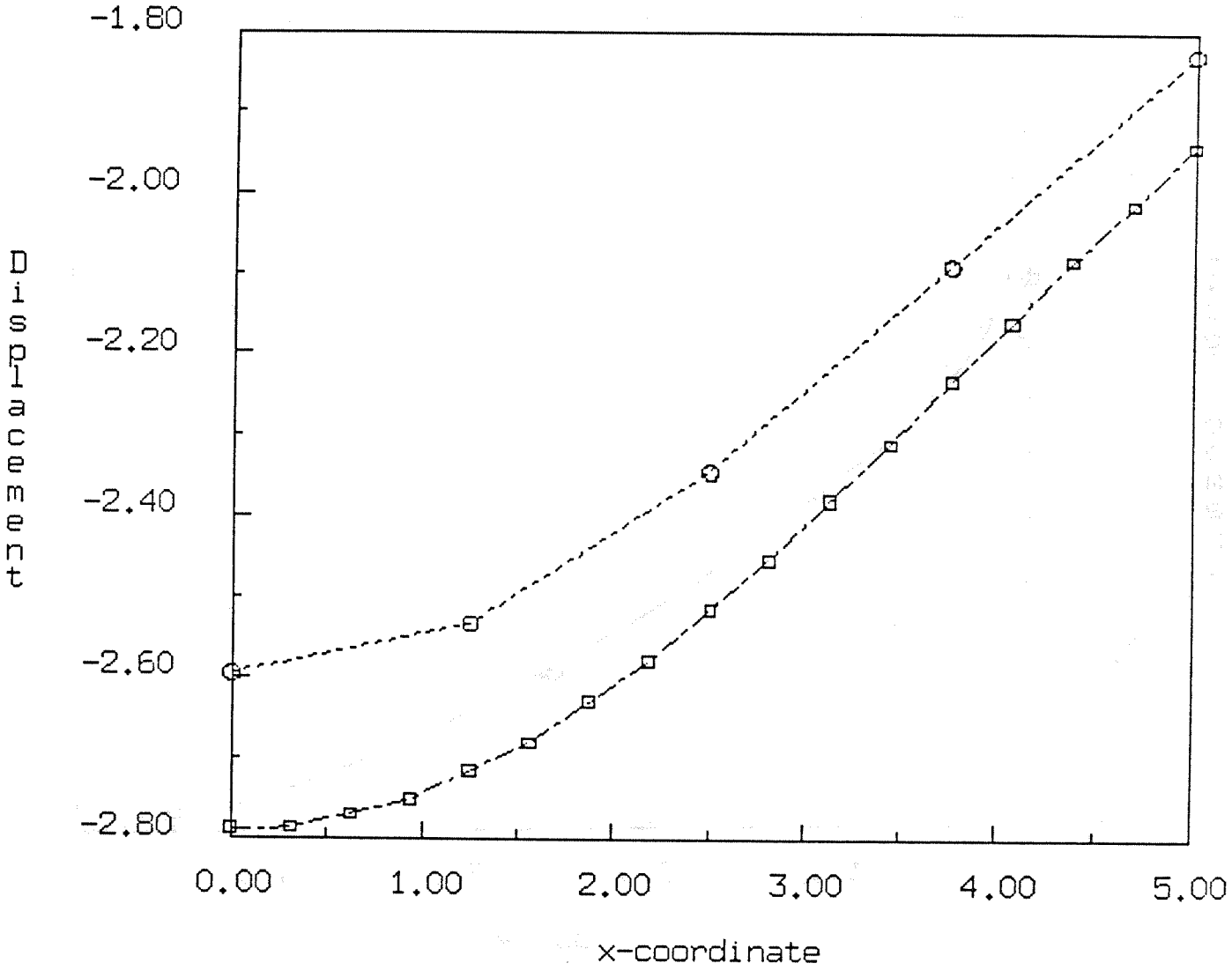

Figure 6.4a. Square plate with corner supports. Transverse displacement along center line. ○: 16 elements. □ : 64 elements.

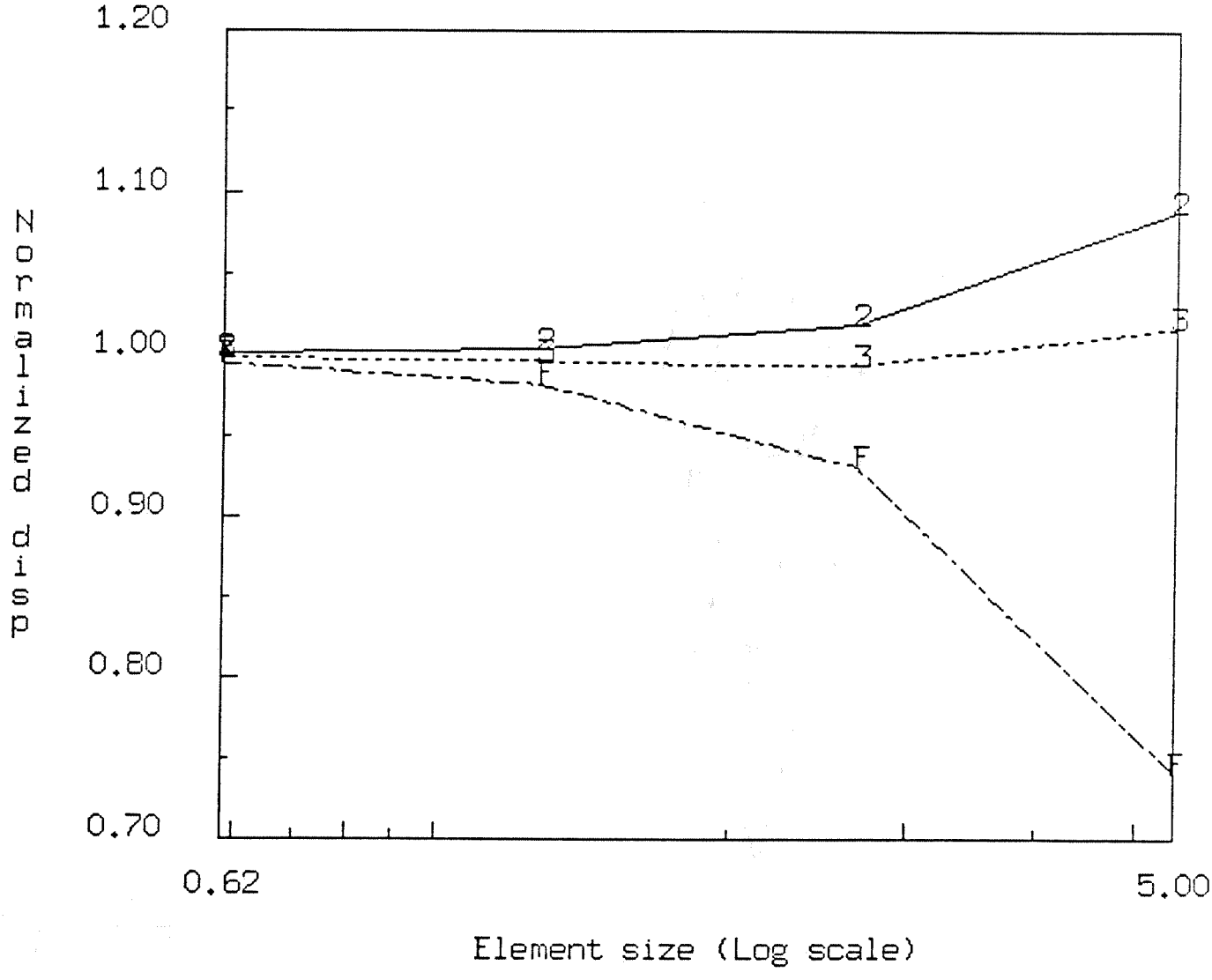

Figure 6.4b. Square plate with corner supports. Displacement at center. (The numbers on the curves are the values of kf with which results are computed. F: Full integration.)

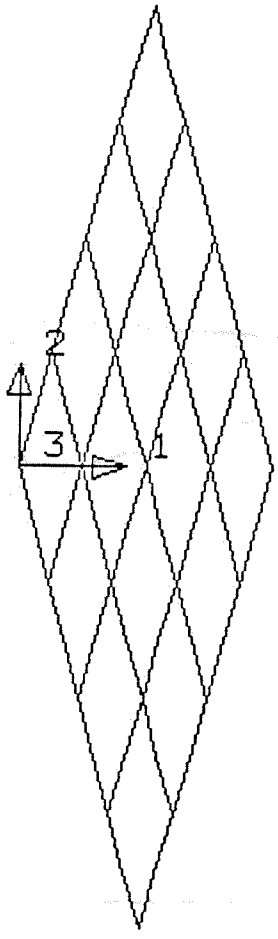

FEAP

Figure 6.5a. Rhombic plate. Geometry.

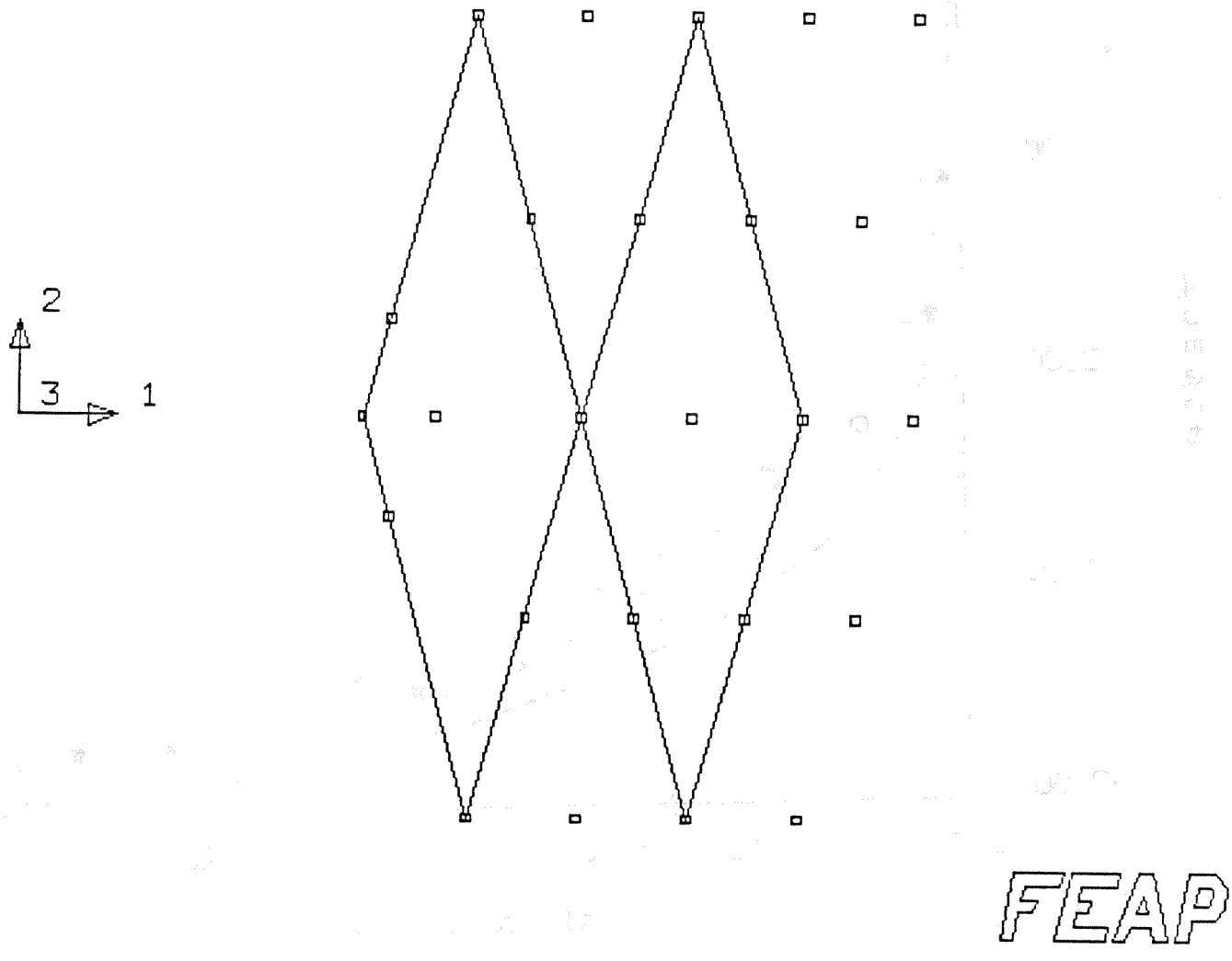

Figure 6.5b. Rhombic plate. Treatment of singularity: Nodes at quarter points from an obtuse vertex.

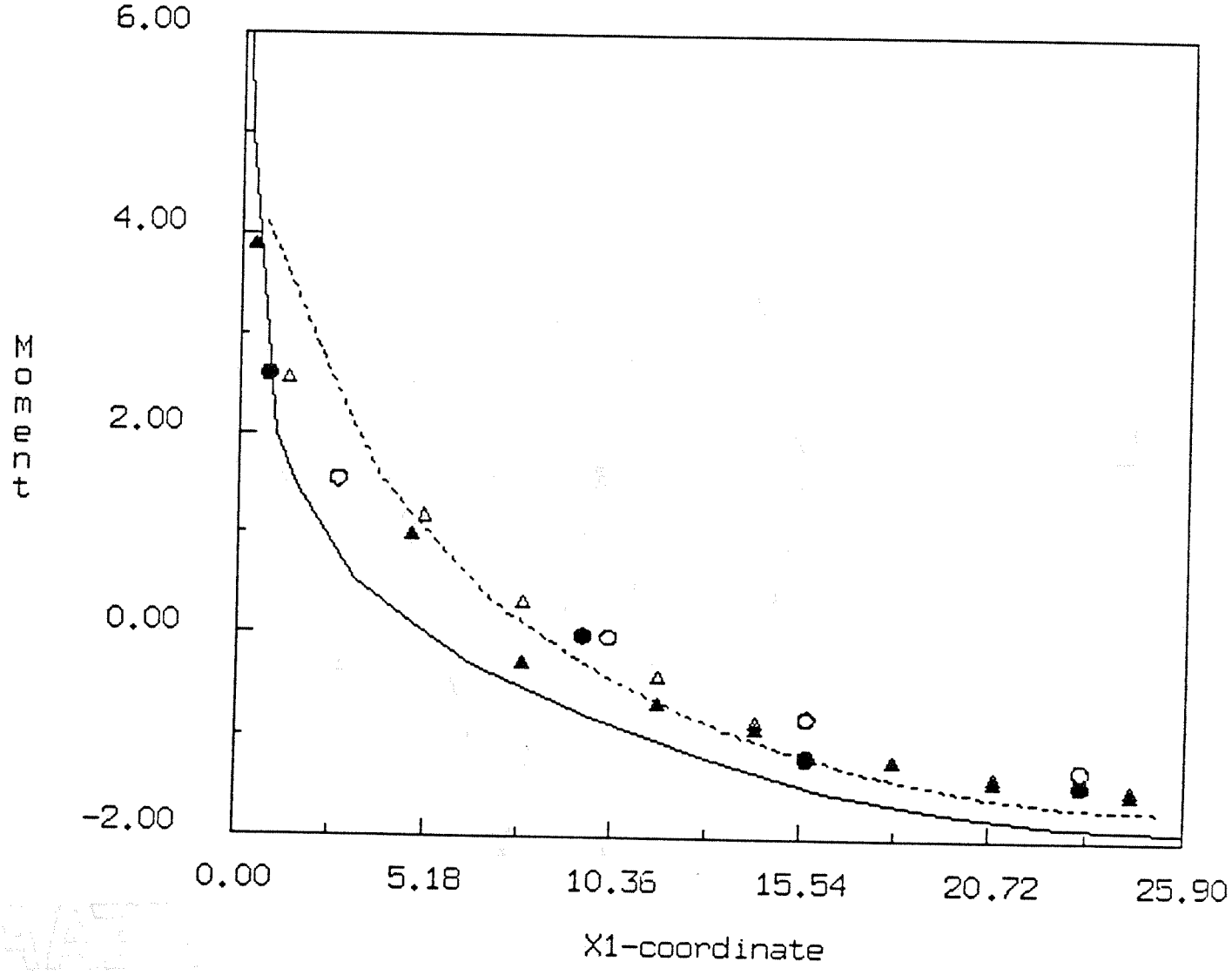

Figure 6.5c. Rhombic plate. Variation of moment M^{12} along the short diagonal. ○: 16 elements. △: 64 elements. Solid line: Morley solution.

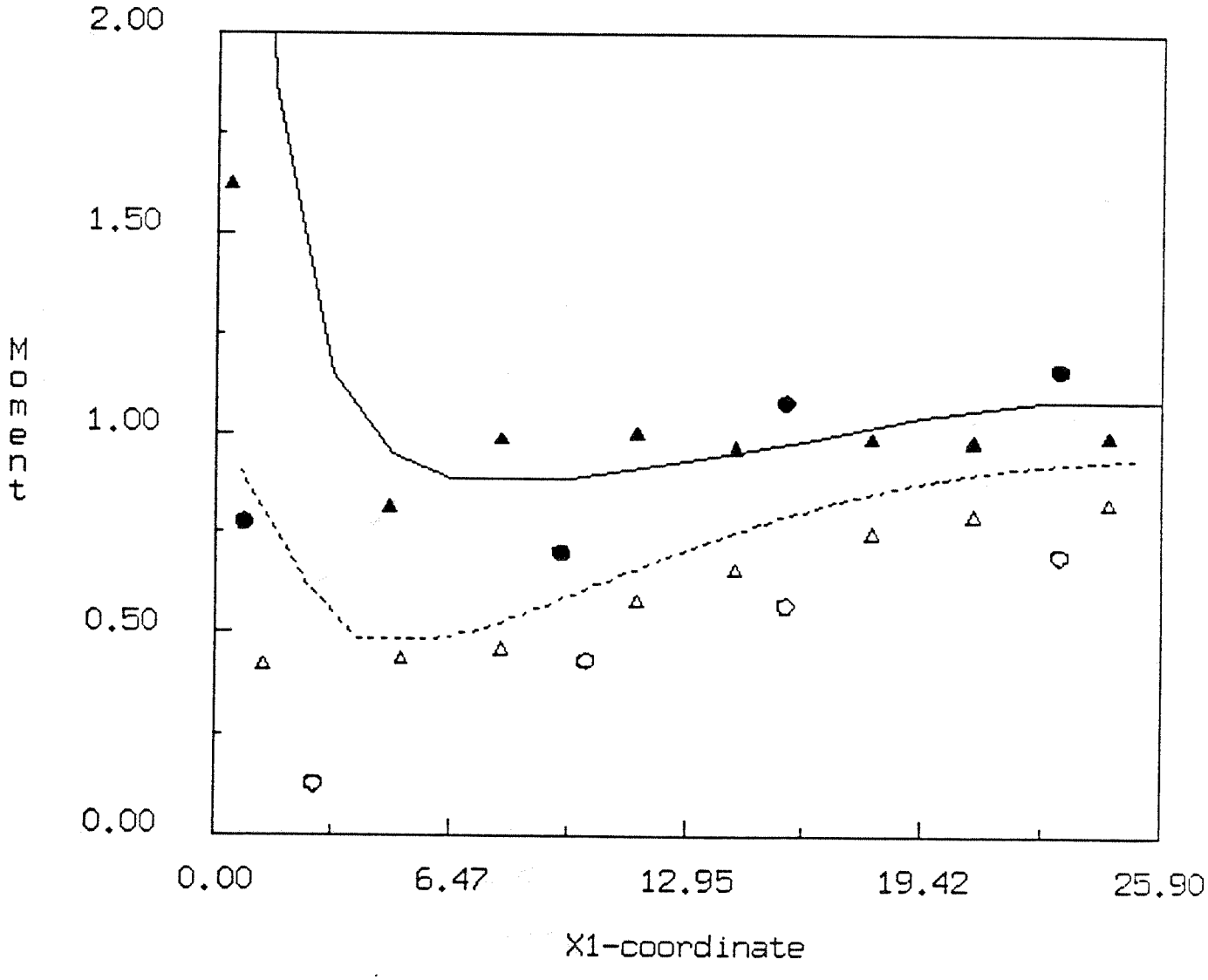

Figure 6.5d. Rhombic plate. Variation of moment M^{21} along the short diagonal. ○: 16 elements, type A. ●: 16 elements, type B. △: 64 elements, type A. ▲: 64 elements, type B. Solid line: Morley solution. Dotted line: 256 elements, type A.

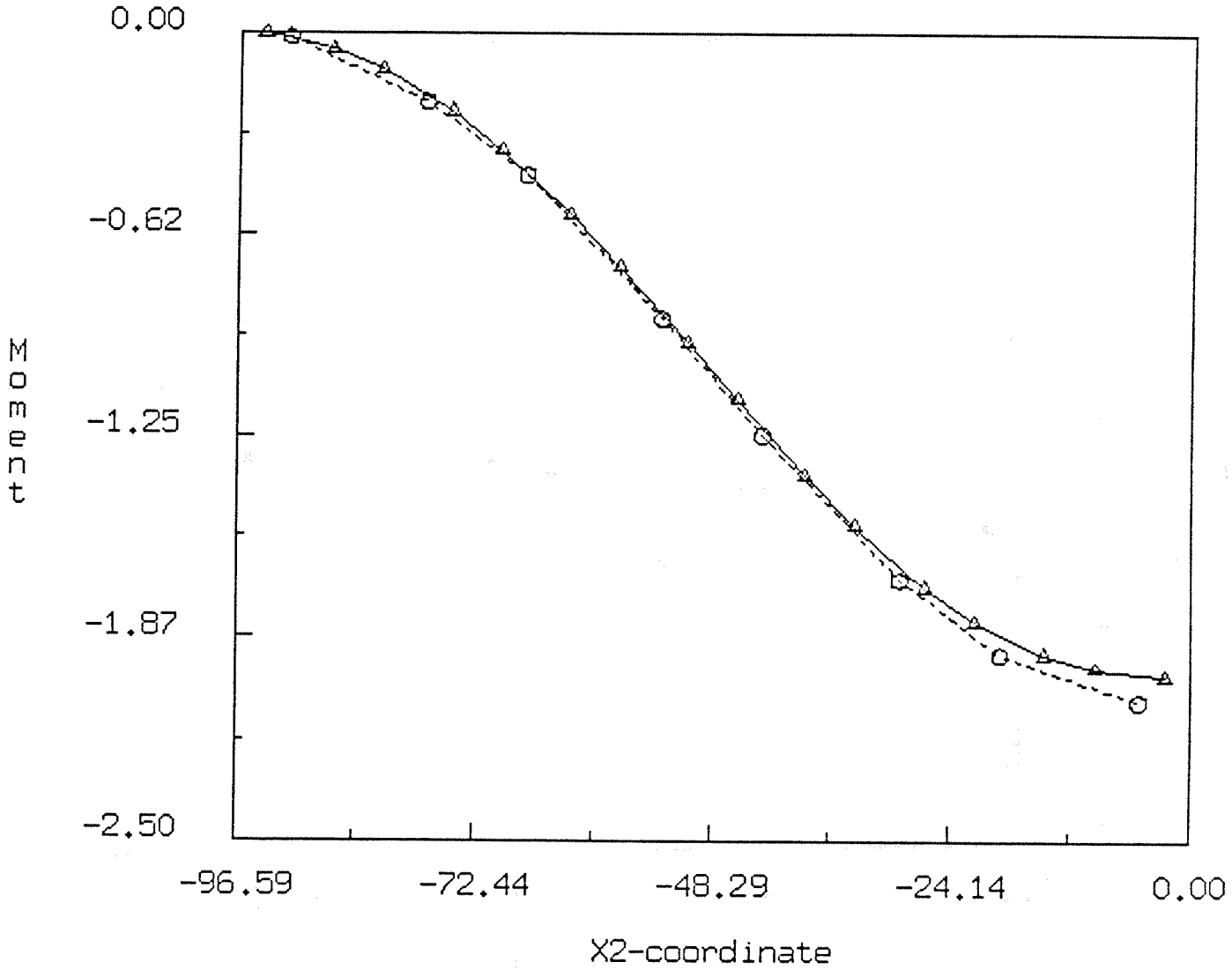

Figure 6.5e. Rhombic plate. Variation of moment M^{12} along the long diagonal. ○: 16 elements. Δ: 64 elements.

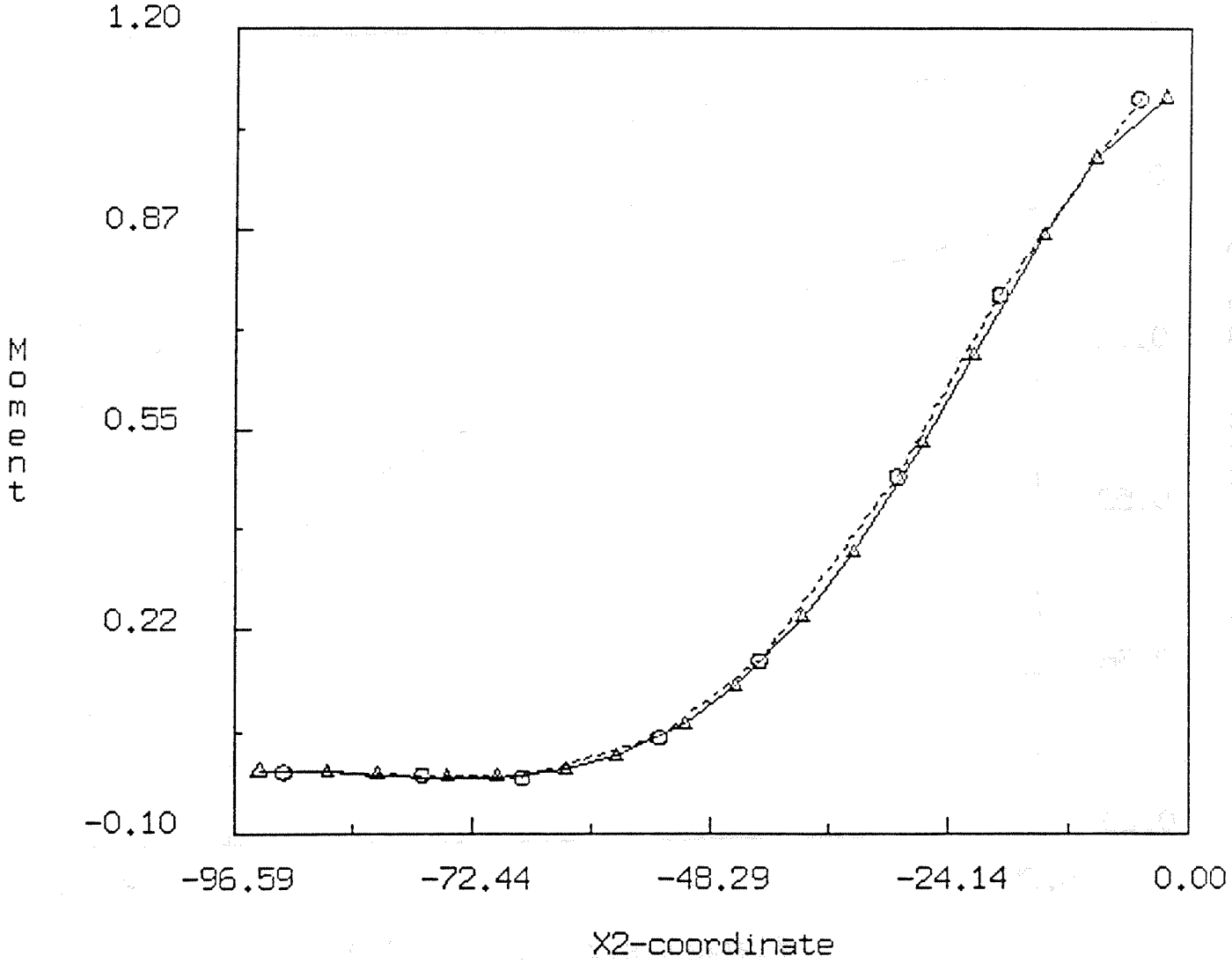

Figure 6.5f. Rhombic plate. Variation of moment M^{21} along the long diagonal. ○: 16 elements. Δ: 64 elements.

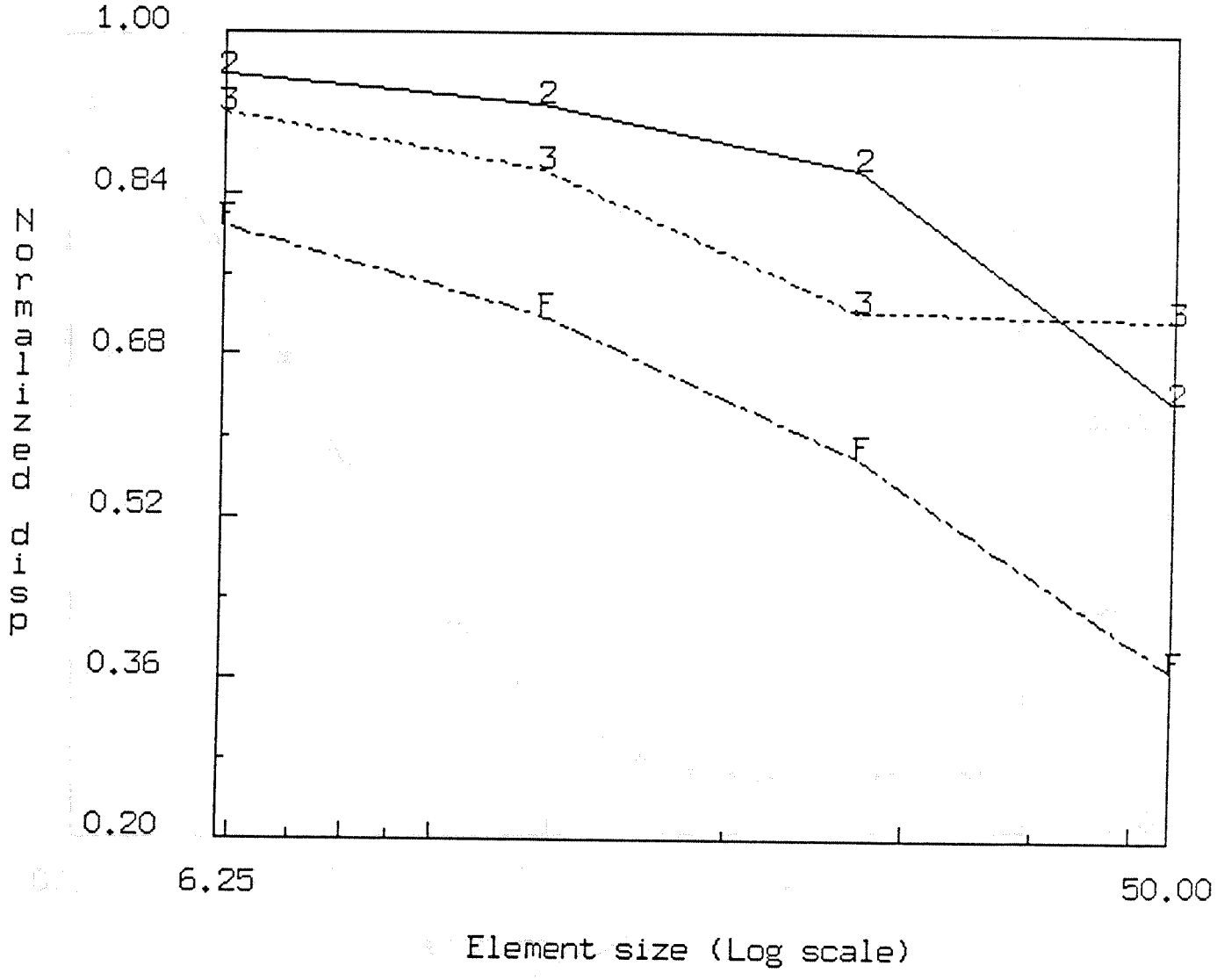

Figure 6.5g. Rhombic plate. Convergence of tranverse displacement at center. (The numbers on the curves are the values of kf with which results are computed. F: Full integration.)

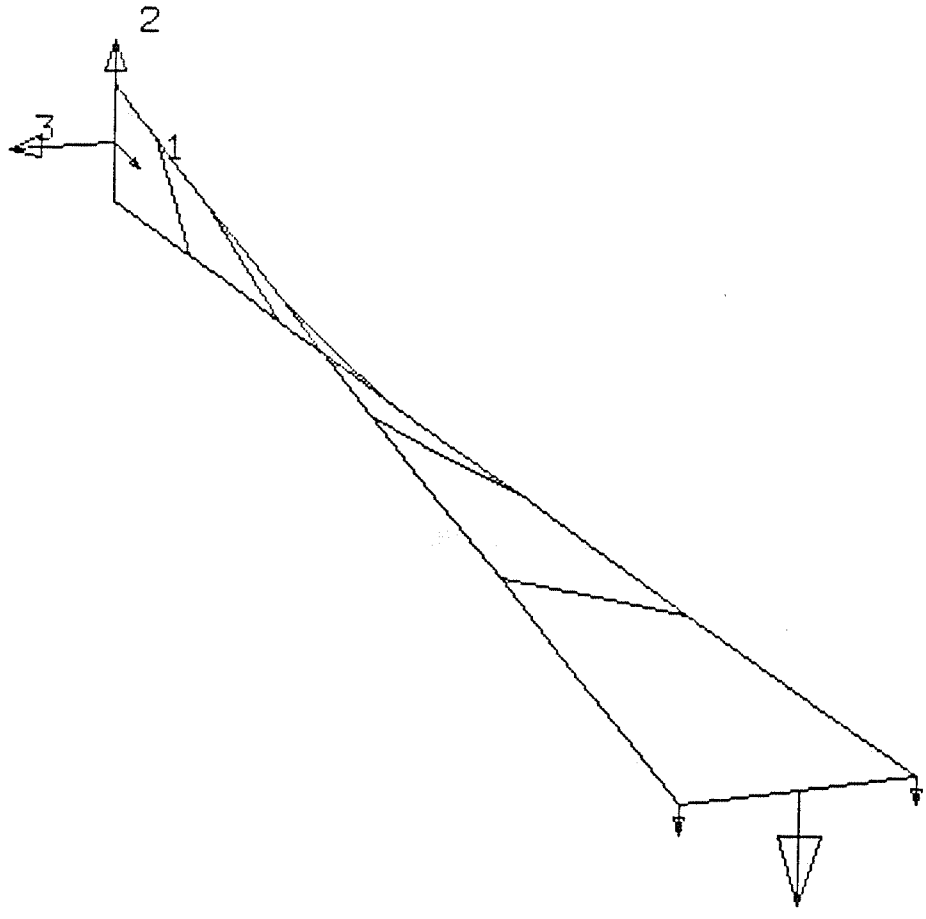

FEAP

Figure 6.6. Twisted beam. Perspective view (shown with out-of-plane shear force).

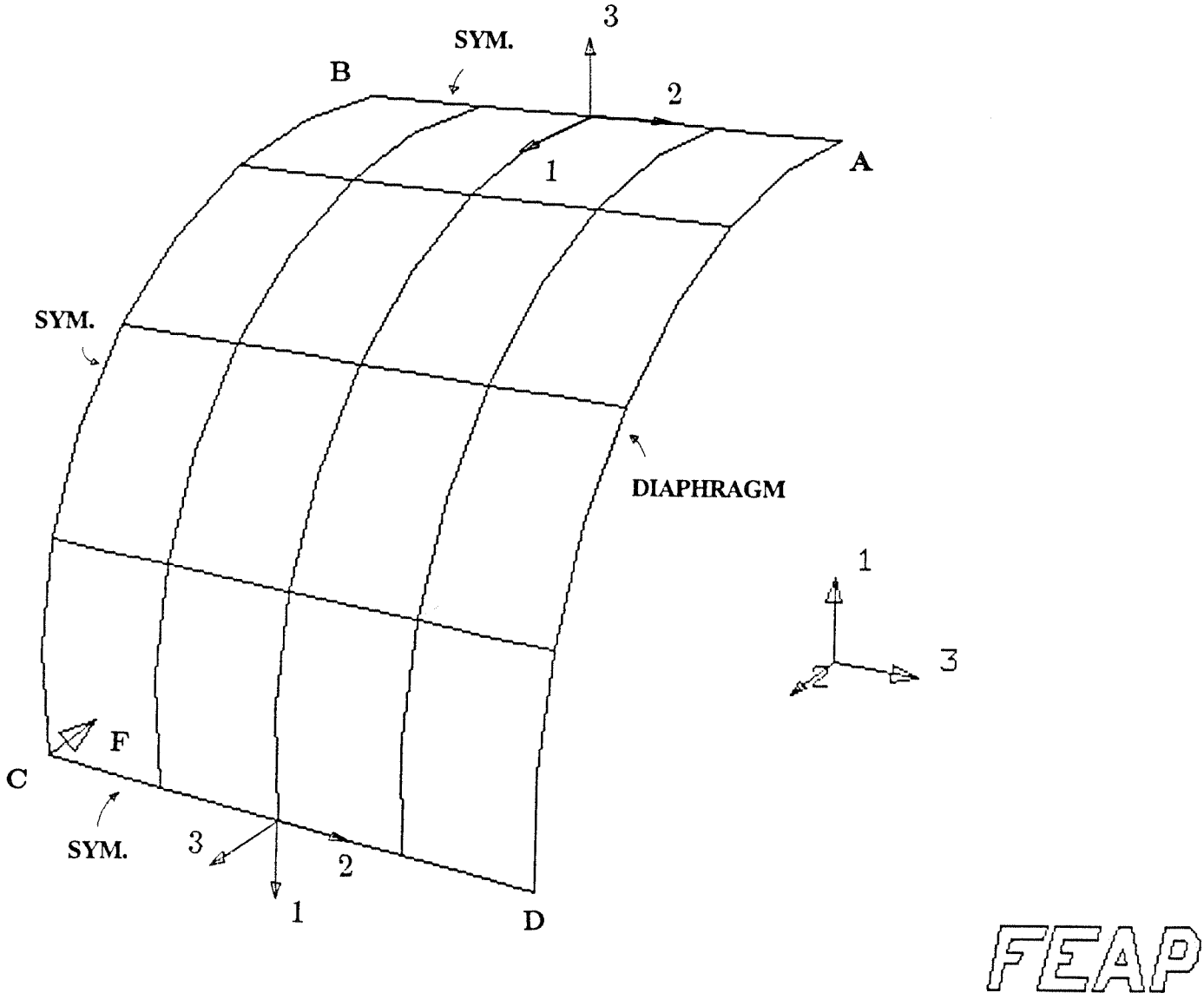

Figure 6.7a. 1/8th of the pinched cylinder. Perspective view.

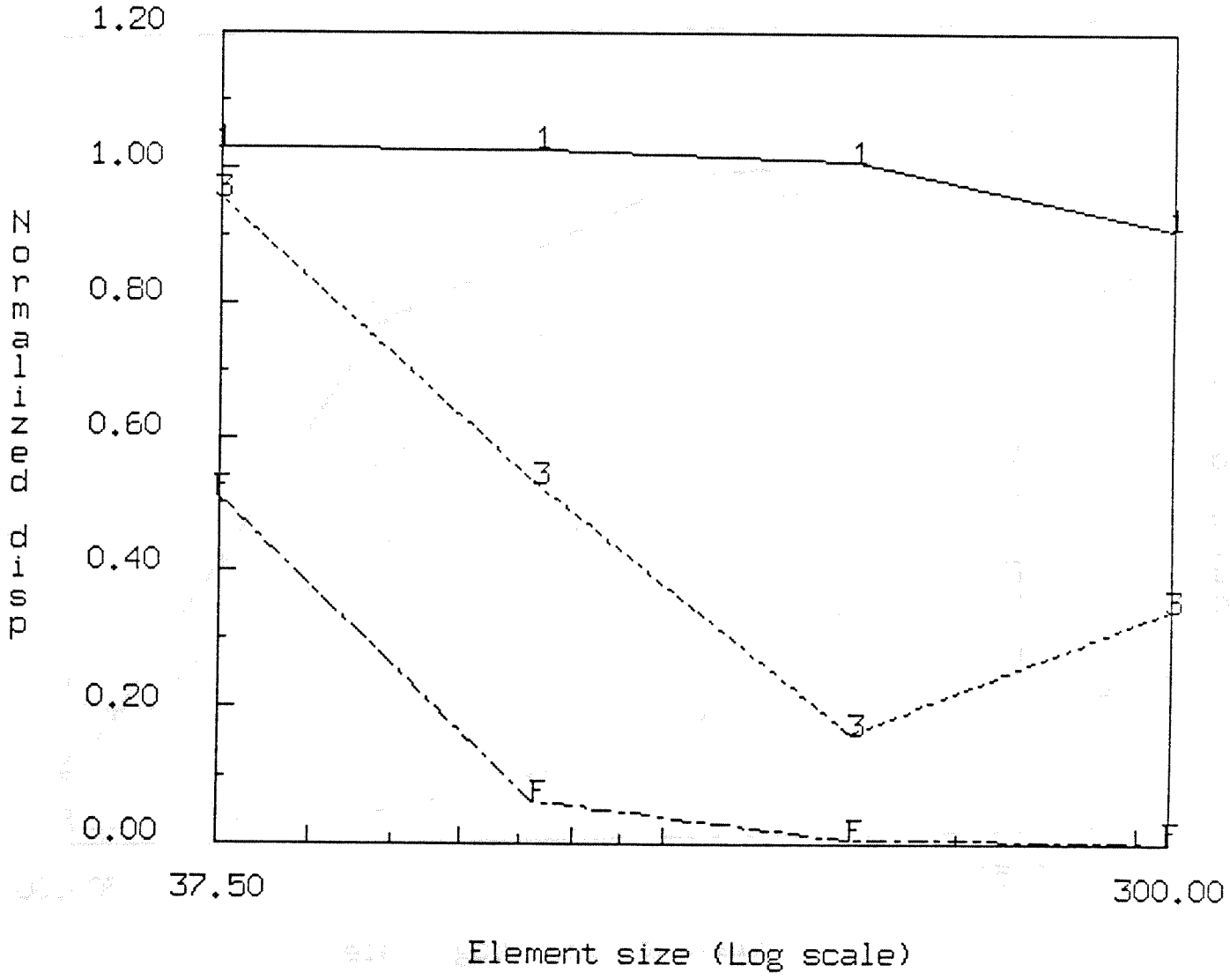

Figure 6.7b. Pinched cylinder with free ends. Convergence of displacement under point force. (The numbers on the curves are the values of kf with which results are computed. F: Full integration.)

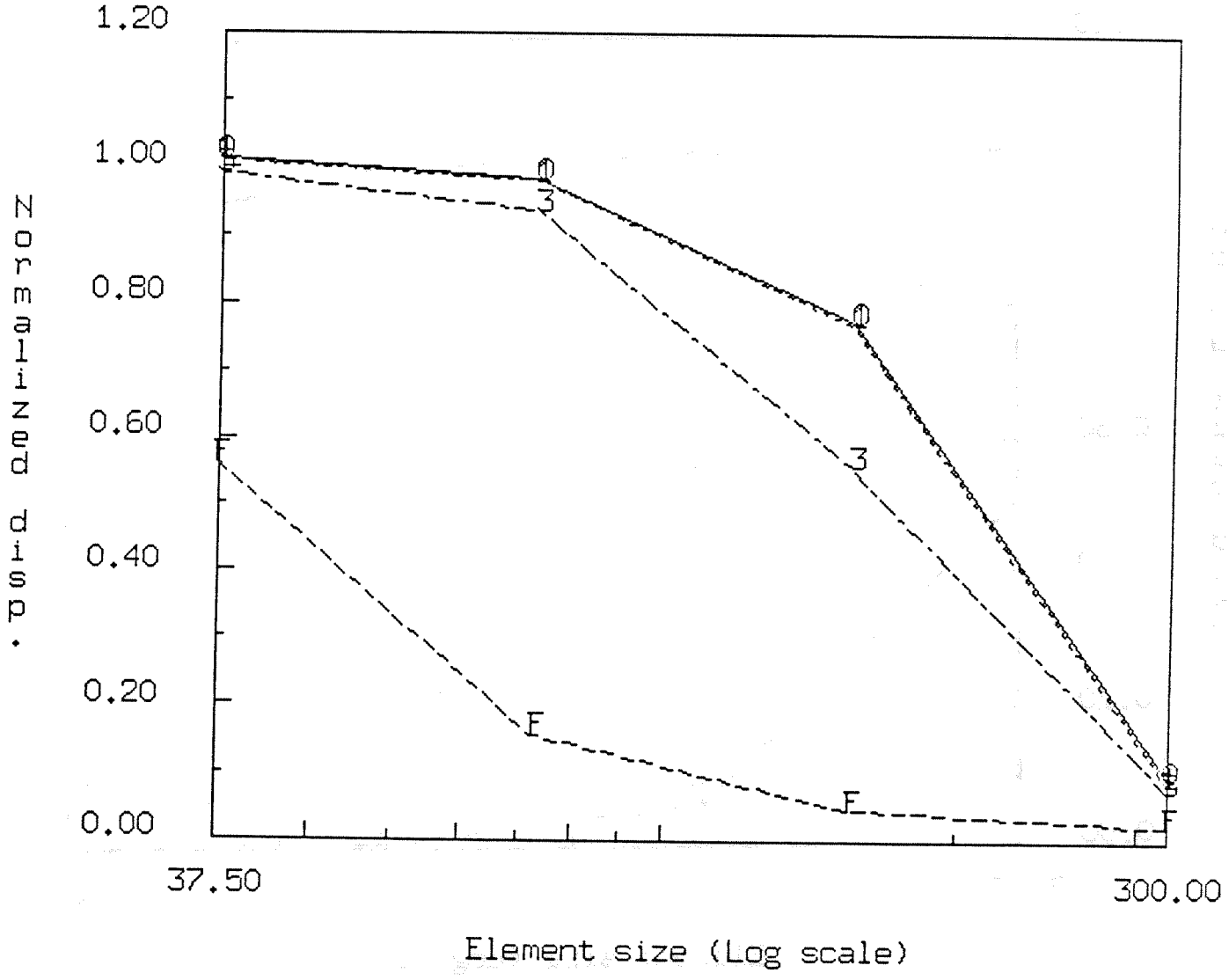

Figure 6.7c. Pinched cylinder with diaphragms. Convergence of displacement under point force. (The numbers on the curves are the values of kf with which results are computed. F: Full integration.)

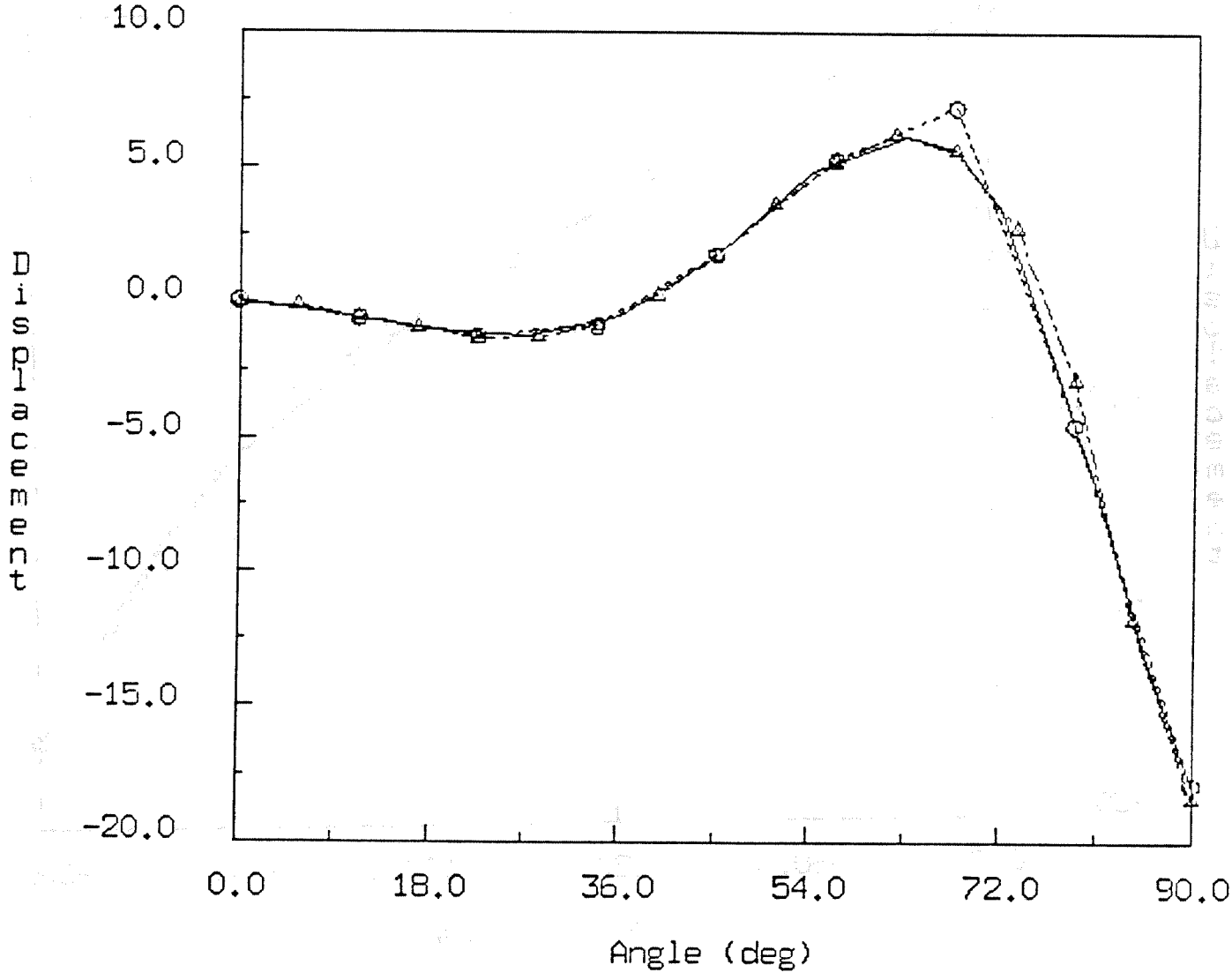

Figure 6.7d. Pinched cylinder with diaphragms. Radial displacement ($\times 10^6$) along BC. O: 16-element mesh. Δ: 64-element mesh. Solid line: Flugge's equations.

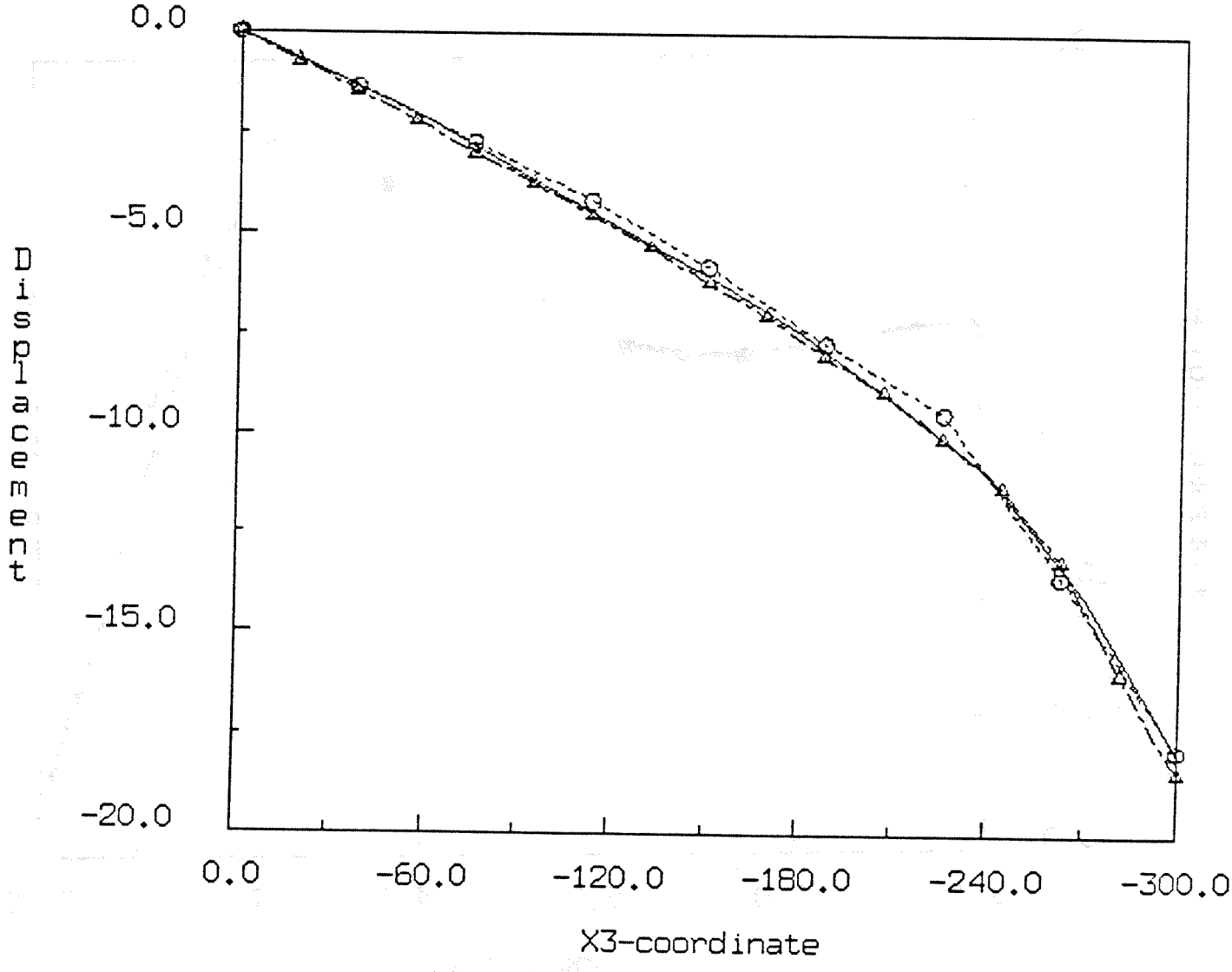

Figure 6.7e. Pinched cylinder with diaphragms. Radial displacement ($\times 10^6$) along DC. $\circ$: 16-element mesh. Δ: 64-element mesh. Solid line: Flugge's equations.

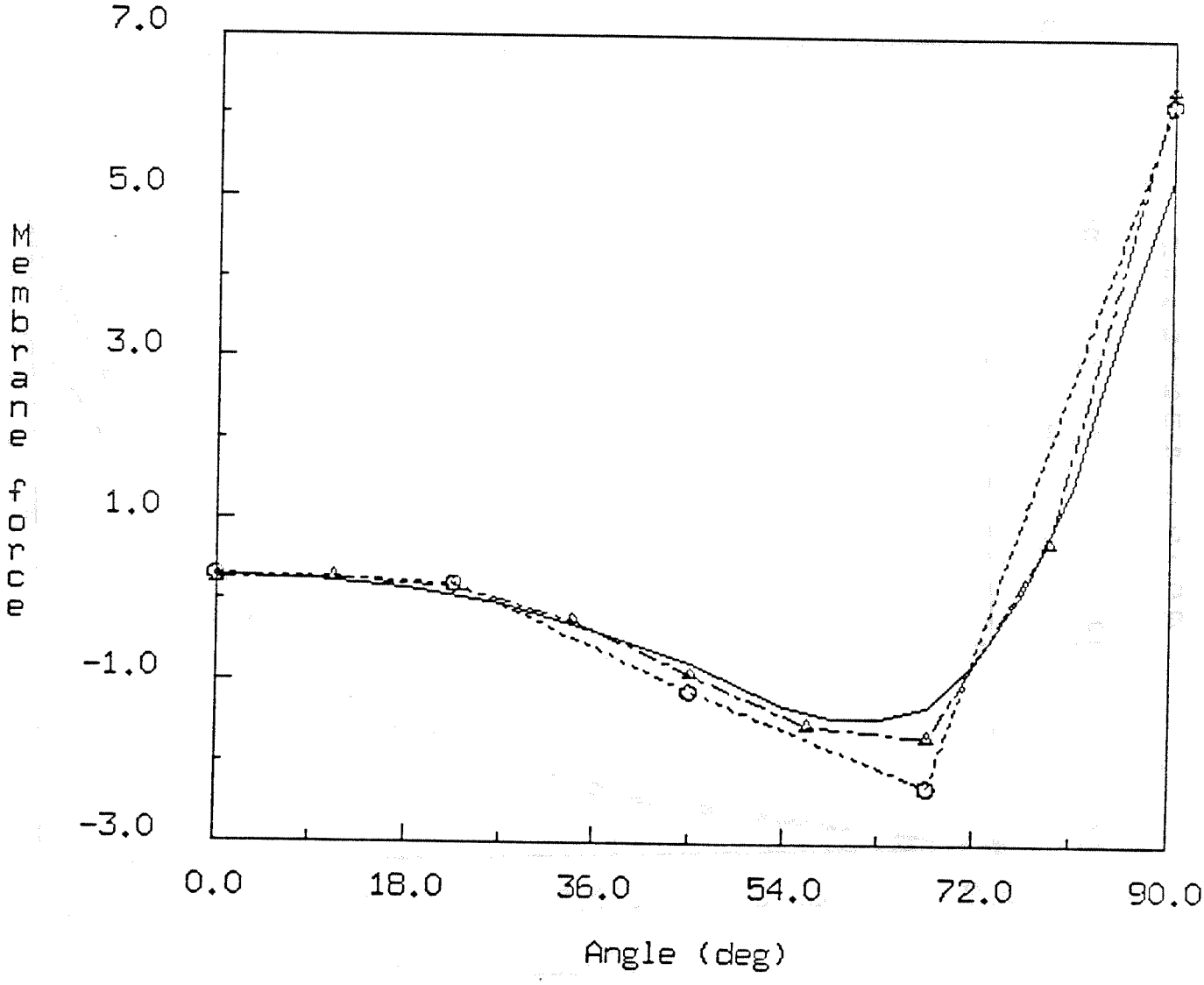

Figure 6.7f. Pinched cylinder with diaphragms. Membrane force N^{11} ($\times 100$) along line BC. ○: 16-element mesh. Δ: 64-element mesh. Solid line: Flugge's equations.

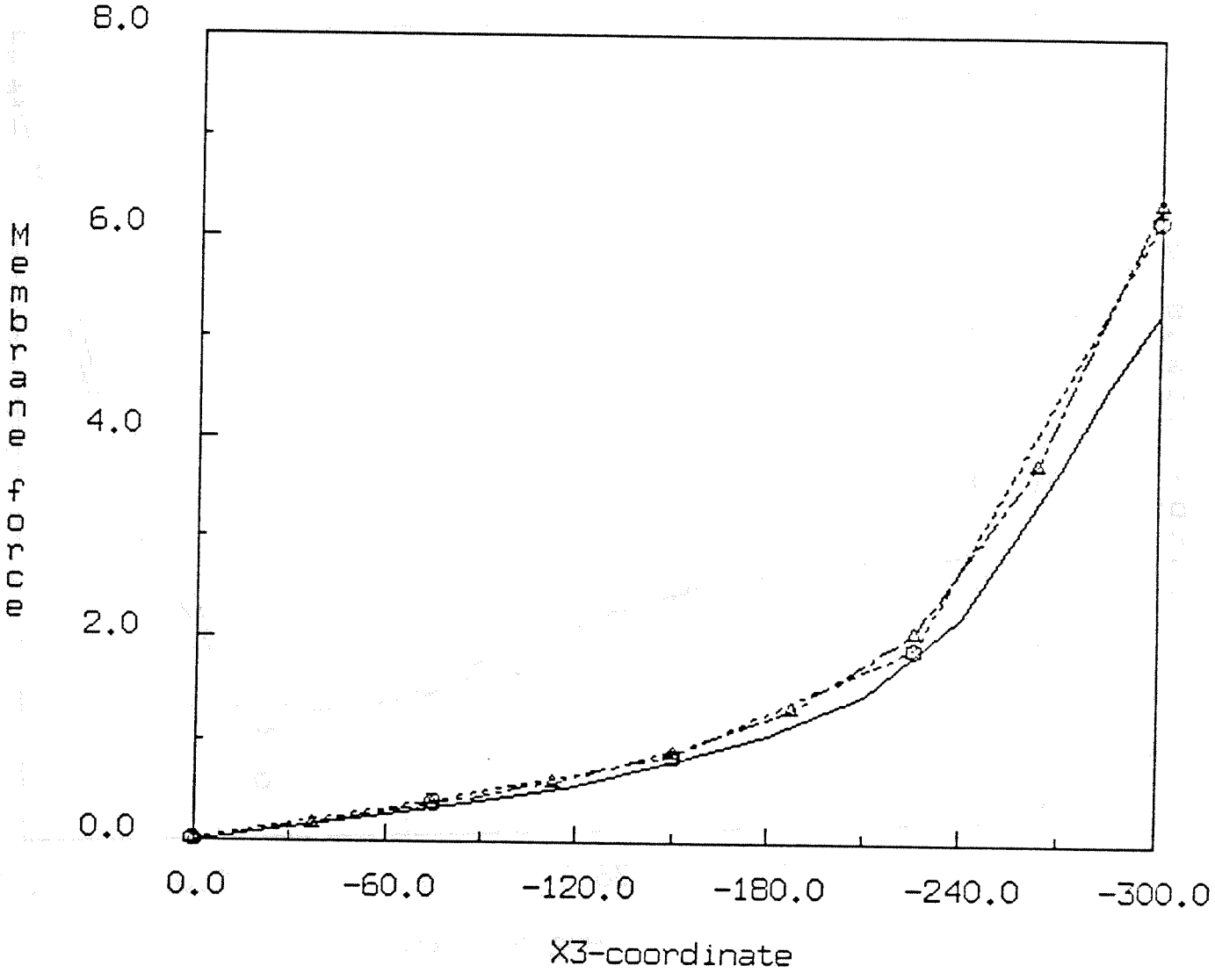

Figure 6.7g. Pinched cylinder with diaphragms. Membrane force N^{11} ($\times 100$) along line DC. O: 16-element mesh. Δ: 64-element mesh. Solid line: Flugge's equations.

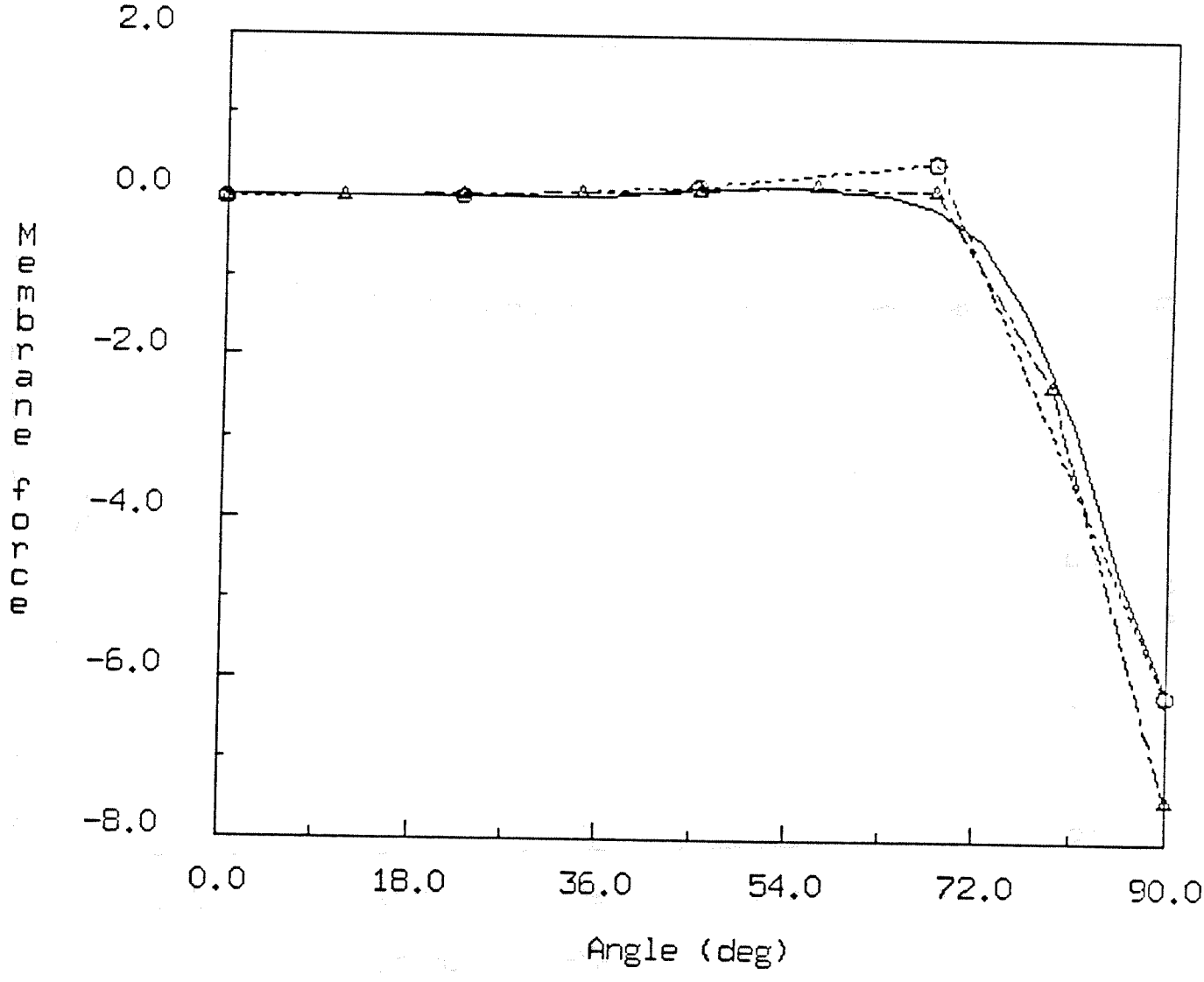

Figure 6.7h. Pinched cylinder with diaphragms. Membrane force N^{22} ($\times 100$) along line BC. ○: 16-element mesh. Δ: 64-element mesh. Solid line: Flugge's equations.

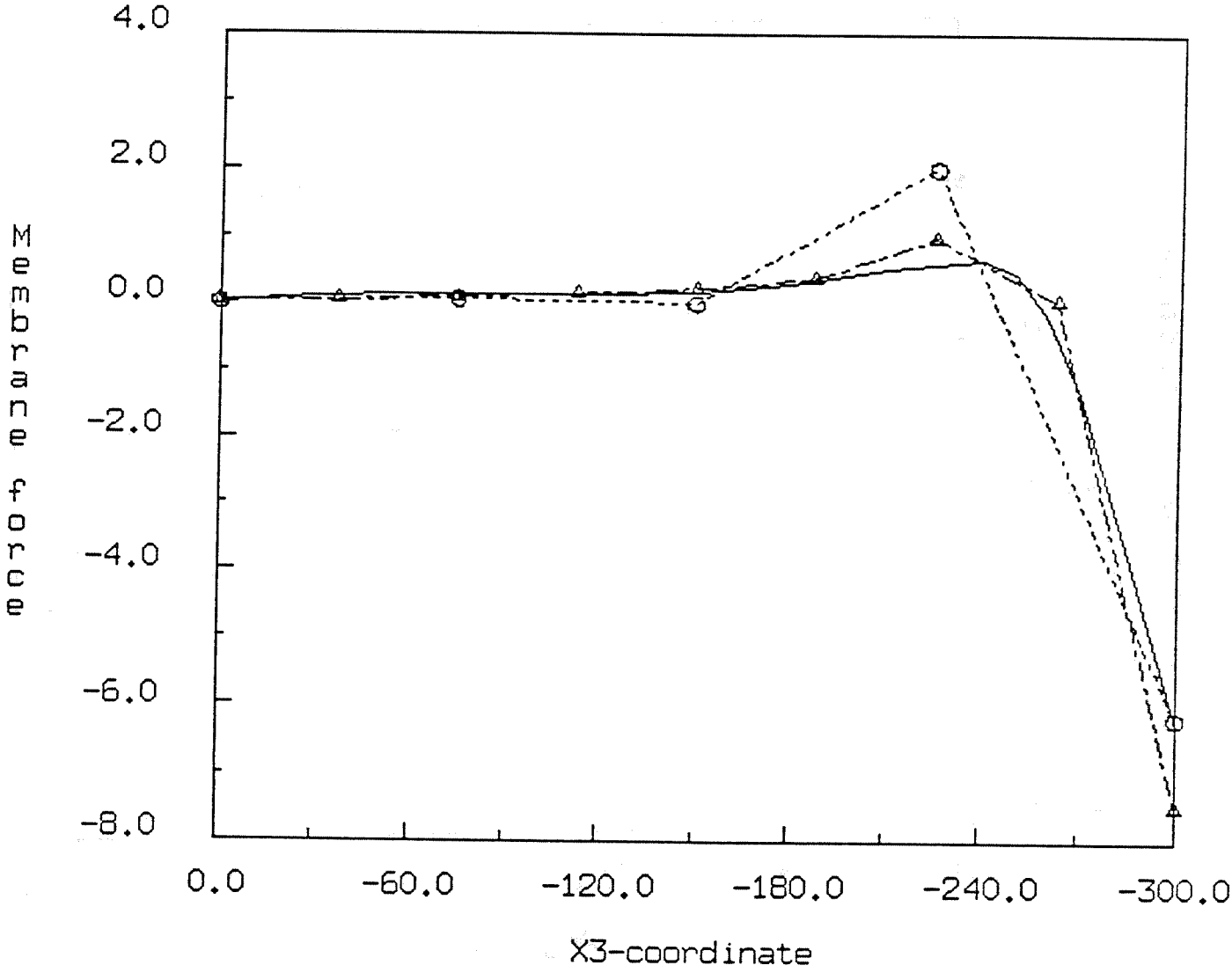

Figure 6.7i. Pinched cylinder with diaphragms. Membrane force N^{22} ($\times 100$) along line DC. $\circ$: 16-element mesh. Δ: 64-element mesh. Solid line: Flugge's equations.

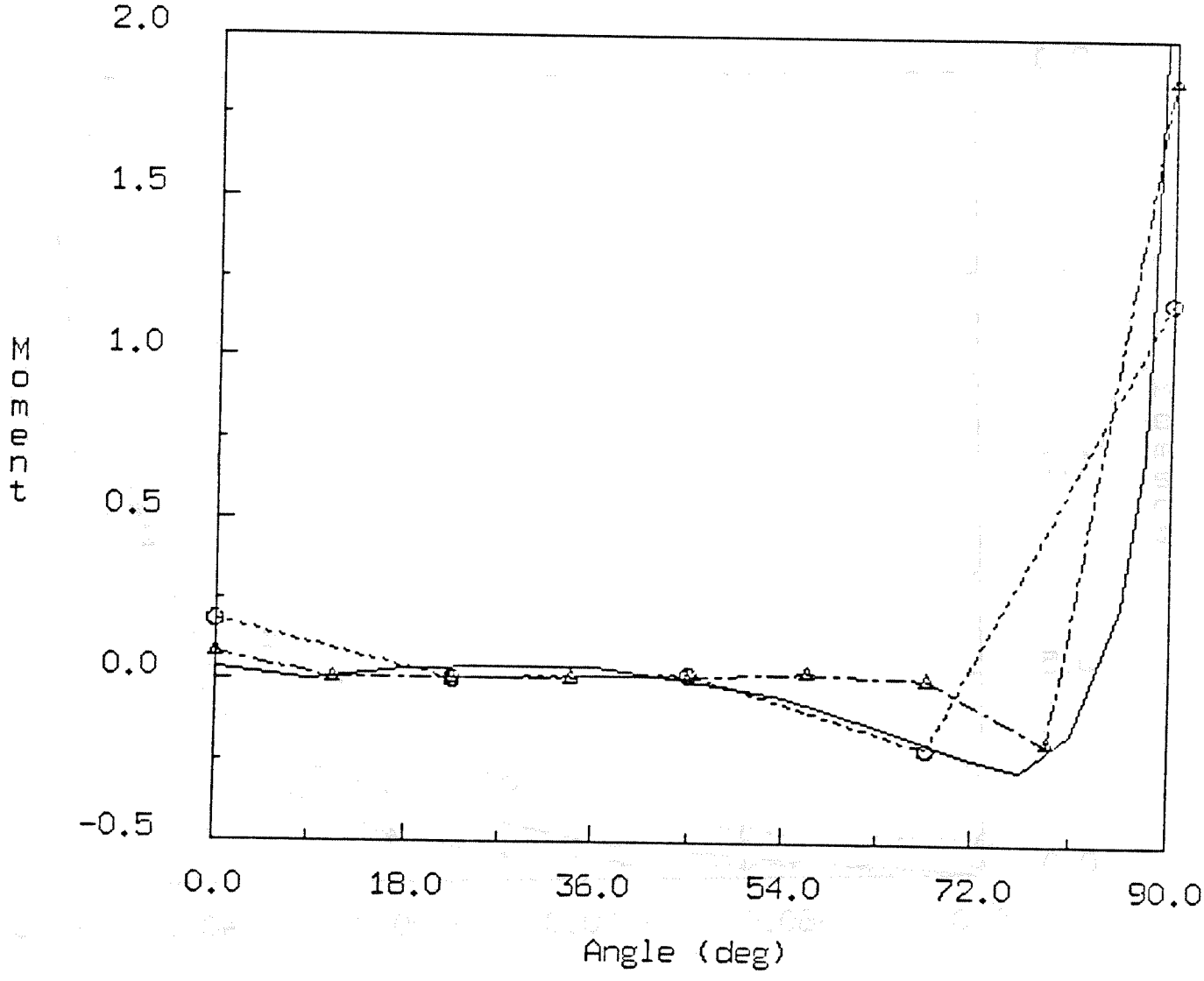

Figure 6.7j. Pinched cylinder with diaphragms. Moment M^{21} ($\times 10$) along line BC. ○: 16-element mesh. Δ: 64-element mesh. Solid line: Flugge's equations.

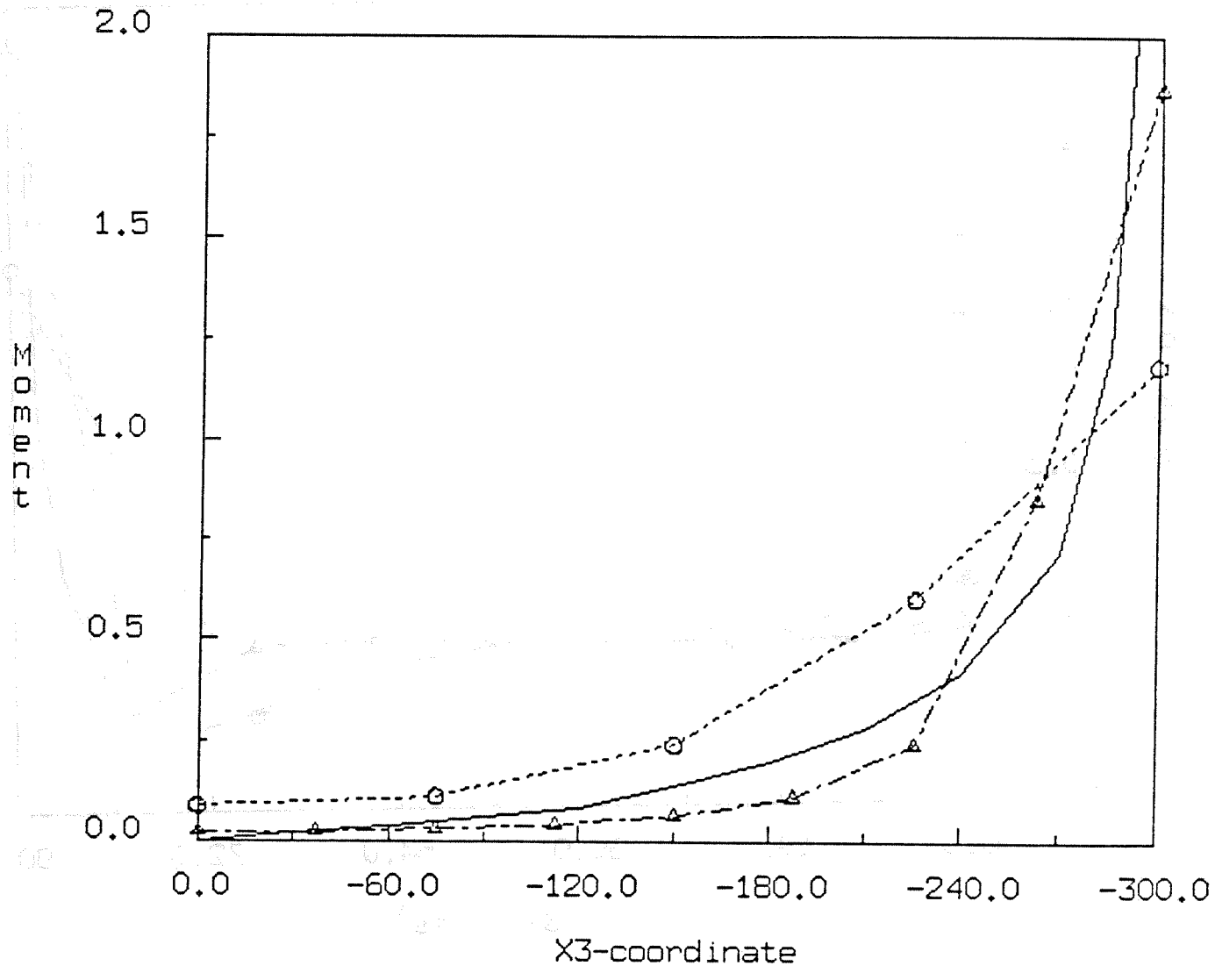

Figure 6.7k. Pinched cylinder with diaphragms. Moment M^{21} ($\times 10$) along line DC. ○: 16-element mesh. △: 64-element mesh. Solid line: Flugge's equations.

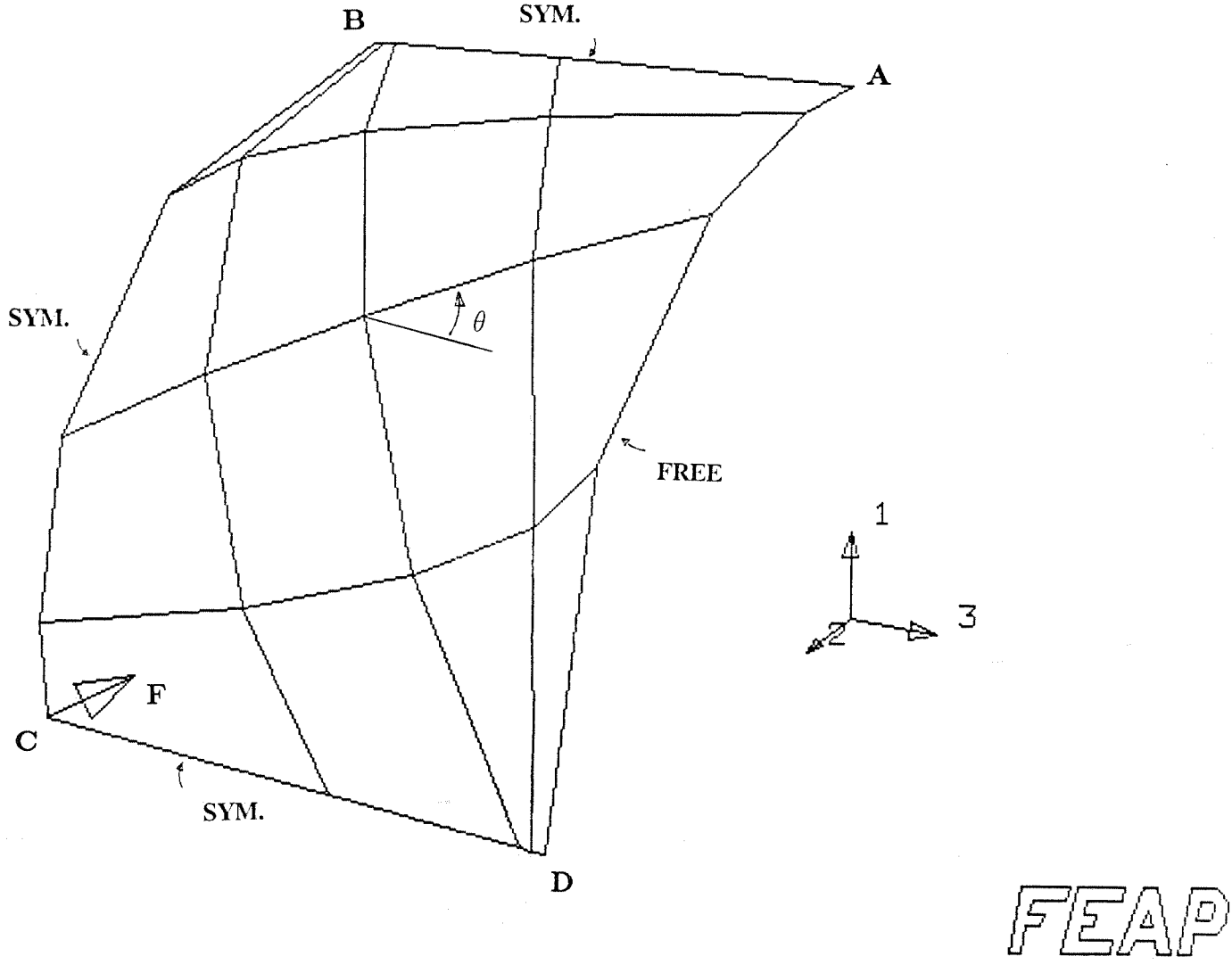

Figure 6.7l. Pinched cylinder with free ends. 4-element mesh shown with 30° angle of distortion. Lines connecting mid-side nodes to interior nodes are plotted to show distortion of mesh.

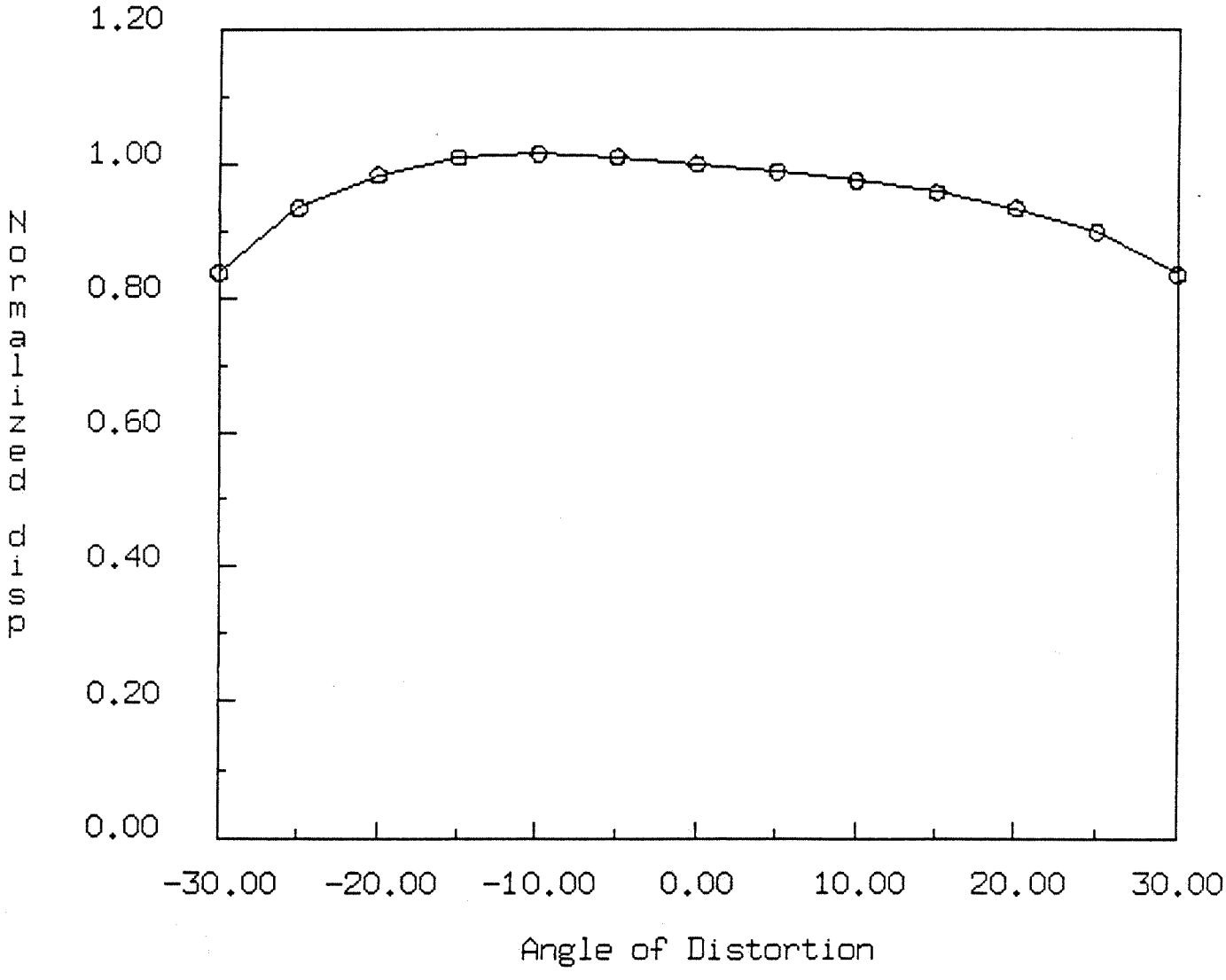

Figure 6.7m. Pinched cylinder with free ends. 4-element distorted mesh. Displacement normalized with the one from undistorted mesh.

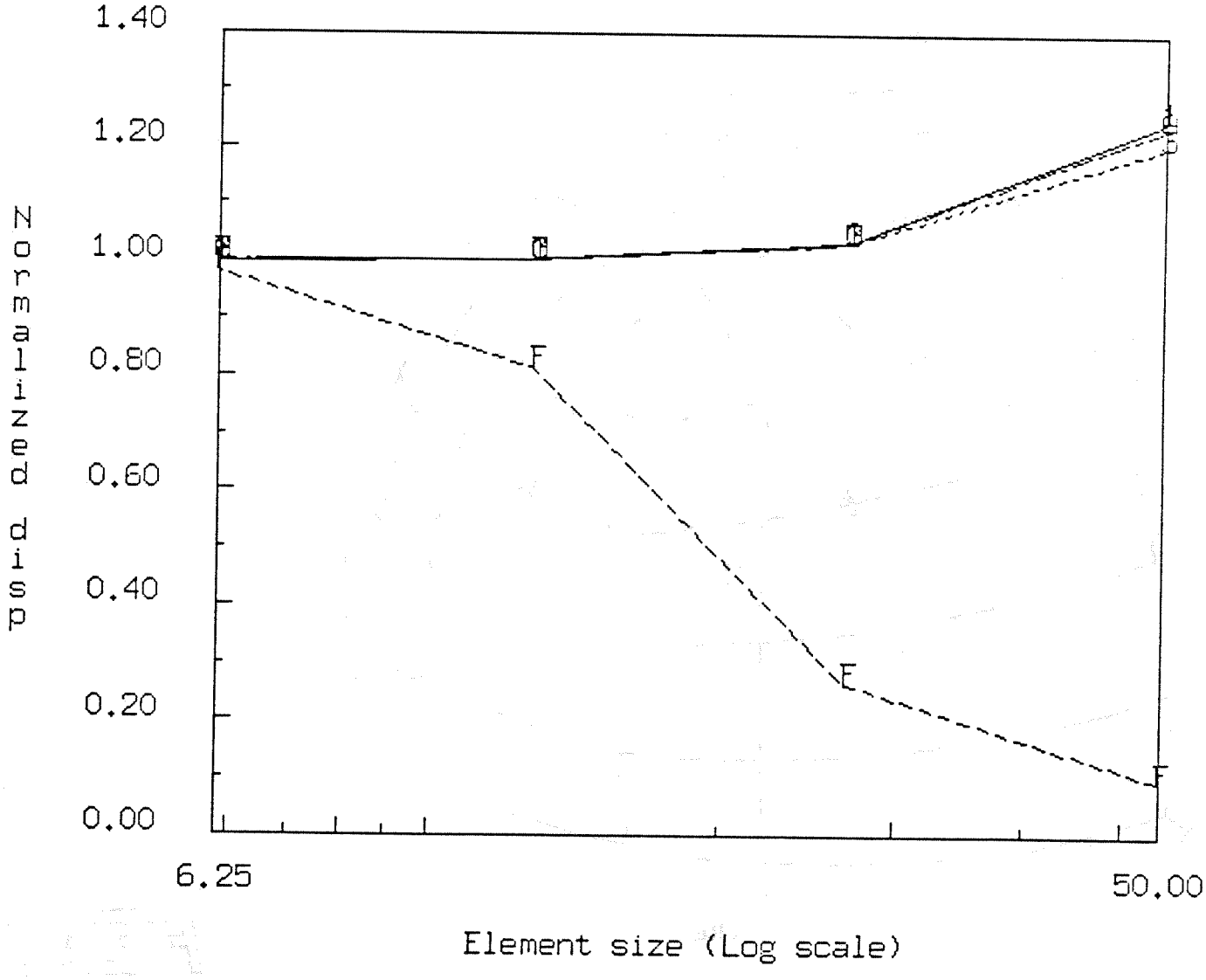

Figure 6.8. Scordelis-Lo roof. Convergence of vertical displacement at mid-span of free edge. (The numbers on the curves are the values of kf with which results are computed. F: Full integration.)

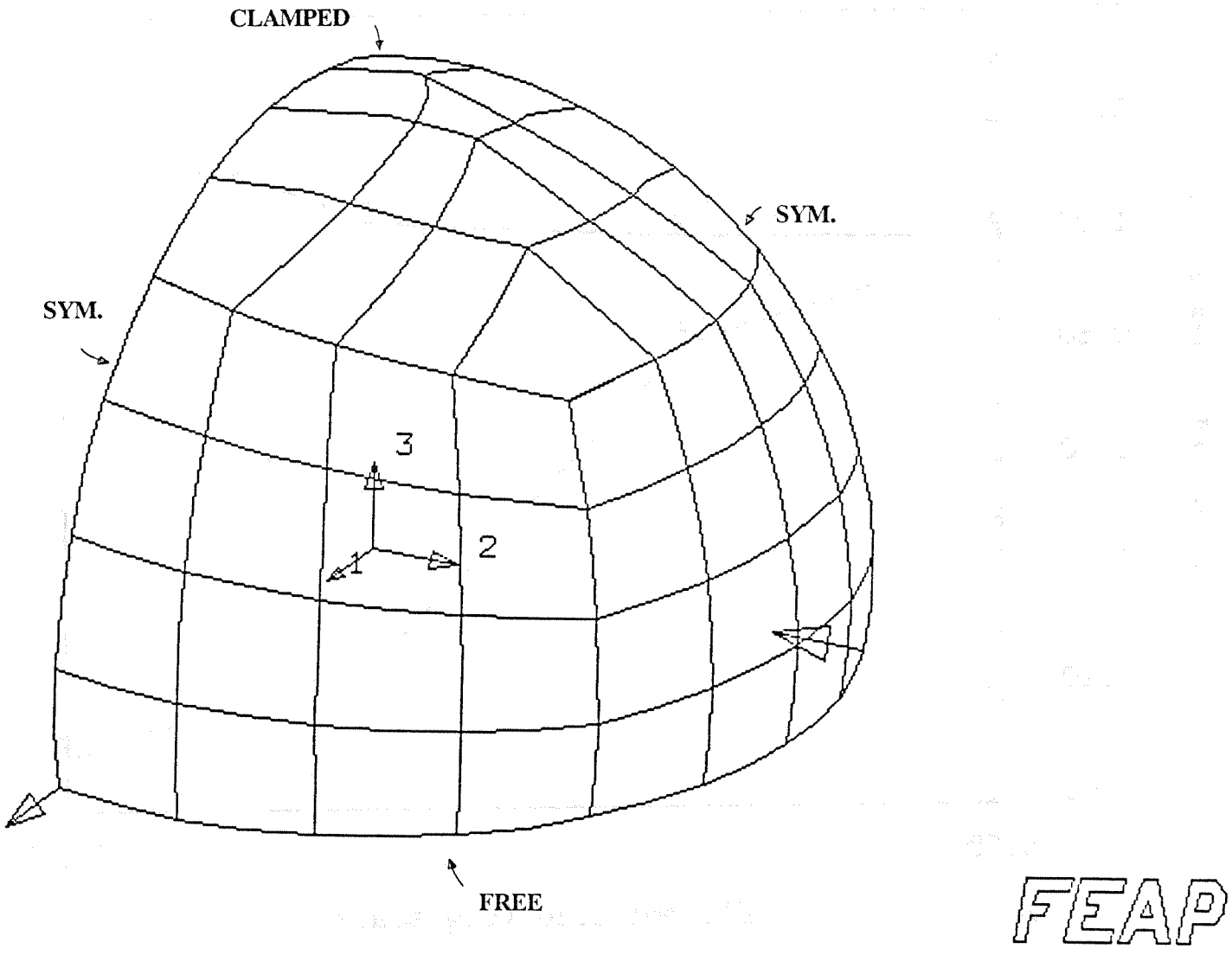

Figure 6.9a. Hemispherical shell. Perspective view (48-element mesh).

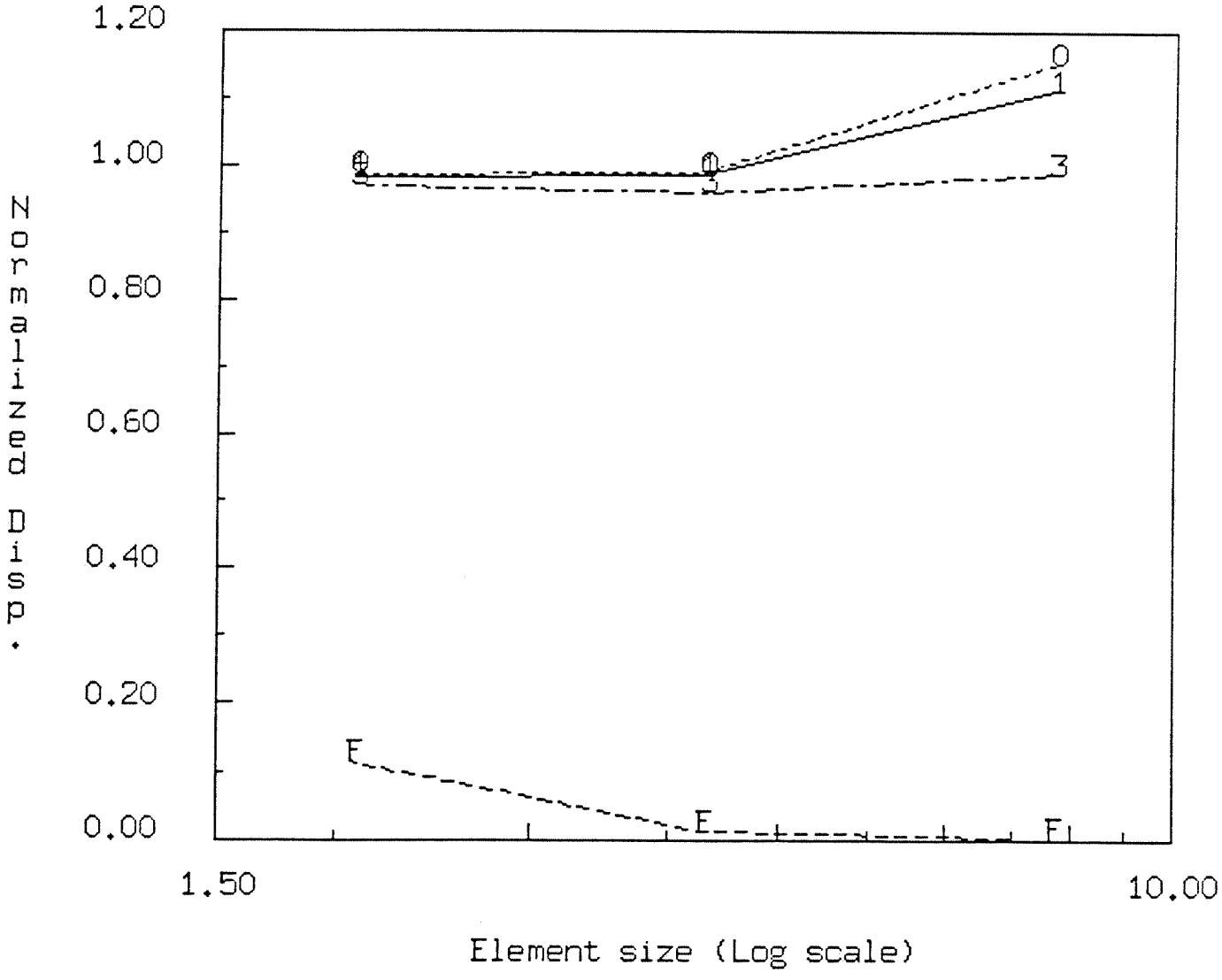

Figure 6.9b. Hemispherical shell. Convergence of displacement under point force. (The numbers on the curves are the values of kf with which results are computed. F: Full integration.)